

**A HIGH VOLTAGE PIEZOELECTRIC TRANSFORMER FOR
ACTIVE INTERROGATION**

A Dissertation
Presented to
The Faculty of the Graduate School
University of Missouri-Columbia

In Partial Fulfillment
Of the Requirements for the Degree
Doctor of Philosophy

By
ANDREW L. BENWELL

Dr. Scott D. Kovaleski, Dissertation Advisor

DECEMBER 2009

The undersigned, appointed by the Dean of the Graduate School,
have examined the dissertation entitled

**A HIGH VOLTAGE PIEZOELECTRIC TRANSFORMER FOR
ACTIVE INTERROGATION**

presented by Andrew Benwell,

a candidate for the degree of Doctor of Philosophy of Electrical
Engineering, and hereby certify that in their opinion it is worthy of
acceptance.

Dr. Scott D. Kovaleski, Dissertation Advisor
Electrical and Computer Engineering

Dr. John M. Gahl
Chemical Engineering

Dr. Jae Wan Kwon
Electrical and Computer Engineering

Dr. Naz Islam
Electrical and Computer Engineering

ACKNOWLEDGEMENTS

I gratefully thank Dr. Kovaleski for your guidance and leadership throughout graduate school. Thanks for the times of friendship, the times of incentive to get work done, and the freedom to learn at my own pace when needed.

I thank Dr. Gahl for guiding me down the path of graduate research while I was an undergraduate student and still unsure of which direction my education would lead me. Thanks for your personal interest in my graduate work. Thanks to Dr. Kwon for your technical interest in my project and your assistance in improving my research. Thanks to Dr. Islam for your knowledgeable suggestions and comments.

Special thanks to Tongtawee Wacharashindu and Riberet Almeida for your advice and invaluable help in this project. Thanks for interesting late night discussions in the laboratory and useful help with fabrication of important experimental components.

Thank you Brian, Jim, and Mark for your friendship and help in all aspects of hard work, procrastination, camaraderie, and life in general as graduate researchers.

Many thanks to Emily and Erik for your collaboration, and conversation over the last few months. Additionally thanks to Bill and Dustin for your willingness to help.

I would like to specially thank the Baxter family, and Emily again, for your interest in my progress and for your conversations on Saturday afternoons when you stopped by at the lab with food.

Thank you, Mom and Dad, for your encouragement and guidance through all of the years of my education. Thank you, Katie, for your patience, help, and company over all the years, and thank you for a place to live while I finished my work in Columbia.

Thank you, Risa, for your patience, support, and love.

Contents

Abstract.....	x
1. Introduction.....	1
Compact Active Interrogation	1
Neutron Sources	3
Portable Active Interrogation	3
D-D fusion.....	4
Piezoelectric Theory.....	5
High Voltage Piezoelectric Transformers	14
Project Overview.....	18
2. Finite Element Simulations.....	21
Behavior of PT	21
High Voltage Gain.....	23
High Electric Field.....	32
Peak Output Voltage.....	36
Even Stress Profile	41
PT Length.....	42
Bipolar Signal, PT squeezed from middle	44
Trapezoid shaped surface	46
Wedge shaped edge	47
Mass loading.....	49
Longer length PT	50
Finite Element Simulation Summary	52
3. Experiment Setup.....	54
Atmospheric Test Stand	54
PT Holder	61
Vacuum Test Stand	63
Flashover Test Stand	69
4. Data and Analysis.....	70
Input Impedance	71
Equivalent Circuit	72
Mechanical Loss	75

Flashover Prevention	77
High Voltage Measurements	85
Variable Capacitance Diagnostic	87
X-ray High Voltage Measurements	89
Overstressed Piezoelectric Transformers	97
Bipolar Output Verification	98
5. Conclusions	101
Summary	101
Future Work	104
APPENDIX	105
Comsol Simulation Guideline	105
Matlab Data Calculations	106
Impedance Calculating Script.....	112
Impedance Matching Network Design Matlab Script	114
Photo Resist Patterns.....	115
Bibliography	116
VITA.....	120

LIST OF FIGURES

Figure 1: Example of a large scale neutron source concept for active interrogation of shipping containers [2].	3
Figure 2: Piezelectric beam or plate squeezed through the thickness (a) prior to being deformed and (b) after deformation has occured along the length.	7
Figure 3: Bar shaped crystal and orthogonal directions	10
Figure 4: Displacement of a piezoelectric bar under length extensional resonance at the half a full wavelength resonance modes. A vibration null occurs near the center of the PT at 0.0375 meters.	12
Figure 5: The directional derivative of the piezoelectric material under half wavelength resonance.	13
Figure 6: 135° rotation [29]	15
Figure 7: Rotational affect on coupling coefficients [29]	16
Figure 8: The resonant frequencies are predicted using the physical properties of LiNbO3 and the geometry of the transformer. Intersection points represent the half and full wavelength resonant frequencies and asymptotes represent anti-resonance.	18
Figure 9: The PT with electrodes drawn in the finite element software graphical interface.	22
Figure 10: Simulated electrical potential on PT surface	24
Figure 11: Measurements were recorded at the frequency according to the FWHM of the output voltage	26
Figure 12: Increasing the length of the device reduced the resonant frequency	27
Figure 13: Increasing the input voltage produced a greater output voltage. This demonstrated a true transformer gain effect.	28
Figure 14: The length of the input electrode should be matched to the length of the device. An electrode greater than 46.5% of the length of the device decreased the peak output voltage.	29
Figure 15: The length of the output electrode affected the peak voltage available at the electrode. A longer electrode decreased the output voltage, but can increase the output current according to Equation 19.	31
Figure 16: Introducing a loss factor to the LiNbO3 greatly affected the performance of the device.	32
Figure 17: Electric field resulting in flashover	33
Figure 18: Location of high electric field due to triple point enhancement...	35
Figure 19: Electric field minima	36
Figure 20: Finite element simulation of the PT under conditions which experimentally led to PT fracture.	38
Figure 21: Peak output voltage that is produced with an applied voltage, V , over a range of frequencies extending from resonance, f_0 .	39

Figure 22: Peak von Mises stress that is produced with an applied voltage, V , over a range of frequencies extending from resonance, f_0	40
Figure 23: The threshold applied voltage for producing greater than 100 kV and less than 30 MPa over a range of frequencies extending from resonance, f_0	41
Figure 24: The predicted output voltage available from a PT of a specific length. This is determined as the simulated output voltage with a stress of less than 30 MPa.	43
Figure 25: The peak output voltage for a length extensional PT is scalable according to the device length. These displayed voltages adhere to the 30 MPa requirement.	44
Figure 26: Output electric potential for a bar shaped PT while squeezing through the middle of the device.	45
Figure 27: Von Mises stress profile in the PT at a peak stress of 30 MPa. This arrangement provided 22 kV	45
Figure 28: Output electric potential for a trapezoid shaped PT at 30 MPa. ..	46
Figure 29: The stress of a trapezoid shaped cross section is more evenly distributed along the length of the PT leading to higher voltages.	47
Figure 30: Electric potential on the surface of a wedge shaped PT at 31 MPa.	48
Figure 31: Von Mises stress profile for a wedge shaped PT at 31 MPa.	48
Figure 32: Electric potential for a mass loaded PT with tapered edges at 31 MPa.....	49
Figure 33: The von Mises stress profile of a mass loaded PT with tapered edges. The stress is much more evenly distributed along the PT.	50
Figure 34: Electric potential for a 150mm PT at 30 MPa.	51
Figure 35: Von Mises stress profile for a 150mm PT at 30 MPa peak. The stress is much more evenly distributed than shown in Figure 19.	51
Figure 36: Diagram of setup with electroded crystal. The input and output dimensions are labeled l_1 and l_2 respectively. (a) Signal generator, (b) Impedance matching transformer, (c) Current transformer, (d) Input voltage Monitor, (e) Variable impedance capacitive probe.	55
Figure 37: Picture of atmospheric test stand.....	56
Figure 38: Impedance Matching Transformer.....	56
Figure 39: LL Impedance Matching Network	58
Figure 40: Picture of LL network	58
Figure 41: Because of its high output impedance, the PT gain can be affected by low diagnostic impedance [17].	59
Figure 42: The diagnostic impedance (b) is increased by adding a series variable gap distance capacitor (a) with a very small capacitance.	60
Figure 43: The attenuation of the high impedance diagnostic was increased by increasing the gap distance in the variable capacitor.	61

Figure 44: Location of PT holder	62
Figure 45: By holding the PT near its vibration null, its gain was increased. 62	62
Figure 46: Bremstrahlung Radiation Measurement	64
Figure 47: x-ray diagnostic trigger scheme	65
Figure 48: A tungsten etched field emission tip (a). The tip was very fragile and difficult to move without bending (b).....	67
Figure 49: A Pt-Ir cut field emission tip.....	68
Figure 50: PT with aluminum electrodes, signal wires, and field emission structures attached. The PT is compared to a stick of gum (Juicyfruit) for scaling comparison.....	69
Figure 51: Pulsed flashover test setup. A 4 mm gap was formed between electrodes on a LiNbO ₃ sample. Flashover occurred at 6.24 kV, 180 kV/cm near the electrode triple point.	69
Figure 52: The measured input impedance of the PT close to the half wavelength frequency. Near resonance, the input impedance decreases. ...	71
Figure 53: The BVD equivalent circuit for a piezoelectric transducer. The left side represents the capacitance formed from the input, and the right side accounts for the mechanical vibration [35].....	73
Figure 54: Measured input impedance (blue) and input impedance of an equivalent circuit (green) determined by curve fitting.....	75
Figure 55: Parylene could be added to only a small region as demonstrated by the dashed box in order to minimize mechanical loss. The experiment diagram is shown; (a) RF source, (b) rotated Y-cut LiNbO ₃ , (c) field emission structures and target, (d) parylene deposition of length, L	80
Figure 56: Gain at low voltage operation for all configurations centered on the average resonant frequency.....	82
Figure 57: Loss factor vs. parylene length.....	84
Figure 58: Initial Output Voltage.....	86
Figure 59: Initial Voltage Gain	86
Figure 60: PT gain will be reduced by relatively low load impedance [29]... 87	87
Figure 61: Increased Output Voltage	88
Figure 62: Increased Voltage Gain	88
Figure 63: Bremsstrahlung and Fluorescence at highest energy for titanium	91
Figure 64: Bremsstrahlung and Fluorescence under increased input voltages	92
Figure 65: Measured x-ray spectrum from highest frequency of experiment.	94
Figure 66: Measured output voltage with x-ray diagnostic compared to Simulated PT with 25 V_{applied} (50 V_{pp}). The PT providing the measured output voltage had a thin film of parylene which can contribute to loss.	95

Figure 67: Measured Gain from x-ray diagnostic compared to simulated gain with experimentally determined loss. The measured PT had a thin film of parylene which can contribute to loss. 96

Figure 68: Experimental setup to verify a bipolar output signal. The output signals were observed to be 180° out of phase. 99

Figure 69: The output voltage from the bipolar configured PT. 99

Figure 70: Bipolar high voltage test circuit 100

Figure 71: Spectrum from the bipolar arranged PT 100

LIST OF TABLES

Table 1: Peak simulated electric field for various modes of operation.....	35
Table 2: Parameters for LL impedance matching network. Parameters were found by using a iterative curve fitting technique.	58
Table 3: Values for equivalent circuit determined by curve fitting to match input impedance.	74
Table 4: Summary of flashover events during high voltage tests.....	78
Table 5: High voltage PT summary.....	83
Table 6: Peak measured x-ray energy at several applied input voltages.....	93

Abstract

Detection of nuclear or fissile materials is made difficult due to the speed, quantity and variety of entrance points of transported goods in a global market. Inspecting transported goods under these conditions requires a convenient and portable device that uses proven methods. Active nuclear detection can be performed by using neutrons to induce a nuclear reaction in a radioactive material which can then be detected by an appropriate sensor. The University of Missouri is developing an ultra compact deuterium ion accelerator to induce D-D fusion as a source of neutrons for detection purposes. The proposed accelerator utilizes a lithium niobate piezoelectric transformer capable of producing a 100 kV output when driven with a low radio frequency resonant voltage. The transformer is a Rosen type transformer composed of a rotated y -cut polarized rectangular crystal, with the primary voltage applied through the crystal's thickness and the secondary developed along its length. The transformer will be used to supply and accelerate deuterium ions by field emission from a tip attached to the crystal's output electrode. The deuterium ions then impact a deuterated target inducing a $D + D \rightarrow {}^3\text{He} + n$ reaction. Advantages of this circuit include low power consumption, quick turn on, and compactness.

A resonant piezoelectric transformer circuit was developed for high voltage generation. The goal of this project was to produce 100 kV with a reasonably sized piezoelectric crystal. Several mechanisms leading to less

than expected high voltage have been addressed. This project addresses problems associated with high power, high stress, high voltage, mechanical loss, and high output impedance measurements. A method for eliminating unwanted discharges and a technique for measuring the true output voltage of the transformer were tested. A way to minimize the mechanical stress while creating high voltage was sought. The research performed in this project extended the state of the art for high voltage piezoelectric transformers.

1. Introduction

Compact Active Interrogation

In order to prevent the transportation of nuclear or fissile materials, especially Special Nuclear Materials (SNMs), through common shipping routes, detection methods must be implemented. Detection of these materials is difficult due to both the speed of transported goods, and variety of entrance points in a global market. The large volume of these goods shipped to the United States provides ample opportunity for nuclear or fissile materials to be hidden inside shipping containers [1]. Fast, reliable, and portable methods for detection of these materials must be developed to protect the United States from attack.

While it is possible to detect the natural emission of neutrons and gamma rays from both ^{235}U and ^{239}Pu , the decay products can be attenuated by objects, or shields, between the initiation source and the detector [2]. As a result, passive scanning of a fissile material may be inaccurate. Alternatively, active interrogation provides a method to encourage measurable fission reactions and increase radiation such that detection of SNMs inside of containers is much more likely [3]. Many techniques for active interrogation have been considered [4, 5, 6].

One method that has produced positive results is neutron active interrogation. By introducing neutrons from various sources to SNMs, specific nuclear reactions take place producing signature neutrons and gamma rays [7]. This can make detection possible even in shielded containers. Some of the forms of neutron active interrogation are discussed in [8]. Neutron active interrogation is scalable and can be used in smaller scale detection applications such as at post offices or office buildings, or in larger scale detection applications such as at shipping ports.

In order to make active interrogation feasible for use at many locations, smaller scale devices must be developed. A compact active interrogation device that can be quickly carried to new locations and implemented for detection purposes would fit this need. In most environments, the ability to quickly turn on and turn off the active interrogation device would further extend its usefulness.

Neutron Sources

Portable Active Interrogation

Because of their usefulness in active interrogation, many neutron source topologies are being considered. Some of these sources are useful for large scale detection purposes and require large accelerators to create high energy neutrons and a large neutron flux. The “Nuclear Carwash” is a concept proposed by Slaughter for active interrogation of large objects [2].

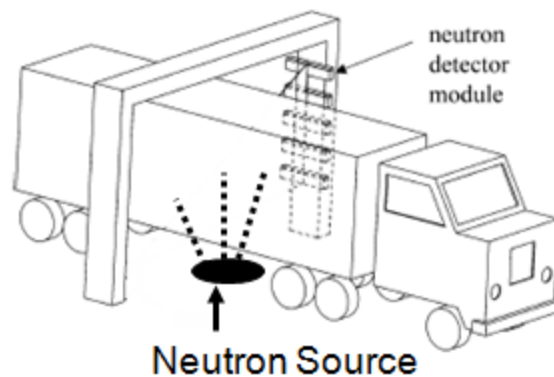


Figure 1: Example of a large scale neutron source concept for active interrogation of shipping containers [2].

The architecture shown in Figure 1 has many benefits, however it is not portable. Objects will need to be brought to the source for interrogation. Portable neutron sources will fill the need for interrogation of smaller objects in remote locations.

Several portable systems to create neutrons have been designed for use in active interrogation [3], however new methods are being studied [9]. Recent publications have described using pyroelectric properties of specific

crystals to create the deuterium ions necessary for D-D fusion [14]. This process creates field emission by thermally stimulating pyroelectric crystals as described by Rosenblum [10]. The pyroelectric properties of specific crystals generate large electric potentials which are used to drive a field emitting tip for ion production.

The piezoelectric properties of lithium niobate (LiNbO_3) crystals have also been used for ion production [16]. A Rosen type piezoelectric transformer (PT) can be used to create high electric potentials on an output electrode [11]. Some simulations indicate that with a specific geometry, it is possible to produce 100 kV on the output electrode with less than 1 kV applied. A field emitting point fixed to the output electrode can be used to field ionize deuterium gas, or emit deuterium ions by field emission. The potential is then used to accelerate the ion into a deuterated target resulting in D-D fusion.

D-D fusion

A deuterium-deuterium (D-D) fusion reaction can be used to produce neutrons of an appropriate energy for active interrogation [12]. A deuterium ion beam accelerated into a deuterated target results in ^3He plus one ≈ 2.5 MeV neutron. In order for D-D fusion to initiate, deuterium ion energies, E , of at least 30 keV must be reached [13]. Because the cross sectional, σ , of the D-D fusion reaction scales with energy, higher energy ions on the order of 100 keV are desirable [14]. At 20 keV the cross section for D-D fusion is approximately zero, however at 100 keV σ is increased to $16.3 \times 10^{-27} \text{ cm}^2$ or

16.3 mb. The probability, P , that a neutron will be produced by D-D fusion is demonstrated by Equation 1 where the N is the deuterium atom number density and the factor of one-half is included because only about one-half of the fusion reactions produce neutrons [15].

$$P_{neutron} \propto \frac{1}{2} N \sigma [E(x)]$$

Equation 1

$$E(x) = E_0 - \int_0^x \frac{dE}{dx}(x) dx$$

Equation 2

Piezoelectric Theory

The piezoelectric effect is widely studied for its use in power conversion circuits [16]. Piezoelectric transformers (PTs) are light, compact, unaffected by electrical noise, and can withstand high energy densities [17, 18]. These characteristics make them useful for many applications including power supplies for electronic devices [19], plasma sources [20, 21], and step-up ratio transformers [16, 22].

Piezoelectric materials are composed of an arrangement of a polarized material that is in a neutral state due to a symmetrical distribution of charge. By deforming the material, a charge can be created from a realignment of the polarized structure. This produces a voltage across a separation distance which can also be described as an electric field.

Piezoelectric devices exhibit strong frequency dependence through which electrical and mechanical energy are coupled. Acoustic waves traveling through the device can result in a variety of resonance vibration modes [23]. The modal frequency for various types of devices depends on parameters including physical dimensions and material properties. Basic geometries and materials are described in a number of texts including [24, 16]. Typical high voltage geometries include beams or plates driven into a variety of extensional modes.

In a beam geometry, by squeezing through the thickness, the piezoelectric material height, h , will be reduced to h' . This is in agreement with Hooke's Law, where applied force is equal to some displacement constant times the displacement distance. The displaced material will be forced in a new direction, such as along the length of the beam. The beam length, l , will be increased to l' . An example of the original state and deformed shape from this process is shown in Figure 2. For the example shown the stress, T , is due to an electric field, E . Much like squeezing a rubber eraser the material is forced to expand in all outward directions except the thickness. Because the material has piezoelectric properties, an electric signal can be harvested due to the electric displacement that occurs.

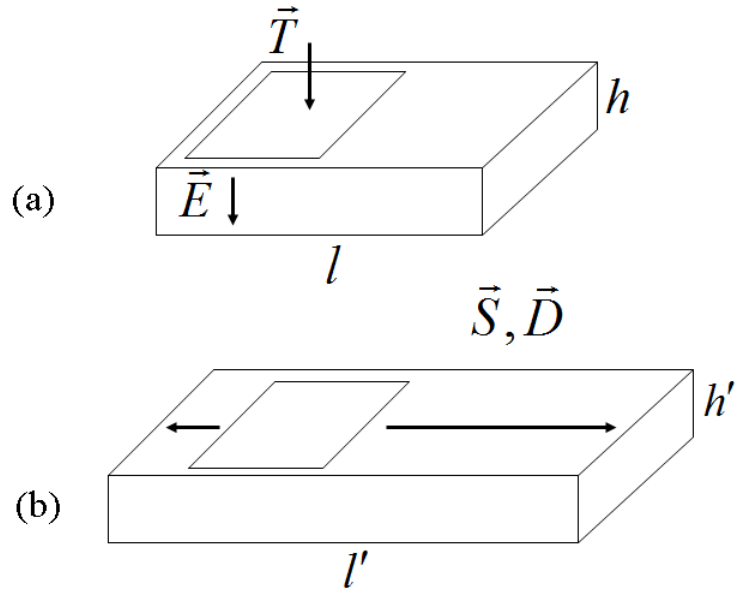


Figure 2: Piezoelectric beam or plate squeezed through the thickness (a) prior to being deformed and (b) after deformation has occurred along the length.

Rosen type PTs have been analyzed in many papers since they were proposed by Rosen in 1957 [11]. These transformers are composed of a rectangular piezoelectric material to which an electric signal is applied through the thickness at one end. The strain induced by the input signal is electromechanically coupled to the output end of the bar in the form of longitudinal acoustic waves. The deformation of the polarized material creates large electric fields at the output which are used to produce voltage and current.

The state of the piezoelectric crystal can be described by the fundamental equations of piezoelectricity. Two equations are used to relate the electrical and mechanical state of the device. These two equations are

shown in Equation 3 and Equation 4 where T is strain, S is stress, E is electric field and D is electric displacement.

$$T_{ij} = c_{ijkl}S_{kl} + e_{kij}E_k$$

Equation 3

$$D_i = e_{ikl}S_{kl} + \varepsilon_{ik}E_k$$

Equation 4

Because the piezoelectric device is anisotropic, the coefficients c , e , and ε that are used in Equation 3 and Equation 4 have different values in different geometrical directions. The coefficient c is the elasticity of the material and relates stress and strain. The coefficient ε is the permittivity of the material and relates the electric field to electric displacement. The coefficient e is the piezoelectric coefficient that relates the electric field and electric displacement to stress and strain.

Under normal operation of a piezoelectric device mechanical deformation takes place. The equation of motion is used to describe the physical displacement, u , of material and relate that motion to stress in the material. The equation of motion is shown in Equation 5.

$$T_{ij,i} = \frac{\partial T_{ij}}{\partial x_i} = \rho \ddot{u} = \rho \frac{\partial^2 u}{\partial t^2}$$

Equation 5

The displacement of material can occur in any direction. The directional derivative of displacement, $\frac{\partial u}{\partial x}$, describes strain. Equation 6 describes strain in a solid object.

$$S_{ij} = \frac{1}{2}(u_{i,j} + u_{j,i})$$

Equation 6

The analysis of a flat bar type piezoelectric device takes advantage of the geometry of the device to make several assumptions. In length extensional vibration of a flat bar, displacement only occurs in one direction, x_1 , as demonstrated in Equation 7. Similarly, there is no variation in displacement along the plane of motion as demonstrated by Equation 8. The directions x_1 , x_2 , and x_3 , are shown in Figure 3.

$$u_2 = u_3 = 0$$

Equation 7

$$\frac{\partial u_i}{\partial x_2} = \frac{\partial u_i}{\partial x_3} = 0$$

Equation 8

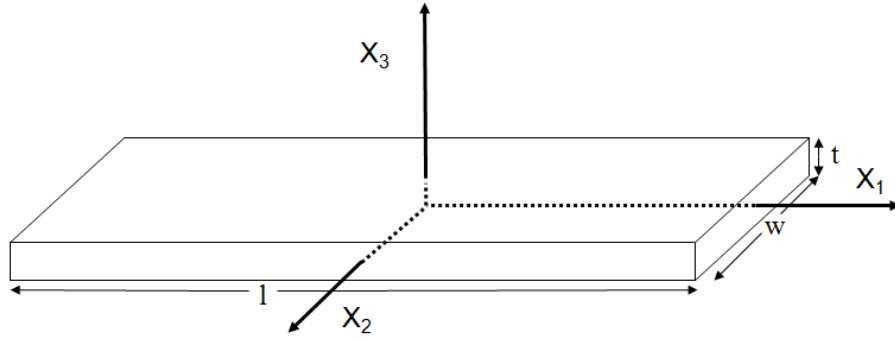


Figure 3: Bar shaped crystal and orthogonal directions

With these conditions, the fundamental equations can be developed into the equation of motion, shown by Equation 9, and valid over the entire length of the device. At its ends, the device is unbounded and stress at those locations is zero.

$$\frac{\partial T_{11}}{\partial x} = c \frac{\partial^2 u}{\partial x^2} = \rho \ddot{u}_1 \quad -l/2 < x_1 < l/2$$

Equation 9

Rearranging the equation of motion will produce Equation 10 which describes the time and position dependence of displacement.

$$\frac{\partial^2 u_1}{\partial x^2} - \frac{\rho}{c} \frac{\partial^2 u_1}{\partial t^2} = 0$$

Equation 10

Assuming u_1 is a function of position and time, and has oscillating form as shown in Equation 11, u_1 can be solved as shown in Equation 12.

$$u_1(x,t) = u_1(x)e^{i\omega t}$$

Equation 11

$$\ddot{u}_1(x,t) = -\omega^2 u_1(x,t)$$

Equation 12

Substituting for the final form of the equation of motion produces Equation 13.

$$\frac{\partial^2 u_1}{\partial x^2} + \frac{\rho}{c} \omega^2 u_1 = 0$$

Equation 13

The solution for displacement from Equation 13 is shown in Equation 14. Displacement occurs along the length of the device.

$$u_1 = \sin(kx) \quad k = \omega \sqrt{\frac{\rho}{c}}$$

Equation 14

Length extensional resonance occurs in the piezoelectric device when a standing wave is developed. The resonant frequencies can be solved from Equation 14 and is shown by Equation 15. The half wavelength and full wavelength modes were simulated using a finite element solver [25] and are shown in Figure 4.

$$\omega_n \sqrt{\frac{\rho}{c}} \frac{l}{2} = \frac{n\pi}{2}$$

Equation 15

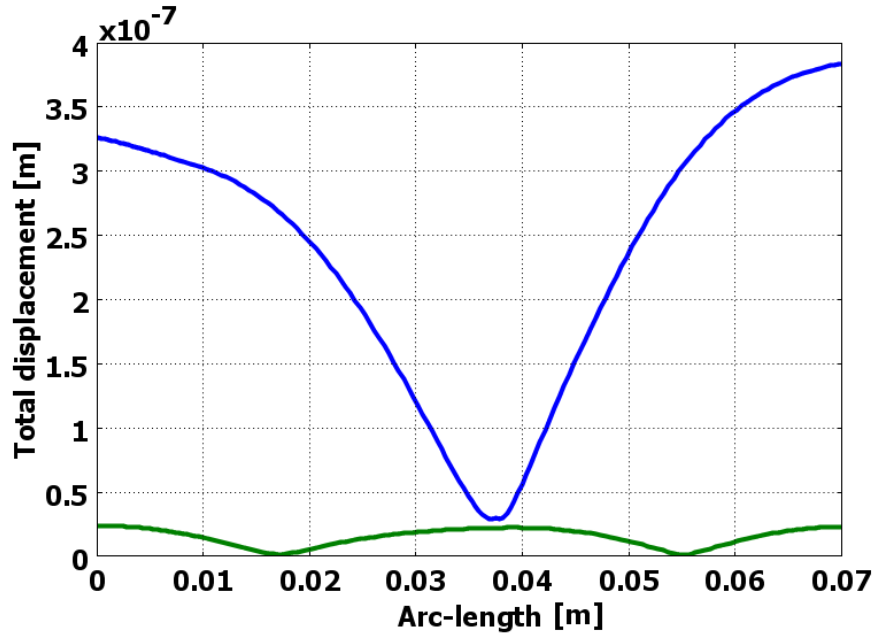


Figure 4: Displacement of a piezoelectric bar under length extensional resonance at the half a full wavelength resonance modes. A vibration null occurs near the center of the PT at 0.0375 meters.

The displacement of the piezoelectric material results in the material undergoing a certain amount of strain. The magnitude of the relative displacement, i.e. the directional derivative of the displacement, provides insight on where peak strain occurs. Figure 5 shows the directional derivative of displacement of a 70 mm PT undergoing half-wavelength resonance. The peak strain is located near, but not at, the displacement null of the longitudinal standing wave.

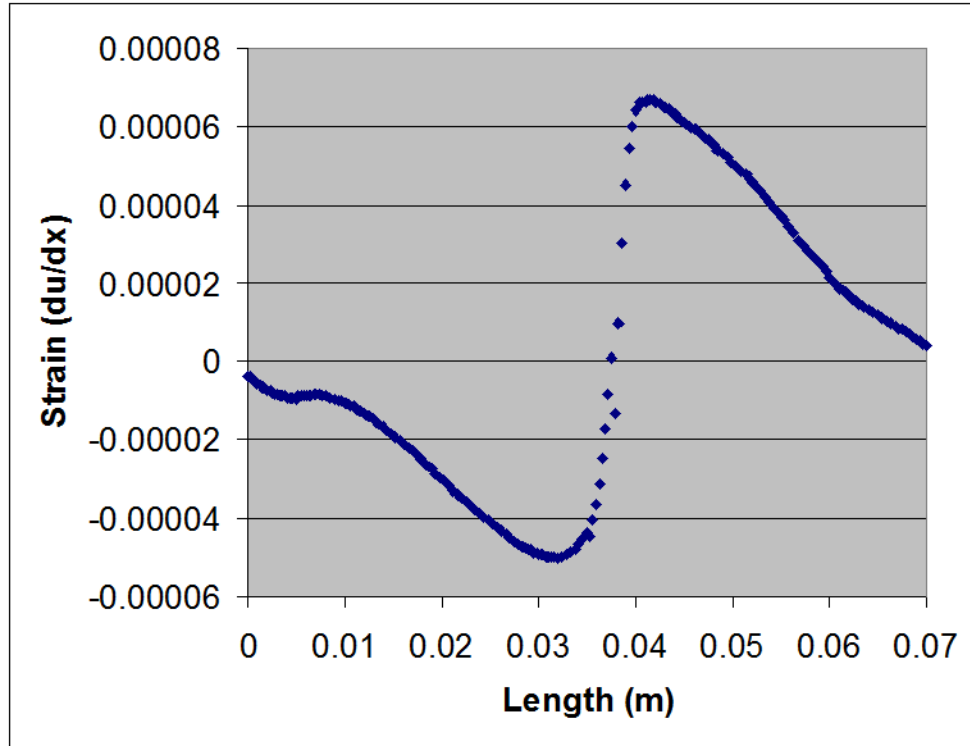


Figure 5: The directional derivative of the piezoelectric material under half wavelength resonance.

When a material is under stress due to displacement, the total stress can ultimately lead to fracture of the material. One method to predict the fracture point of a material is to compare the total stress of the three principal directions to the von Mises yield criterion. The von Mises yield criterion is the point at which the von Mises stress exceeds its maximum value for a particular material. The von Mises stress, σ_v , is calculated from the principal stresses, σ_1 , σ_2 , and σ_3 , as shown in Equation 16 [26].

$$\sigma_v = \sqrt{\frac{(\sigma_1 - \sigma_2)^2 + (\sigma_2 - \sigma_3)^2 + (\sigma_3 - \sigma_1)^2}{2}}$$

Equation 16

The von Mises yield criterion of LiNbO_3 is reported to range from 30 to 120 MPa [27]. For a high voltage PT, fracture can occur at von Mises stress above this range. In high voltage PT design, it is convenient to use simulation software to find the von Mises stress of a particular design.

High Voltage Piezoelectric Transformers

Lithium Niobate (LiNbO_3) crystals have been considered for use in piezoelectric devices for several decades, in part due to very low losses compared to ceramic piezoelectric materials. The material properties of LiNbO_3 are described in [28].

Recent experiments by Nakamura and Adachi [29] have utilized a singly polarized rotated Y-cut LiNbO_3 crystal oriented similar to Rosen type transformers. This arrangement has had success as a high voltage ratio transformer, reaching output voltages of several kV. The output to input voltage ratio is large due to the Rosen type geometry as shown in Equation 17, where L is length, and T is thickness of the device. This is because the geometry is very long when compared to its thickness. Also, the low loss of LiNbO_3 results in a high Q factor, and the transverse coupling factor for length-extensional vibration, k_{23} , and for longitudinal vibration, k_{33} , is higher for LiNbO_3 than coupling factors for ceramic Rosen transformers.

$$\frac{V_{out}}{V_{in}} \propto k_{23}k_{33}\frac{Q}{T}$$

Equation 17

Nakamura and Adachi showed in [29] that the product of the coupling factors, k_{23} and k_{33} , is highest at an angle of $\sim 135^\circ$ as referenced in Figure 6 and shown in Figure 7. A rotated Y-cut Rosen type PT, with a long length compared to thickness can be used to create transformers with a high voltage gain.

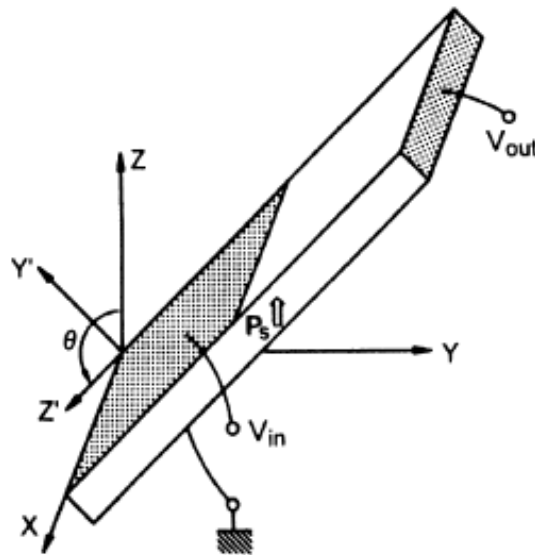


Figure 6: 135° rotation [29]

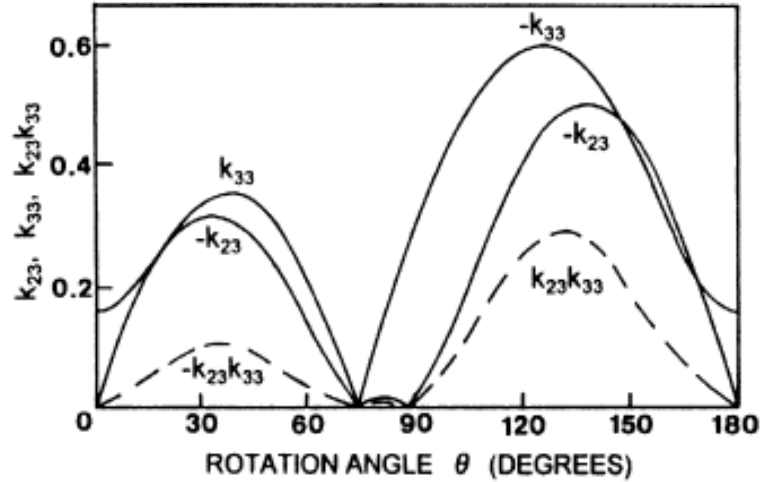


Figure 7: Rotational affect on coupling coefficients [29]

In order to reduce the output impedance of the PT, an electrode is frequently attached to the crystal surface [29]. This electrode will electrically connect regions of higher potential to regions of lower potential effectively shorting out the highest voltage region of the PT. The available charge that can be liberated from the PT for driving a load is proportional to the electric displacement of the material at the output electrode [30]. This is shown by Eqn. 16 where Q is charge, w is width of the output electrode, and l_{out} is the length of the output electrode. As a result of Equation 18, the available output current also scales with output electrode size as shown in Equation 19.

$$Q = -w \int_{l_{out}} D \cdot dx$$

Equation 18

$$I_{out} = -\dot{Q}$$

Equation 19

As the frequency of the applied signal approaches an acoustic resonant frequency, mechanical energy is stored in the device contributing to higher displacement and thus higher output voltage. The resonant frequency depends on the dimensions and material properties of the PT. Near resonance, the input impedance is very small. There are associated anti-resonances at which point the input impedance is large. Figure 8 demonstrates a calculation that predicts the location of the resonant frequencies for different modes of the device when taking into consideration the materials and dimensions. The intersection points, ω_1 and ω_2 , represent half and full wavelength resonant frequencies where a half and full acoustic standing wave are created in the crystal. The asymptotes represent anti-resonance.

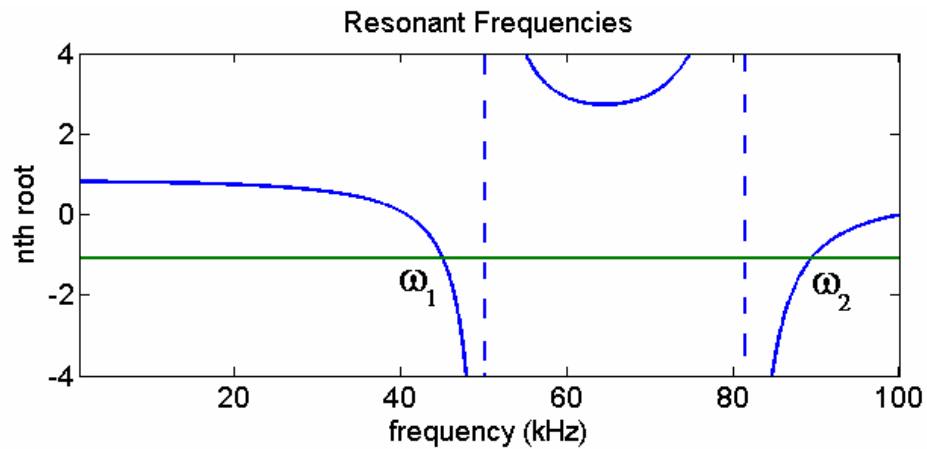


Figure 8: The resonant frequencies are predicted using the physical properties of LiNbO3 and the geometry of the transformer. Intersection points represent the half and full wavelength resonant frequencies and asymptotes represent anti-resonance.

Project Overview

In this document the design and testing of a Rosen type PT for high voltage generation is presented. In general, high voltage and high gain were measured from the PT. A comparison was made between the PT simulations and measured values. Methods to accurately measure the output voltage were developed. Interesting design changes were investigated to push the limits of high voltage generation by a Rosen-type PT.

In chapter 2, finite element simulations are presented for several different purposes. First, the proposed PT architecture was simulated in order to demonstrate that a high voltage gain signal could be generated from the PT. Several design physical variables were then changed to determine

their importance in the performance of the PT. These variables included things such as electrode geometry and material loss. Finally, simulations were performed to predict the limits of high voltage generation for the PT. Methods to increase the available output voltage are presented.

In chapter 3, the various setups that were used for experimentation are presented. High voltage tests were performed in atmosphere and in vacuum, and the layout and diagnostics for these tests are described. Because the PT had high output impedance, special diagnostics were developed to avoid loading down the PT. These diagnostics included a variable capacitance probe and an x-ray emission and detection technique. In addition a test procedure for LiNbO₃ flashover measurements is described.

In chapter 4, an analysis of several experiments is made. Laboratory measurements are discussed that confirm several ideas presented in the simulations. The input impedance of the PT was measured used to calculate the mechanical loss. Gain predictions were made possible by this calculation.

The flashover strength of LiNbO₃ was explored, and a way to prevent flashover by thin film encapsulation is presented. The thin film was found to inhibit flashover at the expense of added mechanical loss. A way to minimize the mechanical loss and prevent flashover is discussed.

Data from the high impedance voltage diagnostics are presented. The variable capacitance was able to increase the measureable voltage in atmosphere. In vacuum, the x-ray diagnostic was able to measure the

output voltage of the PT at close to its peak predicted amount. The laboratory measurements confirmed high PT gain.

The peak stress in the PT under high voltage generation is also discussed. In order to generate 100 kV with the PT, the von Mises stress criterion was surpassed resulting in several broken PTs. The output voltage from the bipolar redesign technique discussed in Chapter 2 was measured. A bipolar output signal was created by the PT to increase the available output voltage at a given stress.

In chapter 5, a summary of the dissertation is presented and suggestions for future work are made. While high voltage and high gain generated by the PT has been measured, 100 kV was not attained with the geometry used for laboratory measurements. Redesign methods might aid in attaining 100 kV with the PT.

2. Finite Element Simulations

Behavior of PT

For ion emission and acceleration to occur, high voltage must be developed on an output electrode. To determine if this was possible, the PT was simulated using a finite element code [25]. The simulations that were performed accomplished several tasks. First, they were used to verify that high gain and voltage could be generated by the proposed PT. Secondly, they were used to determine how important variables affected the operation of the PT. These simulations examined things such as electrode length and other boundary conditions. Thirdly, simulations were used to determine the theoretical output voltage based on a given peak PT stress. All of the simulations provided insights on PT design to provide the best characteristics for ion acceleration.

The FE software used in this project was Comsol Multiphysics [25]. In general, a guideline was followed to run a simulation. Because the Comsol interface was graphical, a text script is not available. However, a detailed simulation guideline is described in the appendix.

For a simulation, the specific PT design was drawn within the finite element graphical interface as shown in Figure 9. Then the following boundary conditions were applied. All surfaces were allowed to freely vibrate unless a particular restrictive boundary condition was desired. The oscillating driving signal was applied to the top of the input side of the PT, surface 1. The bottom of the input side, surface 2, was set as ground. The top output electrode, surface 3, of the of output voltage section was set to floating potential. On all other surfaces, a zero charge boundary condition was set.

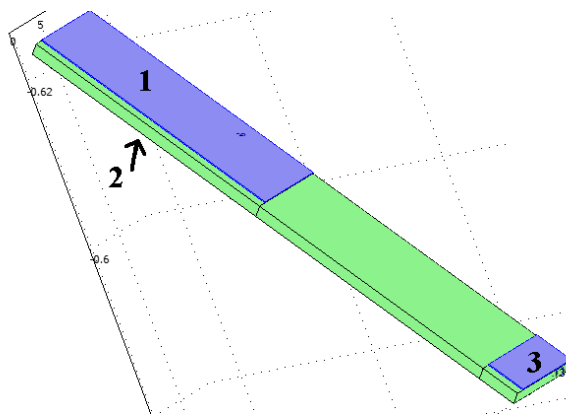


Figure 9: The PT with electrodes drawn in the finite element software graphical interface.

High Voltage Gain

To determine the gain of a realistic PT, a radio frequency (RF) signal was applied through the thickness with a 1 V amplitude, and the output potential was developed along the length of the device. This configuration was consistent with many typical Rosen-type PTs [30]. The frequency was swept over a range that included the half wavelength resonant frequency. Figure 10 shows a simulation of the surface potential developed along the surface of the 70 mm PT near resonance. The simulated output voltage and thus transformer voltage gain was 843. This indicated that 100 kV can be generated with 120 Volts applied.

This simulation shown in Figure 10 was performed with the most accurate PT physics as determined by the entire experiment process. Important conditions included the dielectric and mechanical loss factors for LiNbO_3 . The dielectric loss factor is assumed to be relatively constant for a wide frequency range up to and including 9 GHz. The dielectric loss factor was found by Ohmachi to be 0.0013 at 10 kHz, which is near the PT operating frequency of 45 kHz [31]. The mechanical loss factor was determined experimentally with the PT equivalent circuit. The process is described on page 70. The experimentally determined mechanical loss factor was found to be 0.00188. This value included any coupling losses, e.g. electrode to crystal, because they were indistinguishable with the equivalent circuit.

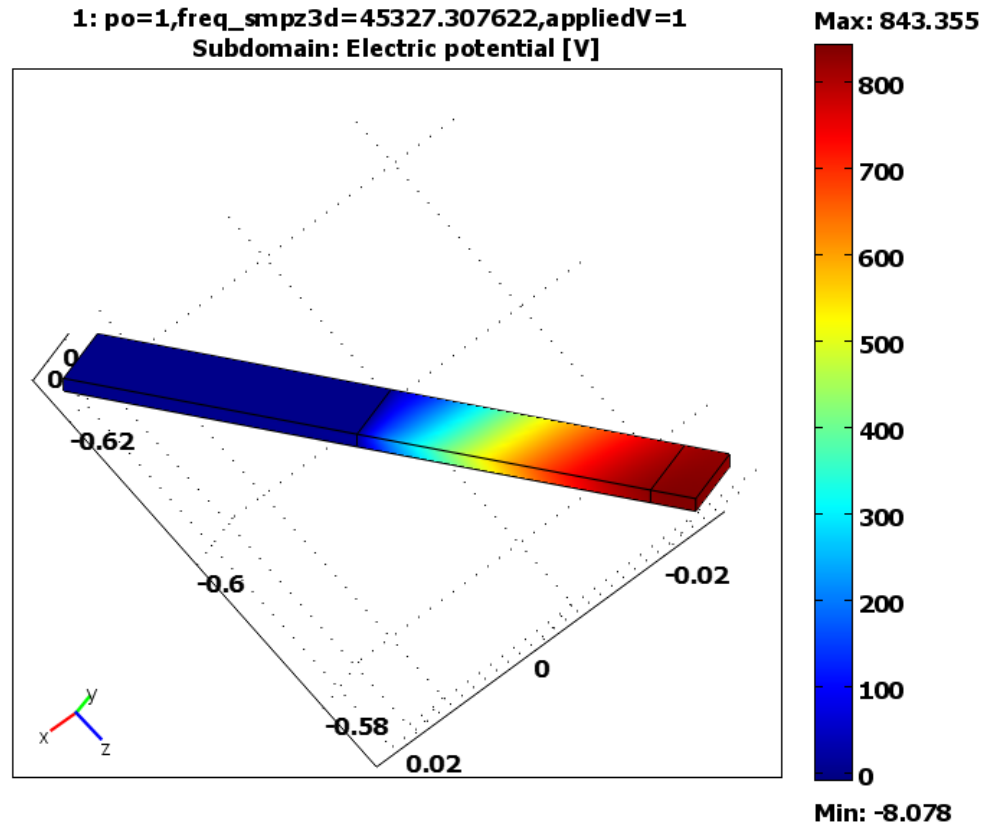


Figure 10: Simulated electrical potential on PT surface

This simulation was also used to discover the true null vibration point on the 135° rotated Y-cut LiNbO_3 crystal. The null point was found to be located 32.5 mm from the input side of the PT. The null point corresponds to the point at which the least displacement occurs for piezoelectric material. For bar shaped PTs, the null point is useful for physically holding the PT [16]. The displacement null points for the half-wave and full-wave modes are shown in Figure 4 and correspond to the regions of least displacement.

As stated, for the simulation shown in Figure 10, loss factors were introduced to account for losses in the LiNbO_3 . Loss decreases the performance of the PT and is therefore important to include when evaluating a PT. However, some of the simulations that were performed did not include loss. The measured response in these simulations can only be used for comparisons between specific variables within the simulation. The determination of the correct loss factors for use in simulations are discussed later in this document.

Once the possibility of high voltage was established, a series of simulations were performed to simulate the operation of a high voltage PT. The software was used to predict how varying several parameters affected the way the PT performed. The particular parameters that were examined include the device length, the length of both input and output electrodes, thickness of electrodes, material loss, and additional electrode mass (e.g. wire). Device responses such as gain and displacement were compared between simulations. All parameters were found to affect the performance of the device.

The ability of a simulation to provide insight to a real system can be improved by adding additional physical phenomena to the solution. For the simulations presented in this paper, simulation fidelity was improved by adding elements such as an output electrode, electrode thickness and real loss as the sequence of simulations progressed. Early simulations examined

the effect that some parameters had while ignoring some of these components.

Near resonance, slight variations in frequency can have a very large effect on the operation of the PT. In order to compare the performance between multiple PTs, a procedure was developed to avoid accidental bias. The developed method involved finding the frequency at the full wave half max of the output voltage in frequency space. The Eigen frequency for length extension vibration was found using Comsol.

The quality factor was then calculated and the half max value was recorded. The frequency that was used for further tests was the frequency at full wave half max on the low side of the resonant frequency. In Figure 11 this corresponds to the frequency at the left side of Δf .

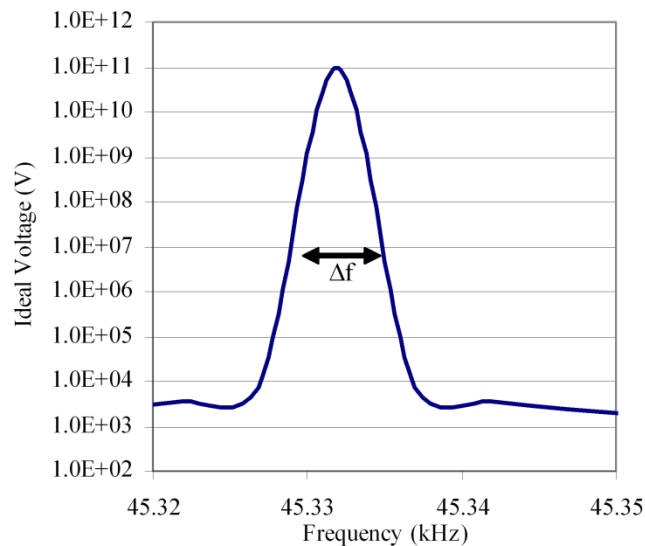


Figure 11: Measurements were recorded at the frequency according to the FWHM of the output voltage

The first simulation test was performed to verify the effect of acoustic velocity for the rotated y-cut PT. The resonant frequency near 45 kHz was solved for three different length PTs: 60, 70, and 80 mm. Figure 12 shows that as the device length was increased the resonant frequency was reduced. The acoustic velocity which can be calculated with Equation 20 remained constant for all values of d: 30, 35, and 40mm. The acoustic velocity for a rotated y-cut piezoelectric transformer was found to be 3170 m/s which was consistent with literature [27]. This proved that the resonant frequency near this frequency range was determined by the length of the device as was expected for length extensional vibration.

$$f_{res} = \frac{V_A}{2d}$$

Equation 20

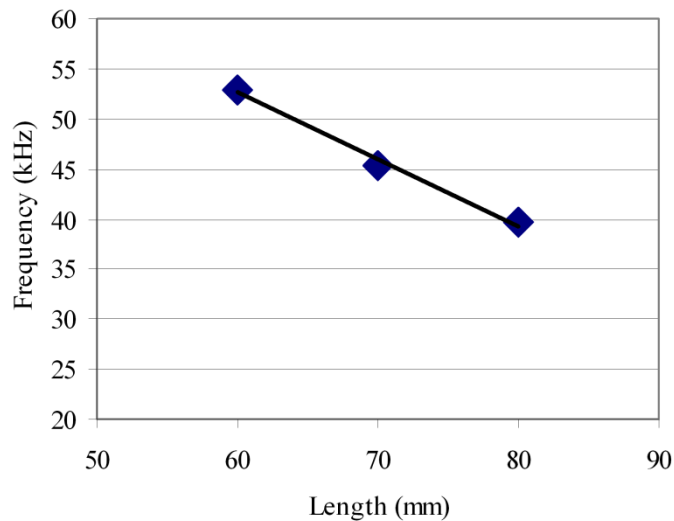


Figure 12: Increasing the length of the device reduced the resonant frequency

In order to confirm that the PT was behaving as a transformer, the gain of the device was examined. The input voltage was varied from 1 to 100 Volts and the potential along the length of the device was recorded as shown in Figure 13. The output voltage was observed to increase by a factor equal to the increase of input voltage. This simulation demonstrated that the output voltage was a valid response to use for comparison as simulations were developed to include the increasingly complex model parameters such as loss.

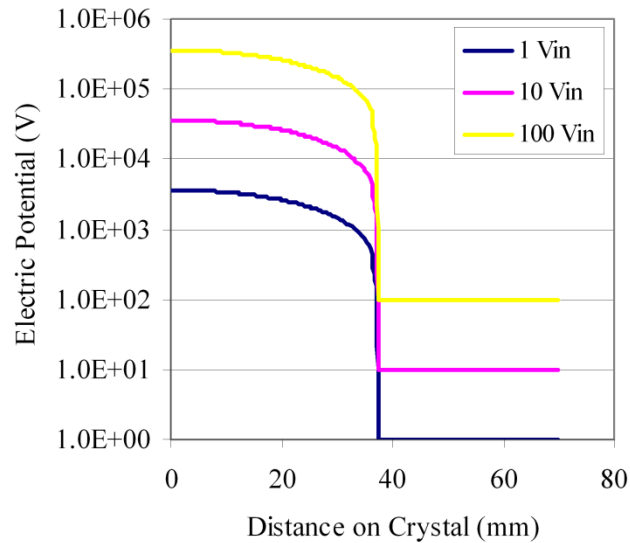


Figure 13: Increasing the input voltage produced a greater output voltage. This demonstrated a true transformer gain effect.

The electrode on the input side of the device was then varied for a PT that was 70 mm in length to determine the optimal length of the electrode. Three values of input electrode length were examined: 30, 32.5 and 35 mm. These values were chosen because they demonstrate the operation of the device with an input electrode edge at a location less than, approximately

equal to, and greater than the null point. The simulations shown in Figure 14 demonstrate that the location of the electrode had an effect on the potential that was developed along the length of the crystal. Because the 35 mm input electrode extended into the region of the device that developed the output voltage, regions of the output voltage were effectively shorted out to the input electrode. As a result, the output voltage was reduced when the input electrode length was greater than the predicted distance to the null point.

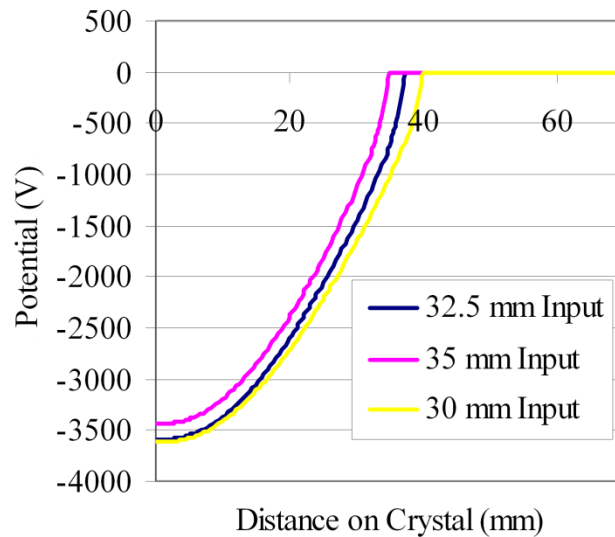


Figure 14: The length of the input electrode should be matched to the length of the device. An electrode greater than 46.5% of the length of the device decreased the peak output voltage.

Reducing the input electrode length below the distance to the null point was shown to produce the same output voltage as the matched electrode length. This was because the output voltage was generated from near zero at the null point to the end of the PT. A decreased input electrode

will not short out any region of developed electric potential. However, reducing the input length from the null point can prevent access to the null point for things like attaching wire. In addition, decreasing the size of the input electrode will reduce the amount of surface to which an electrical signal can be applied. This in turn reduces the maximum theoretical pressure that can be applied to the PT according to Equation 3 and Equation 4.

The length of the output electrode ranged from 0 mm to 15 mm. When the length of the output electrode was increased, it extended into the high voltage region of the PT. As a result, the high voltage that was generated by the tip of the PT was effectively shorted out by regions of lower voltage as shown in Figure 9. While a short output electrode is ideal for producing the highest output electric potential, increasing the output electrode can be useful for decreasing the output impedance of the device. This is possible by producing a larger output current according to Equation 18 and Equation 19.

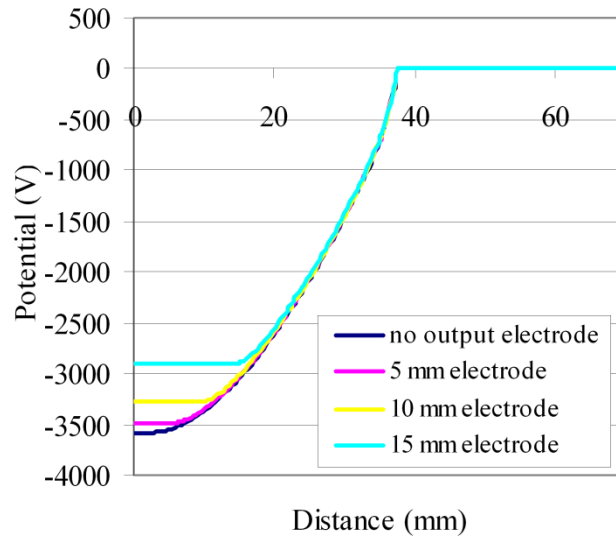


Figure 15: The length of the output electrode affected the peak voltage available at the electrode. A longer electrode decreased the output voltage, but can increase the output current according to Equation 19.

A loss factor was added to the LiNbO_3 material to determine how loss affected output voltage. As shown in Figure 16, the output voltage over the entire range of frequencies for a set input voltage was drastically reduced. The output voltage of the transformer was measured without loss and with both a dielectric loss and dielectric and mechanical loss. This indicated that the loss factor was a very important part of the operation of a real device. The simulation also indicated that the inclusion of a loss factor is necessary in future simulations for comparison purposes.

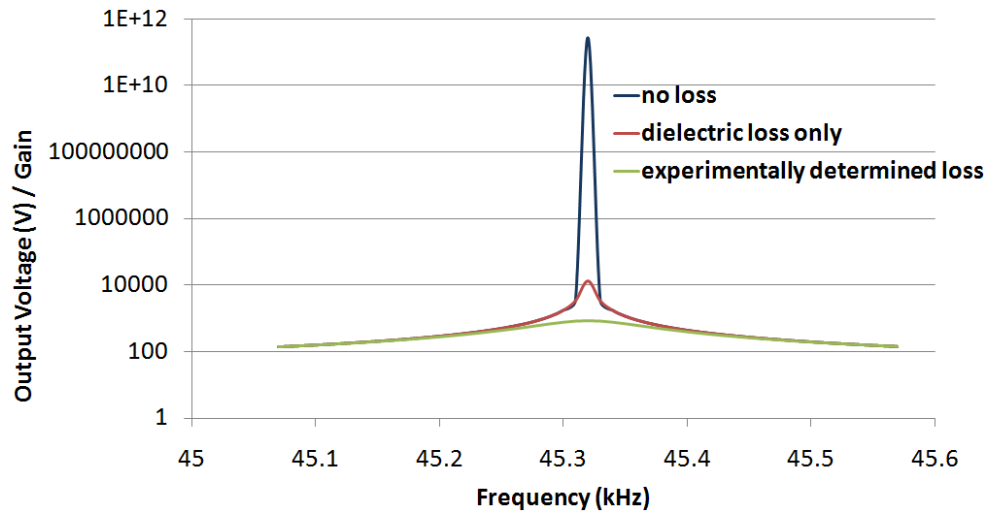


Figure 16: Introducing a loss factor to the LiNbO₃ greatly affected the performance of the device.

High Electric Field

When a high voltage pulse is being produced, the voltage profile along the length of the PT can result in a large electric field on the PT surface. The high electric field can then lead to unwanted discharges forming [29, 20]. The PT was simulated to determine the profile and magnitude of the electric field on the PT surface to help predict when and where flashover would occur.

The first electric field simulation was performed to determine the flashover strength of LiNbO₃ based on the results of a flashover test described on page 69. For this simulation 6.24 kV was applied to a 4mm gap of LiNbO₃. Aluminum electrodes of 1 μ m were used to apply the electric potential. These conditions were set to match the laboratory flashover experiment.

The resulting electric field is shown in Figure 17. Because of triple point field enhancement, the electric field near the electrodes is very high compared to the average electric field across the gap. From this simulation the electric field leading to flashover for LiNbO_3 was found to be approximately 180 kV/cm.

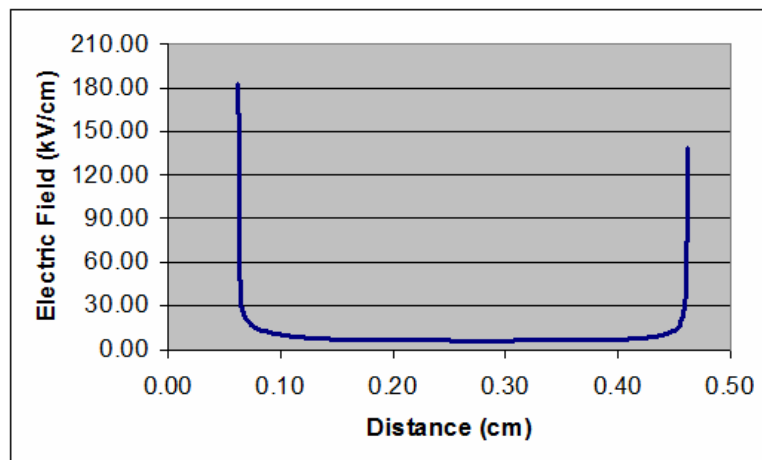


Figure 17: Electric field resulting in flashover

A finite element simulation was then used to determine the peak electric field that occurs while the PT was generating high voltage. The simulation was performed under several conditions in an attempt to discern the peak electric field as accurately as possible. In the simulation, 100 V was applied to the input electrodes and the output voltage and peak electric field was recorded. The location of the peak electric field was also determined and is shown in Figure 18.

When high voltage is generated with a PT at the half wavelength mode, a large electric field forms near the input electrode triple point. Simulations indicated that the magnitude of the electric field approaches 400 kV/cm depending on the electrode thickness. This is shown in Figure 18. The simulation confirmed that the peak electric field formed near the input electrode. The results of the simulation are summarized in Table 1. In each case, the peak electric field was recalculated assuming the PT was providing 100 kV on its output electrode.

It was clear from the experiment that the electric field on the PT surface would exceed the peak electric field for LiNbO_3 and could lead to flashover. The initiation point for the flashover appeared to be confined to a region near the input electrode triple point. Several methods to prevent flashover were considered in this project and are discussed on pages 36 and 77.

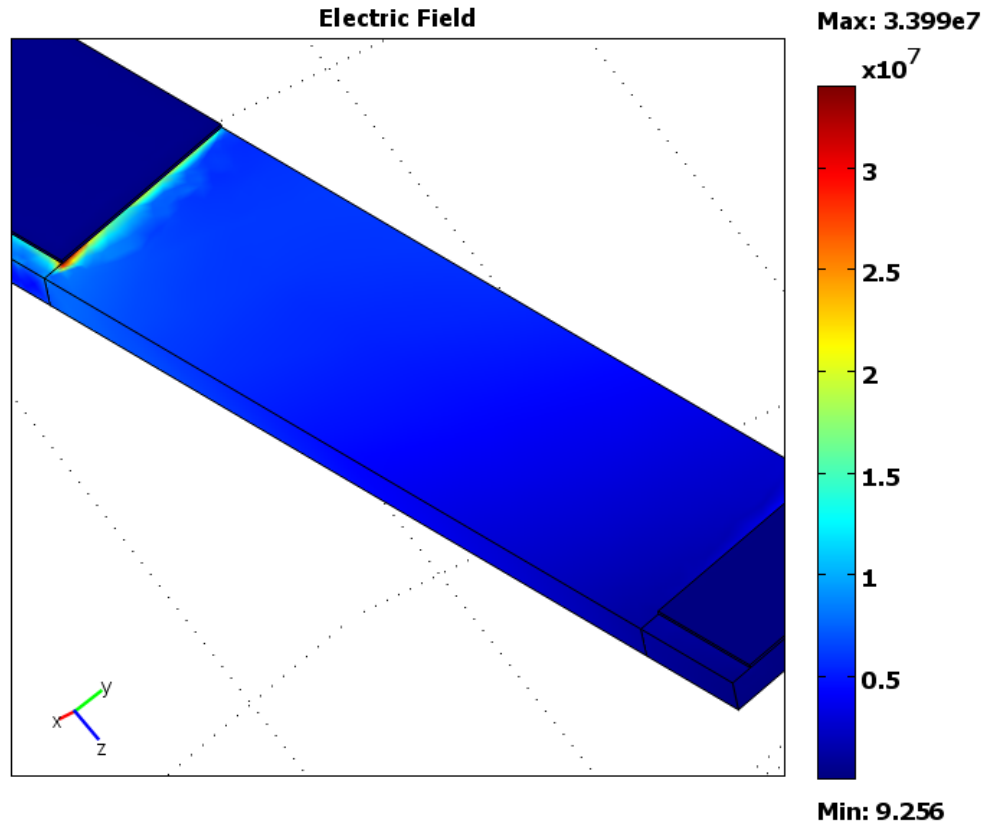


Figure 18: Location of high electric field due to triple point enhancement

Table 1: Peak simulated electric field for various modes of operation

	Peak Voltage (kV)	Peak Electric Field (kV/cm)	Peak Electric Field Adjusted for 100 kV (kV/cm)
At resonance	84.3	340	408
At FWHM	42	170	204

The peak electric field at the triple point was then examined based on the length of the input electrode. There were several minima in the electric field along the length of the PT found by simulation shown in Figure 19.

During experimentation, when the electrodes were deposited accordingly, the peak voltage acquired from the PT was increased slightly. However, the average electric field remained throughout the range of input electrode lengths.

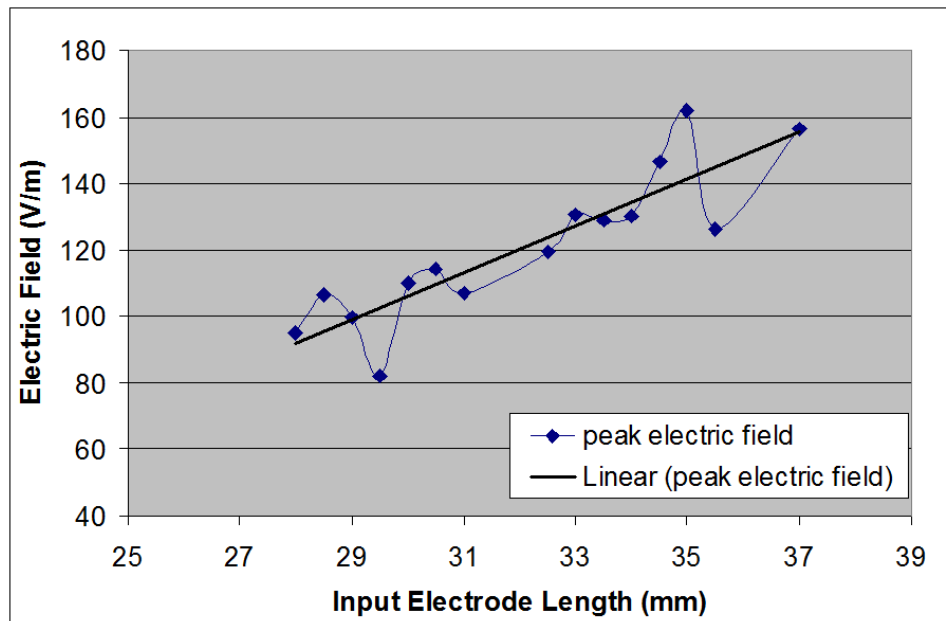


Figure 19: Electric field minima

Peak Output Voltage

The PT was simulated to determine its peak theoretical output voltage at the maximum stress level for LiNbO_3 . The peak stress that occurs while a piezoelectric device is undergoing mechanical deformation is one of the important factors that determine if the device will fail. The von Mises stress,

σ_v , is shown by Equation 16. The maximum von Mises yield stress for LiNbO_3 has been measured at 30 - 120 MPa [27]. Above this stress the LiNbO_3 will fracture.

For the PT used in this project, the peak stress that occurred can only be determined by finite element simulation. Aside from calculating the peak von Mises stress due to certain conditions, the only other indication for failure of a PT is if the device breaks under experimentation.

A simulation was performed to see if the von Mises stress criteria was surpassed when the PT fractured during an experiment. The laboratory experiments leading to a broken PT are described on page 97. For the simulation, the experimentally determined loss factors were used and the applied voltage and frequency were set to a value that experimentally resulted in a broken crystal.

The simulation provided the peak von Mises stress by sweeping through the phase of the displacement. The peak stress was found to be 34 MPa at the resonant frequency and an experimental voltage as shown in Figure 20. This simulation provided an explanation for the broken PT.

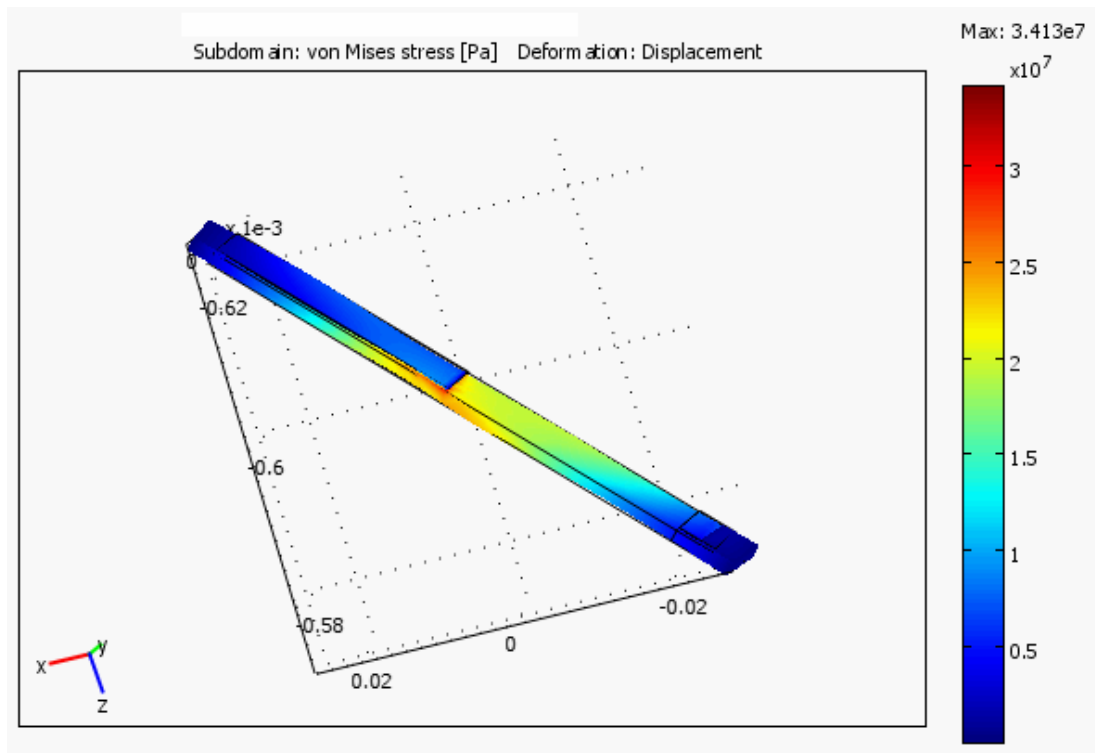


Figure 20: Finite element simulation of the PT under conditions which experimentally led to PT fracture.

This particular example of a broken PT occurred at a specific frequency with a specific applied voltage. A series of simulations were performed to determine the best operating region in terms of frequency and applied voltage. With more simulations and subsequent experimentation, the true peak output voltage before the PT is over-stressed was sought. Also, simulations were performed to find ways to modify the PT in order to reduce the peak stress.

To determine the best applied voltage and frequency for low stress operation, simulations were then performed to determine the stress that can

result from an applied voltage over a range of frequencies near resonance, f_0 . This is shown in Figure 21. By interpolation, the applied voltage that resulted in 30 MPa for each frequency was found.

A similar method was used to determine the output voltage of the PT due to an applied voltage over a range of frequencies. Again, interpolation was used to determine the applied voltage necessary for 100 kV production on the PT output electrode. The result is shown in Figure 22.

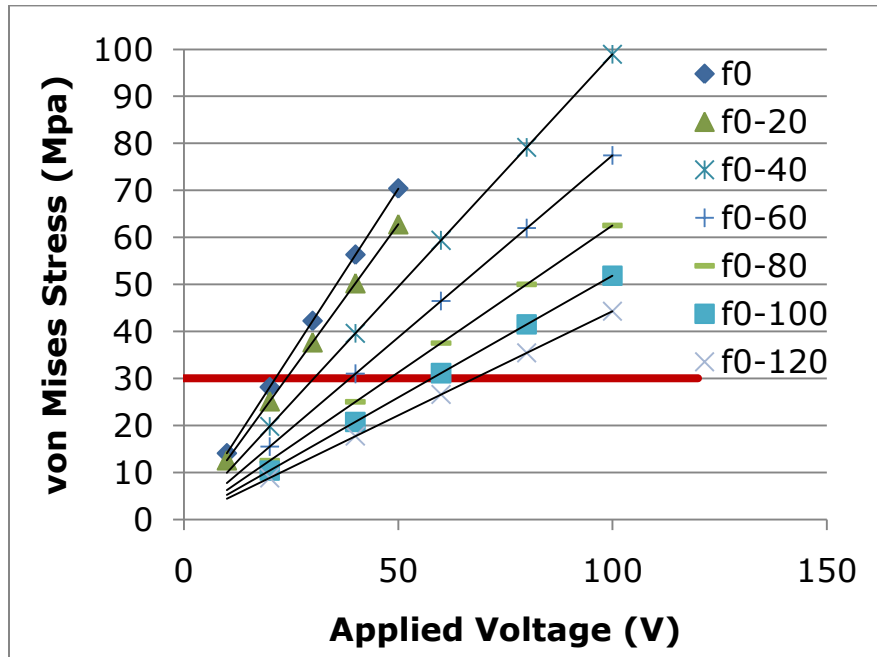


Figure 21: Peak output voltage that is produced with an applied voltage, V , over a range of frequencies extending from resonance, f_0 .

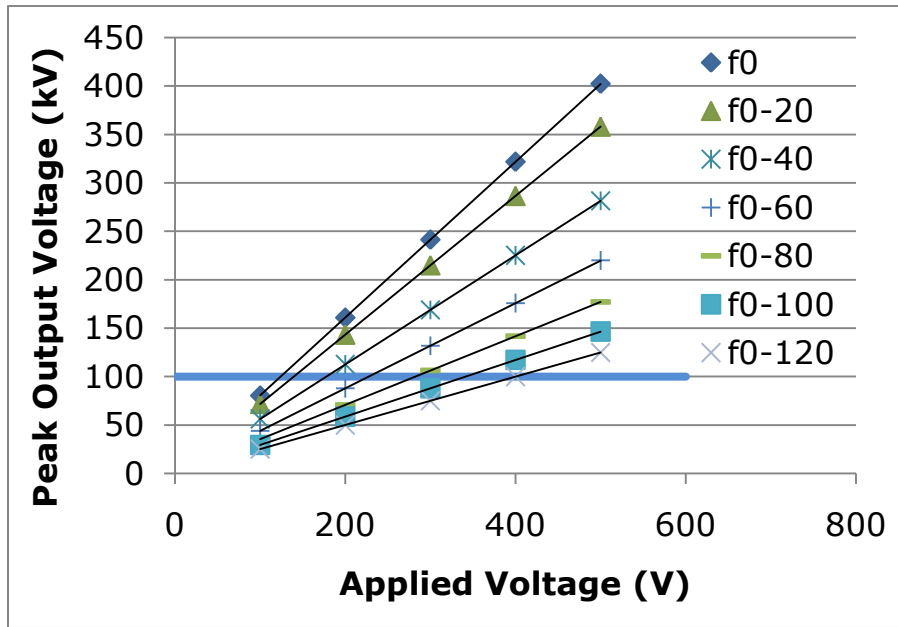


Figure 22: Peak von Mises stress that is produced with an applied voltage, V , over a range of frequencies extending from resonance, f_0 .

With this information, the applied voltage that resulted in both 100 kV and 30 MPa for each frequency were compared. These threshold values are shown together in the same parameter space in Figure 23. The comparison demonstrates that the applied voltages necessary for 100 kV production will result in fracturing the PT at all frequencies.

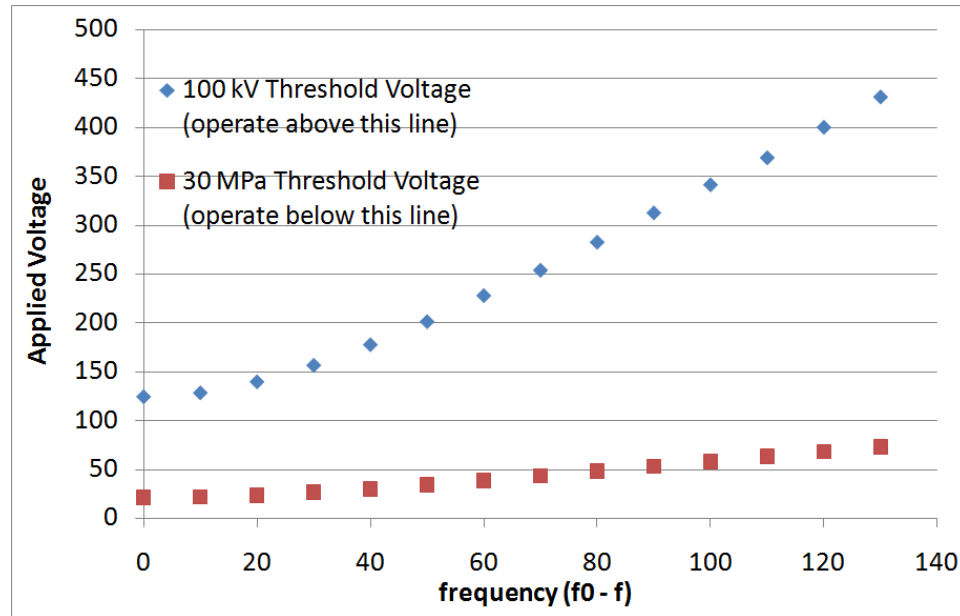


Figure 23: The threshold applied voltage for producing greater than 100 kV and less than 30 MPa over a range of frequencies extending from resonance, f_0 .

Even Stress Profile

The threshold plot shown in Figure 23 is specific to this PT design. Because the PT that was investigated is a first version design, there are many ways to try to improve its performance. Several redesigns were examined to increase the output voltage available from the PT while avoiding the stress that would break the PT. For this design process the peak allowable stress was defined as 30 MPa.

The techniques that were investigated involve spreading the highest stresses of the operating PT over the entire volume of the transformer material. This can be accomplished with very simple geometry changes. Simulations were performed to evaluate several proposed solutions to

increase output voltage for a given stress. The above analysis was repeated for the redesigned PTs. The redesigns included:

- PT Length
- Bipolar Output Geometry
- PT Cross Sectional Area
- End Mass Loading
- Combined

PT Length

The first redesign was to increase the length of the PT. The transformer ratio for this type of PT depends on the length of the device, so it would make sense if a longer PT can produce a similar output voltage with reduced stress.

The analysis was performed with a PT lengths ranging from 63 to 91 mm. Figure 24 shows the output voltage achievable at a stress level below 30 MPa. Two conclusions were made. First, the peak output voltage at a given stress did not depend highly on the driving frequency. As the driving frequency moves away from resonance, both stress and output voltage were reduced proportionately. Second, the output voltage can be increased by changing the geometry of the PT. As the PT length is increased, the output voltage at peak stress was increased.

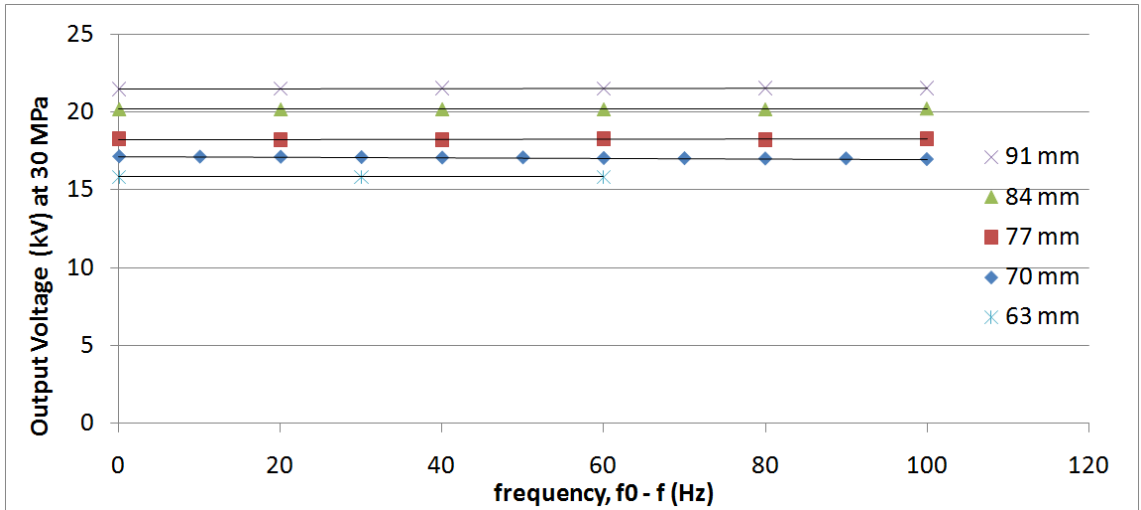


Figure 24: The predicted output voltage available from a PT of a specific length. This is determined as the simulated output voltage with a stress of less than 30 MPa.

The voltages curves from Figure 24 were used to predict the output voltage of a longer PT. A 240 mm PT was simulated with an expected output voltage of 50 kV at 30 MPa. The simulation demonstrated that the output voltage was actually closer to 55 kV for this geometry. This is shown in Figure 25. Based on the PT design that has been assumed up to now, the length of a PT to achieve 100 kV was predicted to be very long. For 100 kV, the length would be 450 mm according to the plot showing voltage at 30 MPa.

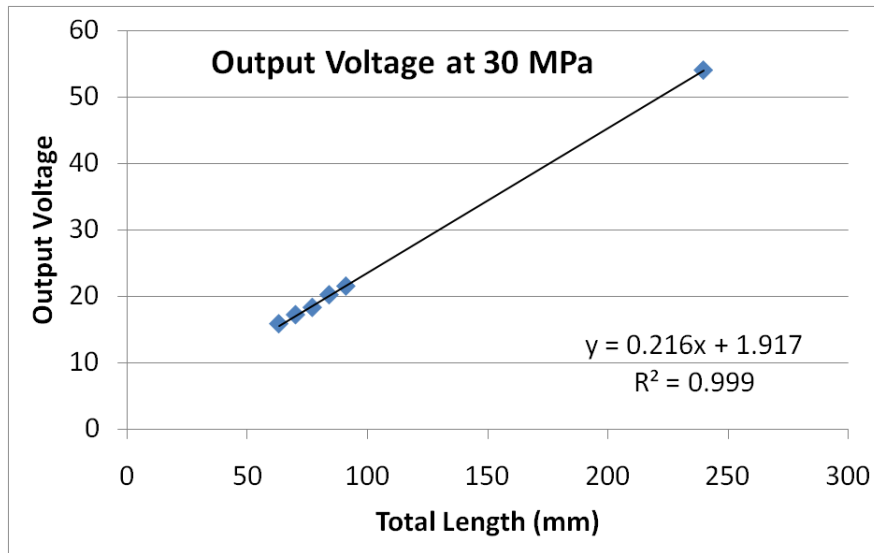


Figure 25: The peak output voltage for a length extensional PT is scalable according to the device length. These displayed voltages adhere to the 30 MPa requirement.

Bipolar Signal, PT squeezed from middle

By squeezing from the middle of the PT instead of at one end, a high voltage is developed at each end of the PT (plus and minus V_{out}). Under this geometry one PT end would generate ions and the other would be attached to the target material. This geometry divides the stress into two regions on either half of the input electrode. An example of this type of geometry is shown in Figure 26 and Figure 27. The material is driven by electrodes above and below the green colored section. For the example shown the peak output voltage at 30 MPa was increased from around 17 kV to about 23 kV for a 70mm PT.

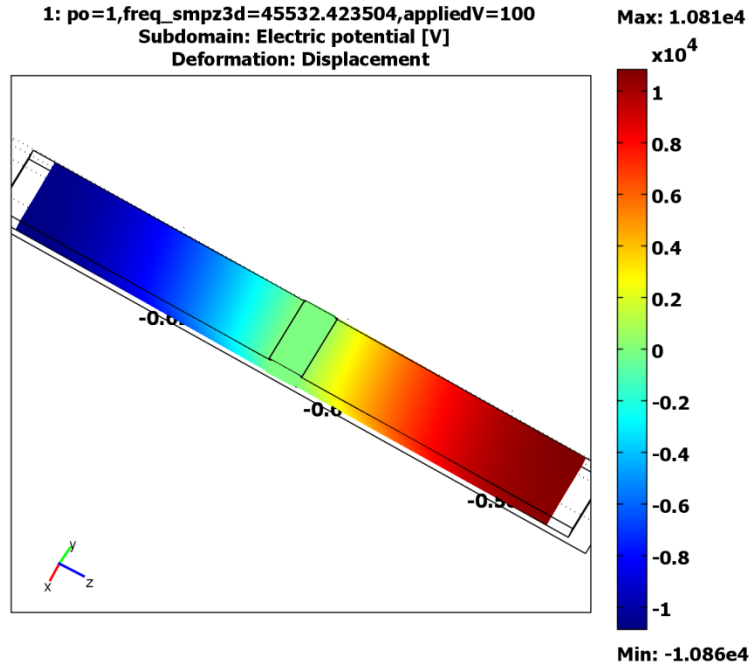


Figure 26: Output electric potential for a bar shaped PT while squeezing through the middle of the device.

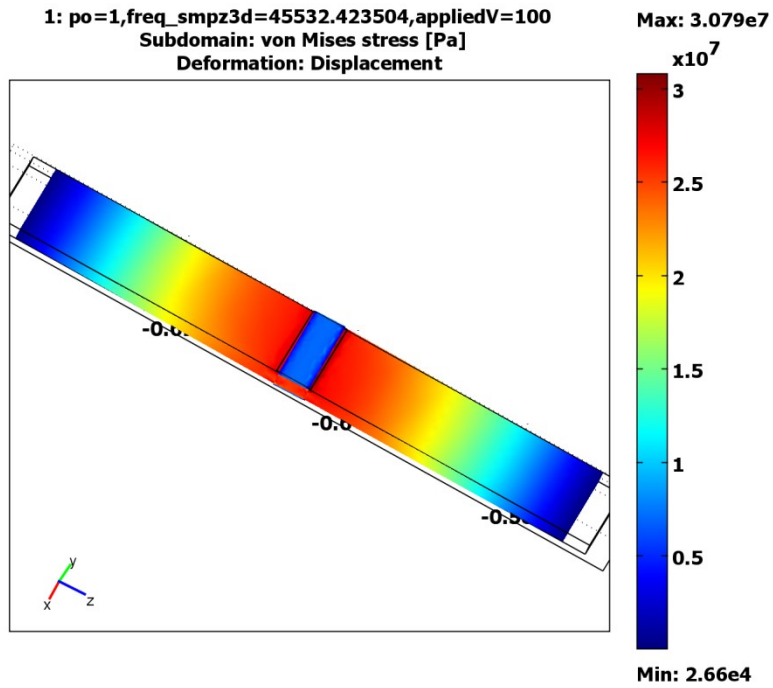


Figure 27: Von Mises stress profile in the PT at a peak stress of 30 MPa. This arrangement provided 22 kV

Trapezoid shaped surface

As seen in the original PT design, voltage is developed quickly away from the center of the PT. This is what creates the high stress near the electrodes. By shaping the cross section of the PT, the displacement and thus voltage and stress can be more evenly distributed along the length of the PT. The simulation shown in Figure 28 and Figure 29 demonstrated that by tapering the shape from 18 cm to 6 cm at the PT end, the output voltage available at 30 MPa is increased to 29 kV for a 70 mm PT and was 54 kV for a 140 mm PT.

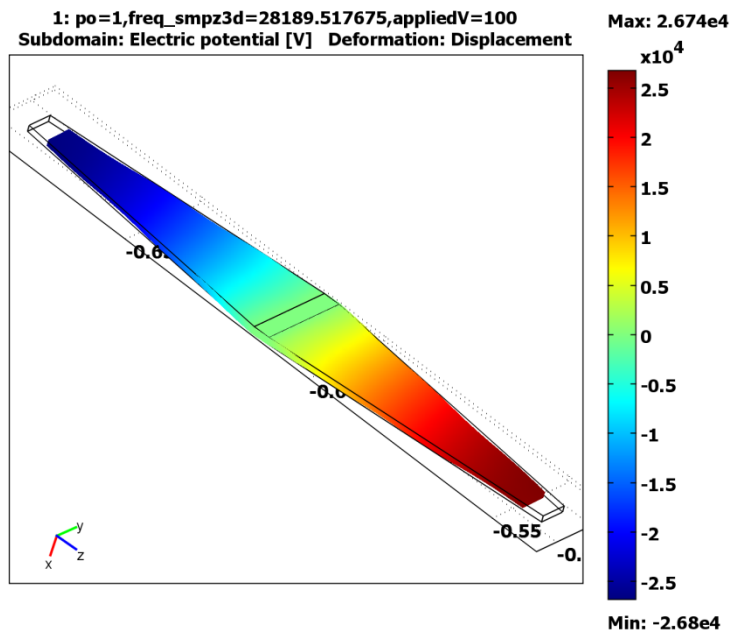


Figure 28: Output electric potential for a trapezoid shaped PT at 30 MPa.

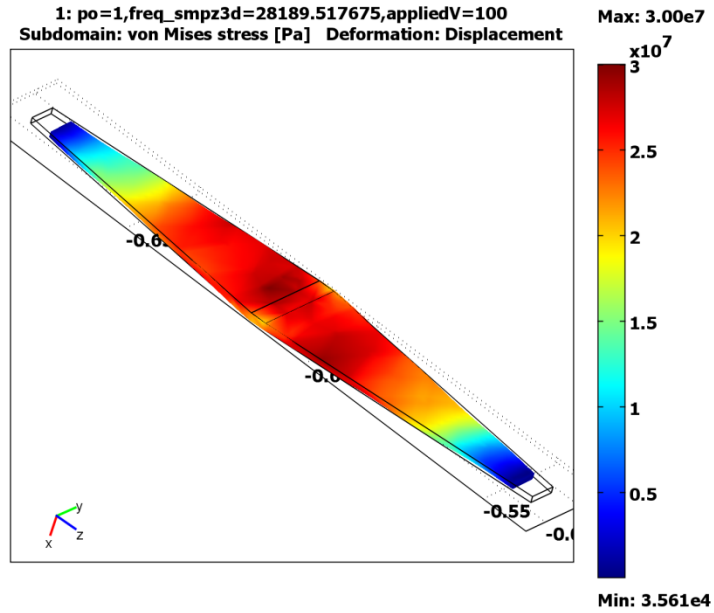


Figure 29: The stress of a trapezoid shaped cross section is more evenly distributed along the length of the PT leading to higher voltages.

Wedge shaped edge

A similar technique can be used on the PT y-axis geometry. Simulations showed that tapering the thickness of the PT will encourage the stress to shift more toward the end of the PT and increase the output voltage. In the simulation shown in Figure 28 and Figure 29, the thickness of the middle section was 3mm and the ends were 1.5mm. The output voltage at 30 MPa was 54 kV for a 140 mm PT which is greater than the PT with no tapered edges.

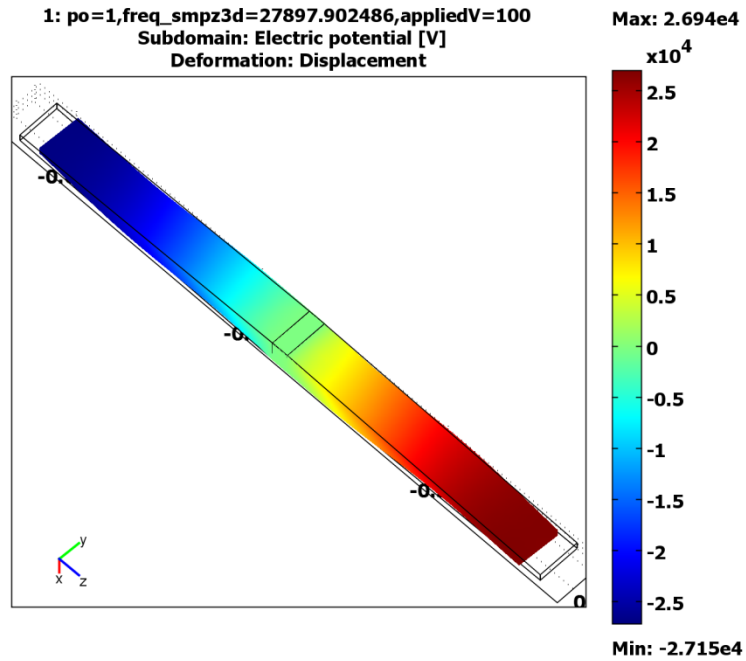


Figure 30: Electric potential on the surface of a wedge shaped PT at 31 MPa.

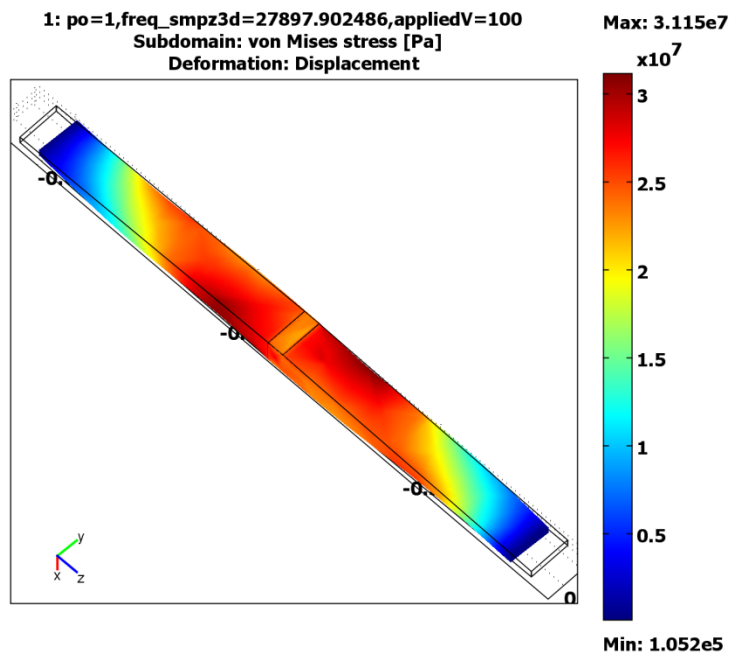


Figure 31: Von Mises stress profile for a wedge shaped PT at 31 MPa.

Mass loading

By placing mass at the ends of the PT, the end section of the trapezoid shaped PT was encouraged to undergo more displacement than the thicker section. This further distributed the total stress more evenly across the PT. Simulations showed that a 1mm piece of steel density material attached to the end of the PT increased the output voltage at 30 MPa by 20% above the output voltage of the tapered PT without mass added. This trend increased as the amount of mass was increased. The mass loading is very realizable with silver paint or epoxy used to attach wires or electrodes to the PT surface.

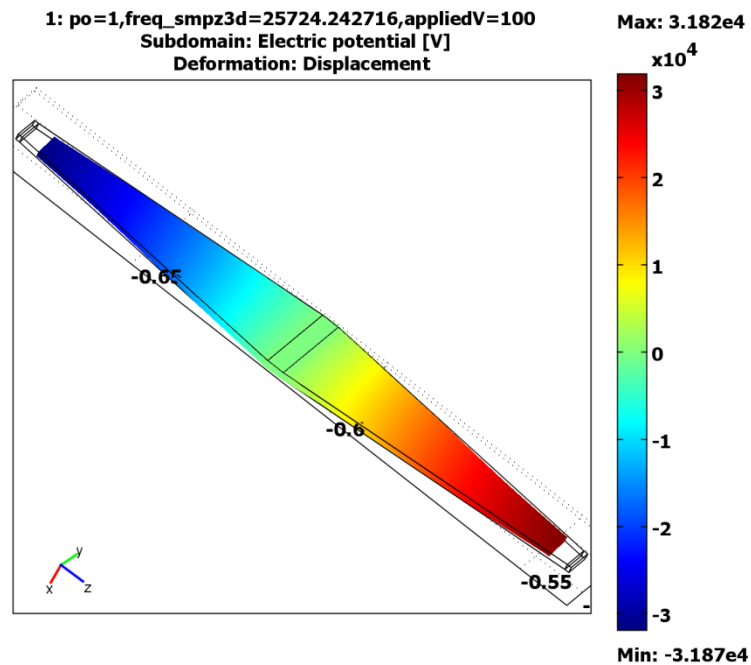


Figure 32: Electric potential for a mass loaded PT with tapered edges at 31 MPa.

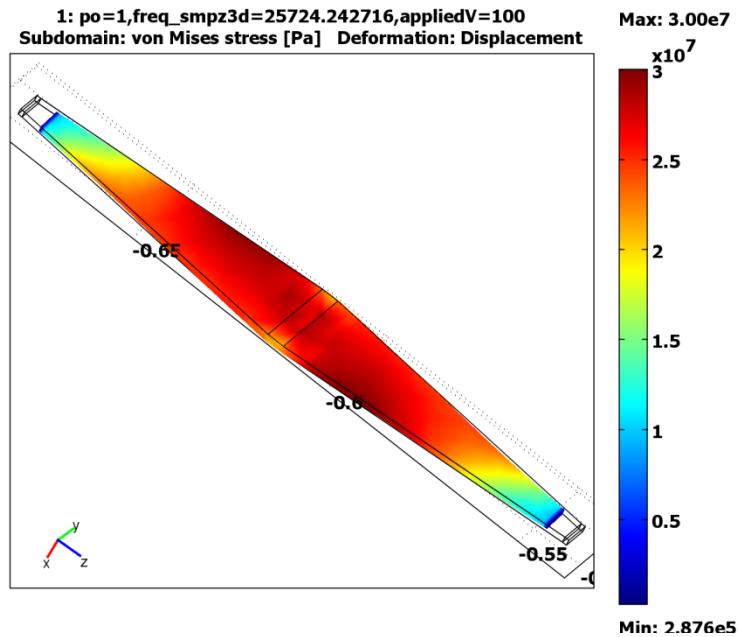


Figure 33: The von Mises stress profile of a mass loaded PT with tapered edges. The stress is much more evenly distributed along the PT.

Longer length PT

The length of the PT has a large effect on the peak output voltage at 30 MPa. By increasing the PT length the stress is pushed away from the PT center and is spread over a larger area. Using the techniques listed in this section, a 150mm PT was simulated and provided 99 kV at 30 MPa as shown in Figure 34 and Figure 35. The PT that was simulated had a 20mm to 6mm tapered edge contributing to its trapezoid shape. It had a 6mm to 1.5mm tapered edge contributing to its wedge shape. It had 2mm masses added to each end of the PT. The length of the PT was 150mm. Prior to PT geometry redesign, the estimated peak voltage for a 150mm PT was 34.5 kV.

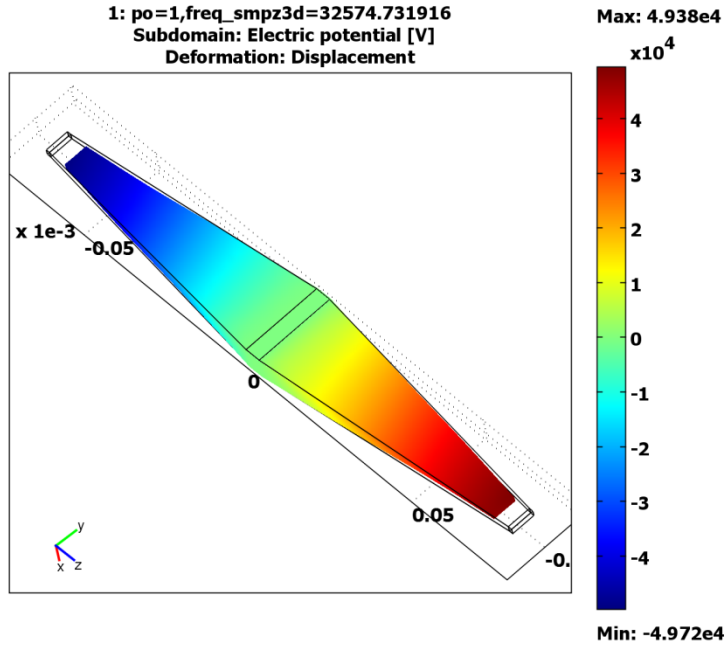


Figure 34: Electric potential for a 150mm PT at 30 MPa.

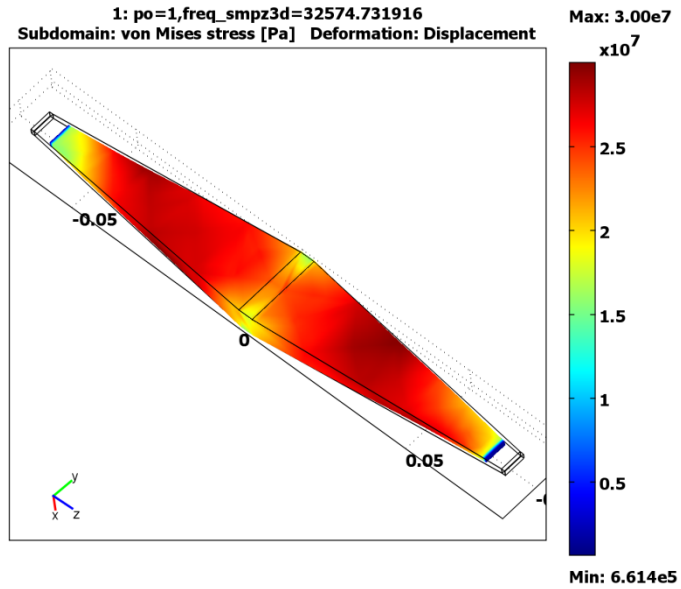


Figure 35: Von Mises stress profile for a 150mm PT at 30 MPa peak. The stress is much more evenly distributed than shown in Figure 20.

Finite Element Simulation Summary

The simulations that were performed provided much insight on the operation of the PT. The simulations indicated how best to hold and electrically drive the PT. They also demonstrated many trends that could be expected from experimental operation of the PT. These trends are summarized below.

- An increased device length reduced the resonant frequency according to the acoustic velocity.
- The device operated with a gain effect; increased input voltage will increase the output voltage.
- It was noted that the geometry of the electrodes determined how the PT performed.
- The length of both input and output electrodes affected the output voltage and electric field on the device. However, in a real device, reducing the input electrode length from the null point will prevent the use of the null point for advantages such as an ideal location to mount wires.
- Increasing electrode thickness restricts the motion of the device decreasing displacement.
- It was noted that the inclusion of real parameters such as mass and a loss factor also affected the performance of the PT.
- The inclusion of loss in the simulation greatly reduced the simulated peak voltage of the device.

- Additional mass (e.g. wire) will affect both the resonant frequency and decrease the gain of the device.

In addition to these trends, the FE simulations helped to reveal a number of potential issues that need to be addressed in the event of PT underperformance. These issues include:

- Location and Magnitude of Electric Field
- Peak Output Voltage at 30 MPa
- Profile of PT Stress

3. Experiment Setup

Atmospheric Test Stand

The first step in making a high voltage PT was to develop an experiment setup and protocol. Aluminum electrodes were attached to a LiNbO_3 crystal by aluminum sputtering. The electrode thickness was $0.5 \pm 0.1 \mu\text{m}$ thick. The direction of polarization with respect to the electrodes is shown in the experiment diagram in Figure 36.

As a minimum precaution to avoid high electric field enhancement, all electrodes were applied to the PT with rounded corners after January, 2009. A high resolution photo-resist pattern was created to make the rounded corners. A sheet with all of the photo-resist patterns used is included in the Appendix.

For atmospheric tests, the following test circuit was constructed. Current and voltage were measured at the input of the crystal with a Pearson 2877 current transformer, and a Tektronix P2100, 100:1, 16 pF, 10 M Ω voltage monitor. The output voltage was measured with a Tektronix P6015A, 1000:1, 3pF, 100M Ω voltage monitor. Later, the output voltage was measured with a variable impedance capacitive probe over a range of 3 to 15 M Ω which is described later in this section.

The input voltage was generated by an Agilent 33220A waveform generator. The voltage was applied in bursts of approximately 1000 cycles with control over the applied frequency and voltage amplitude. The signal was amplified with an AR KAA1020 25 Watt RF amplifier. The amplifier had a 50 Ω output impedance which was matched to the higher impedance of the crystal with an impedance matching transformer.

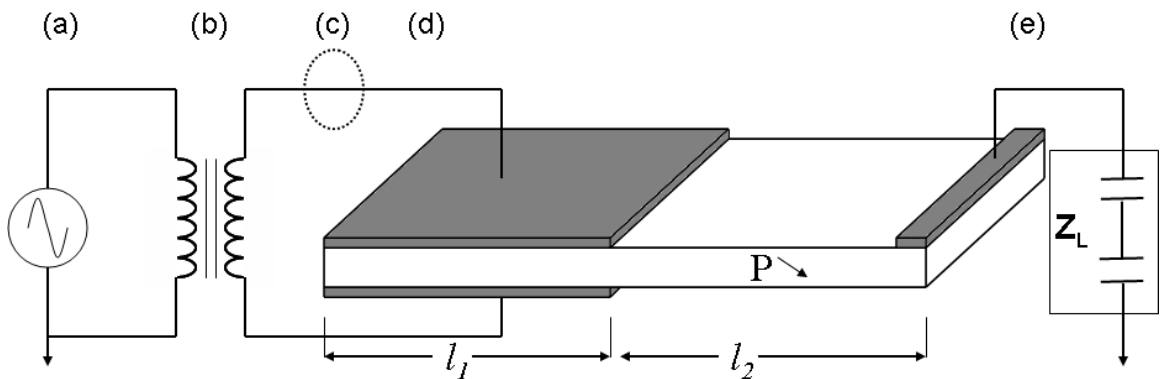


Figure 36: Diagram of setup with electroded crystal. The input and output dimensions are labeled l_1 and l_2 respectively. (a) Signal generator, (b) Impedance matching transformer, (c) Current transformer, (d) Input voltage Monitor, (e) Variable impedance capacitive probe.

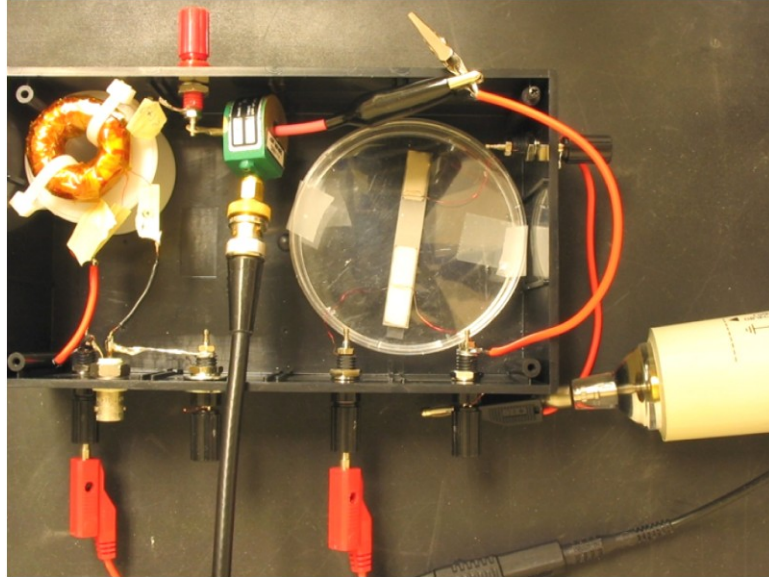


Figure 37: Picture of atmospheric test stand

Once the input impedance of the PT was initially measured, the impedance matching transformer shown in Figure 36 was constructed. The transformer was composed of a wound coil as shown in Figure 38. Because the impedance of the PT changes with frequency, a specific value had to be determined to which the source was matched. The lowest input impedance of the PT was used as the matching impedance because it was the frequency at which the highest theoretical gain could be reached and at which the most power would be transmitted to the PT.

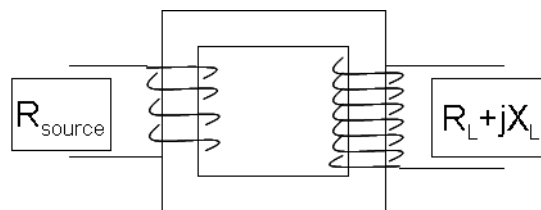


Figure 38: Impedance Matching Transformer

For the PT, the minimum input impedance was measured to be greater than the source impedance. This benefited the impedance matching design by allowing a greater number of turns to be applied to the secondary as shown in Equation 21. Therefore the matching transformer was also used to step up the applied voltage from the signal generator. In one experiment the minimum input impedance was measured to be near 1 k Ω . The turn ratio was set at 5:1 for the matching transformer to match 1 k Ω to 50 Ω .

$$\frac{N_1}{N_2} = \sqrt{\frac{Z_L}{Z_S}}$$

Equation 21

One drawback of the impedance matching transformer was that it was very difficult to change the number of windings once the transformer was built. This limited the versatility of the transformer when testing multiple PTs. After several tests it became apparent that the input impedance could vary significantly between several PTs. A new impedance matching transformer would have to be designed and built for each PT that was tested. To avoid this time consuming step the wound coil was abandoned in favor of a LL impedance matching network as shown in Figure 39. The LL network was favorable because components could quickly be exchanged in order to match a new PT. Table 2 shows the values for the LL matching network used to replace the impedance matching transformer. These values were found by an iterative curve fitting method in which the equivalent circuit for the PT

was applied to the output of the LL network. The entire circuit was then matched to the source by changing the LL network parameters.

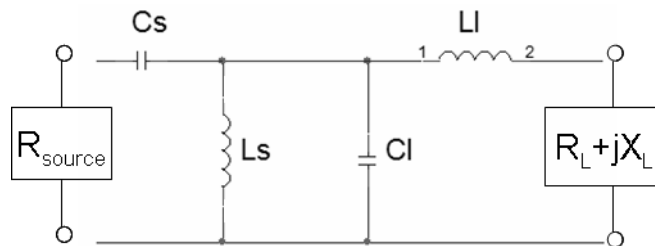


Figure 39: LL Impedance Matching Network

Table 2: Parameters for LL impedance matching network. Parameters were found by using an iterative curve fitting technique.

C_s (pF)	L_s (μ H)	C_1 (nF)	L_1 (μ H)
45.9	165	112	397

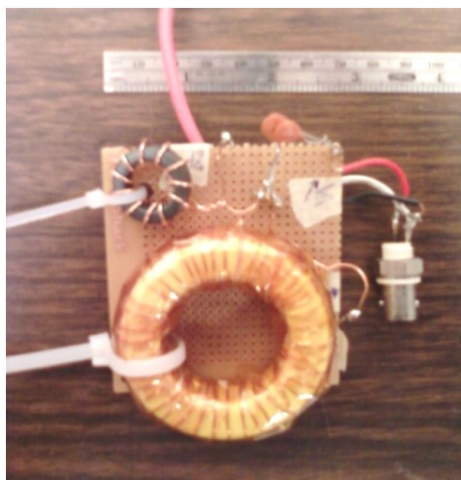


Figure 40: Picture of LL network

For early tests the output voltage was measured with a Tektronix 100 M Ω high voltage probe connected directly to the output electrode of the PT. The probe consisted of a 100 M Ω resistor in parallel with a 93 pF capacitor as shown in Figure 42 (b). For a 45 kHz signal, the capacitance reduced the magnitude of the diagnostic impedance from 100 M Ω to 38 k Ω . For many PTs, low diagnostic impedances can reduce the measurable gain. Figure 41 shows how diagnostic equipment can contribute to a reduction of load impedance and decrease the expected gain of a PT.

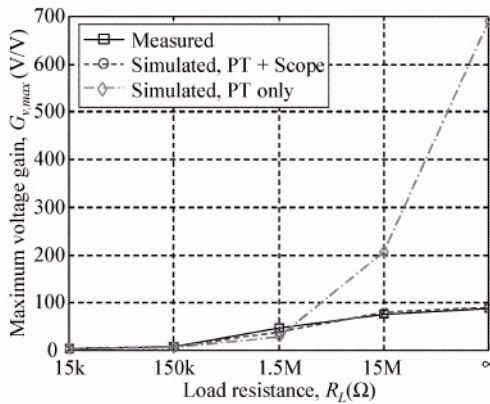


Figure 41: Because of its high output impedance, the PT gain can be affected by low diagnostic impedance [17].

To boost the load impedance, the diagnostic impedance had to be increased. A variable capacitance was introduced to the circuit in series with

the voltage monitor. The variable capacitance was composed of two plates with a separation distance, d , that could be varied over a range of 30 to 130 mm. The goal was to create a capacitance that on the order of 10^{-15} Farads resulting in an impedance on the order of $100 \text{ M}\Omega$ at 45 kHz.

The variable capacitor diagnostic shown in Figure 42 was then driven with a low output impedance circuit to reduce the possibility of a false calibration. The input voltage was compared to the voltage measured by the diagnostic. With a gap of 110 mm the attenuation of the diagnostic was increased to 1:370, and the variable capacitance was measured as 250×10^{-15} F. The impedance of the voltage probe was increased from $38 \text{ k}\Omega$ to as high as $15 \text{ M}\Omega$ as shown in Figure 43.

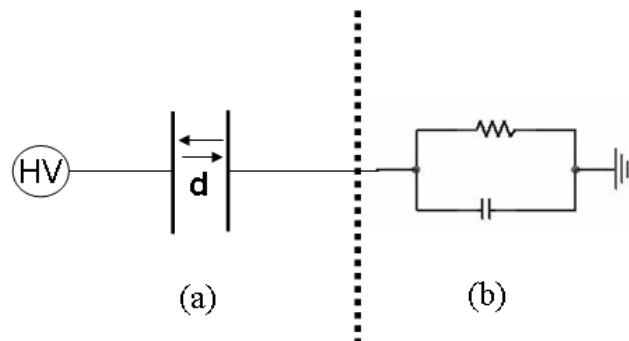


Figure 42: The diagnostic impedance (b) is increased by adding a series variable gap distance capacitor (a) with a very small capacitance.

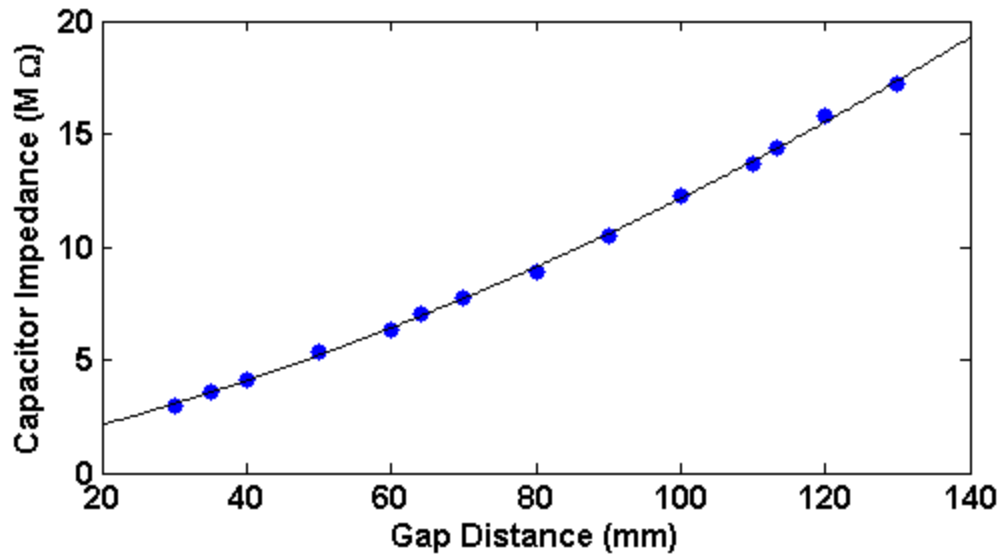


Figure 43: The attenuation of the high impedance diagnostic was increased by increasing the gap distance in the variable capacitor.

PT Holder

During initial tests, the PT was placed horizontally on a soft surface. While undergoing length extensional vibration, the surface of the PT was permitted to slide against the surface. To reduce the possibility of frictional loss, a holder was built to squeeze the LiNbO₃ crystal while lifting it away from any surface. To determine the best place to hold the crystal, the placement of the holder was swept along the PT length as shown in Figure 44. The PT gain was measured to determine the best place to hold the crystal. As shown in Figure 45, the gain was highest while the device was held near the low displacement null point. For all successive tests, the holder was positioned at the null point.

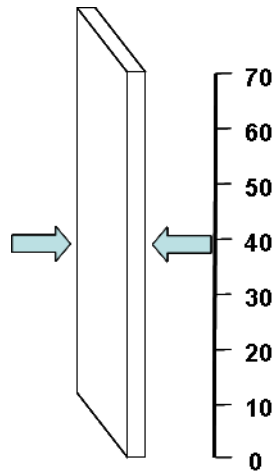


Figure 44: Location of PT holder

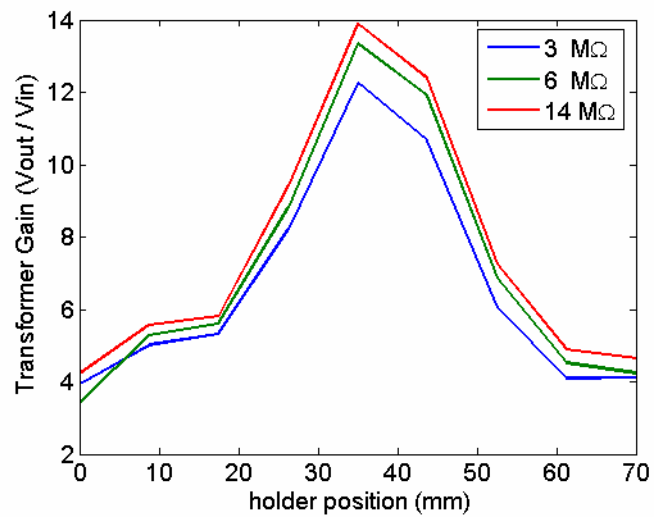


Figure 45: By holding the PT near its vibration null, its gain was increased.

Vacuum Test Stand

By increasing the voltage monitor impedance from 38 k Ω to 15 M Ω the output voltage was able to increase by a factor of 3 to 4. However both Nakamura and Chang showed in Figure 60 and Figure 41 that 15 M Ω is still low enough to decrease the gain of a PT by a factor of 4 to 5 from that of a 150 M Ω load. This indicates that the gain of the constructed PT may be higher than that measured thus far. From Figure 41 and Figure 43, it was apparent that an even higher impedance diagnostic would be needed to measure the true output voltage of the PT.

A method to increase the load impedance of the PT circuit and still measure the output voltage was developed. By attaching sharp tips to the output electrode of the PT, and placing it in a vacuum, electrons were emitted and accelerated by the PT. When the electrons were accelerated into a metal target at the energy levels mentioned, Bremsstrahlung radiation was produced in the x-ray range of the electromagnetic spectrum. By measuring the x-ray spectrum, electron energy was determined. The peak electron energy will corresponded to the tailing edge of the spectrum. An example setup for this observation is shown in Figure 46. This diagnostic method allowed for voltage measurements without directly attaching a probe to the output of the PT. With this method it was possible to detect a significantly higher PT gain.

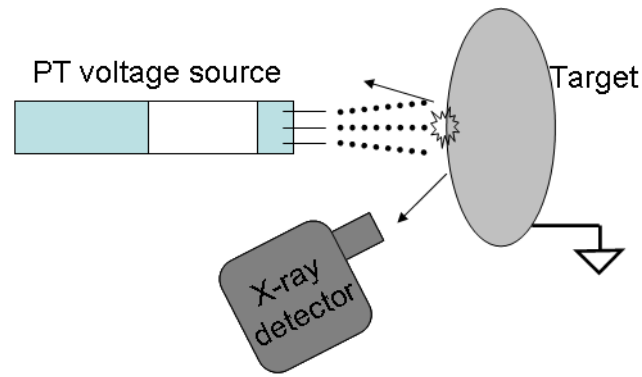


Figure 46: Bremstrahlung Radiation Measurement

Because the number of counts that the x-ray detector measures depends on the solid angle in which the detector views the target, the diagnostic was frequently sampled for long periods of time. During these sampling periods, the output surface of the PT would begin to charge positively as electrons were emitted. The following test setup was implemented in order to allow for a long sample period with time for PT neutralization.

The RF signal was generated with an Agilent 33220A waveform generator. The waveform power was boosted with an AR KAA1020 RF amplifier. The 50 Ω RF amplifier was matched to the input impedance of the PT with an impedance matching network.

The voltage signal was applied to the PT at the appropriate frequency over 1000 cycles per burst. The burst was applied 2 times per second. The signal was applied for 90 seconds and then the signal was turned off for 90 seconds. The off period allowed for electrons to travel back to the PT output

surface to neutralize it. This process created additional low energy x-rays which were also measured by the x-ray detector. The signal generating system is shown in Figure 47

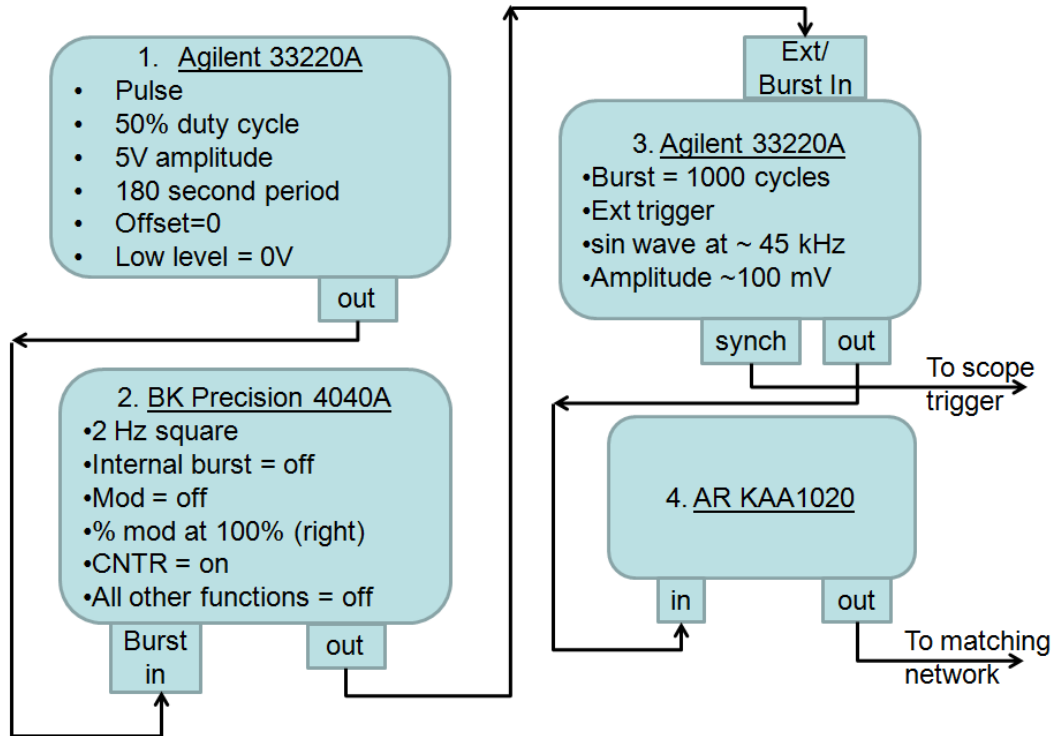


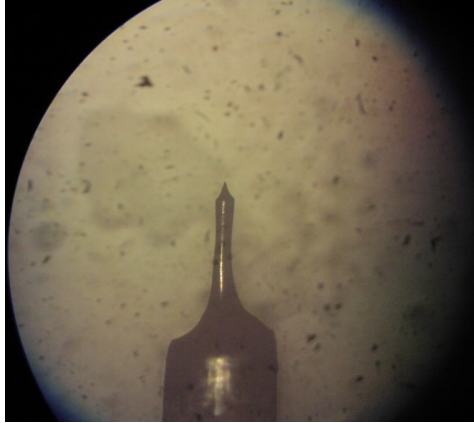
Figure 47: x-ray diagnostic trigger scheme

The waveform was fed into the vacuum chamber to a bracket that held the PT, the x-ray detector and the target material. The x-ray detector was a AmpTek XR 100-CR Si-PIN detector. The detector was controlled by a PX4 Digital Pulse Processor. The detector gain was set to 30 and the data were sampled over 4096 channels.

The base pressure in the vacuum chamber was 1×10^{-6} Torr. The vacuum was generated with a Helix CT-100 cryogenic pump. The pressure was measured with a Kurt Lesker Ion gauge controlled by a JC Controls IG 4500 Ion Gauge controller.

Two types of field emitting tips for electron emission were considered. The first was a tungsten etched single tip and the second was a platinum-iridium (Pt-Ir) cut single tip. The tungsten etched tip was fabricated by putting a DC signal on a tungsten wire whose tip was submerged in a container of 10% KOH solution. The tungsten wire was etched from its radius near the surface of the solution. Eventually the tip of the wire would stretch and fall into the KOH solution forming a sharp single structure on the remaining piece of wire [32]. Figure 48 (a) shows an image taken from a tungsten etched wire under a microscope.

This method of fabrication was found to be difficult for several reasons. Tungsten will begin to oxidize as soon as the tip is fabricated unless it is stored in an inert chemical. Formaldehyde was considered as a temporary storage solution to avoid oxidation, but the extra step of moving the tip resulted in a greater chance of damaging the tip by direct contact as shown in Figure 48 (b). To simplify the method of attaching field emitting structures to the PT, a different fabrication technique was sought.



(a)



(b)

Figure 48: A tungsten etched field emission tip (a). The tip was very fragile and difficult to move without bending (b).

The second method for fabricating emission structures was made by cutting Pt-Ir wire at an acute angle with wire cutting shears. While cutting the wire by hand, tension was applied to the wire so that it stretched as it was being cut in order to form a very sharp point. A picture of the Pt-Ir field emission structure is shown in Figure 49. This fabrication technique is common for creating the tips necessary for scanning tunneling microscopy (STM) [33].

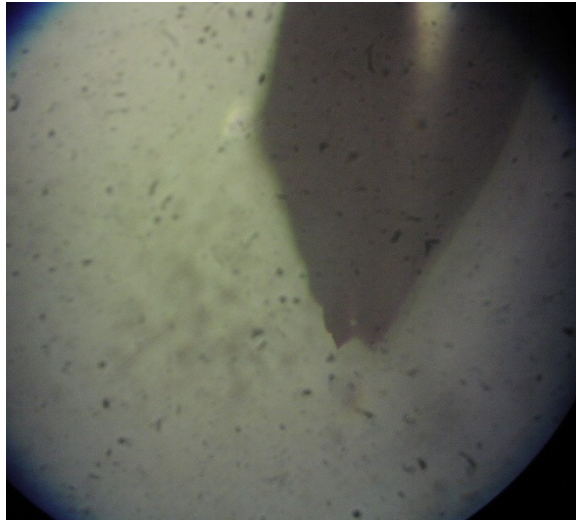


Figure 49: A Pt-Ir cut field emission tip.

The Pt-Ir field emission tip was preferred over the tungsten tip for several reasons. The Pt-Ir structure was very easy to fabricate by hand. Several tips could be made in less than 5 minutes. Each tungsten etched tip required significant setup time. The Pt-Ir wire was easy to directly transfer from fabrication to the LiNbO_3 surface. However, transferring the tungsten etched tip to the LiNbO_3 surface was much more difficult resulting in damaged structures as shown in Figure 48 (b). Finally, the tungsten etched structures were susceptible to damage from oxidation over long periods of time.

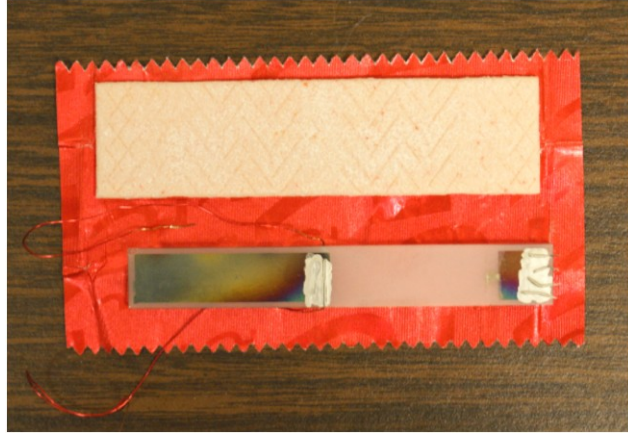


Figure 50: PT with aluminum electrodes, signal wires, and field emission structures attached. The PT is compared to a stick of gum (Juicyfruit) for scaling comparison.

Flashover Test Stand

To determine the conditions under which flashover will occur for a rotated Y-cut LiNbO_3 sample, a flashover test was performed. Electrodes were applied to a piece of LiNbO_3 with a gap of 4 mm as shown in Figure 51. A high voltage pulser capable of delivering 8 kV with a 1 μs pulse was connected to one electrode and the other electrode was grounded [34]. When high voltage was applied, flashover occurred across the gap. The recorded flashover voltage was 6.24 kV.

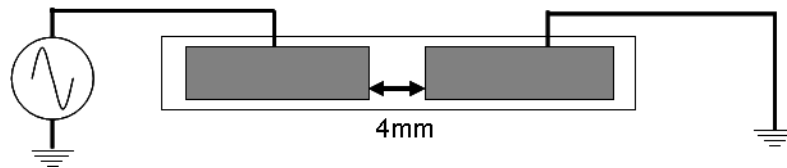


Figure 51: Pulsed flashover test setup. A 4 mm gap was formed between electrodes on a LiNbO_3 sample. Flashover occurred at 6.24 kV, 180 kV/cm near the electrode triple point.

4. Data and Analysis

Experiments were undertaken with the intention of creating and measuring high voltage and high gain from the PT. Measurements were made of many of the important characteristics of the transformer. Characteristics such as input impedance, mechanical loss, and an equivalent circuit were useful for predicting the behavior of the PT in models. Experiments were also made to minimize failure mechanisms of the PT such as flashover and fracture due to over stressing the PT. High voltage was measured using the variable capacitance probe and by measuring Bremsstrahlung emission energy. The experiments that are explained in this chapter, confirmed high voltage and provided a clearer understanding of the high gain PT operation.

Input Impedance

The input impedance was measured in atmosphere over a range of frequencies that included the half wavelength resonance. The result is shown in Figure 52. A drop in the measured input impedance occurred near the expected resonant frequency within about 2 kHz. Sweeping from low to high frequency, low impedance near the resonance is followed by a region of high impedance indicating anti-resonance. The close match between the measured and expected resonant frequencies indicates that the actual transformer is performing as predicted. The range of frequencies near the half wavelength mode will encompass the most interesting experimental results.

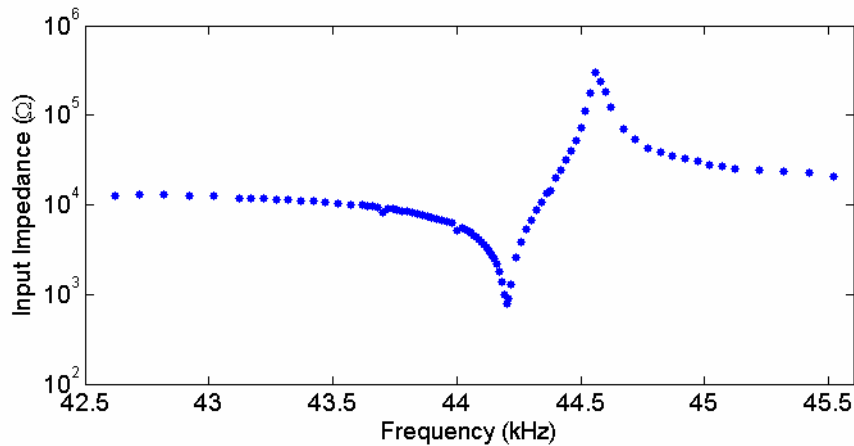


Figure 52: The measured input impedance of the PT close to the half wavelength frequency. Near resonance, the input impedance decreases.

Equivalent Circuit

An equivalent circuit is highly valuable in providing insight to the operation of real circuits. In this project, the equivalent circuit was used to design the impedance matching networks used in the driving circuit to increase the amount of power available to the PT. A properly designed impedance matching network is important for many conditions such as driving the PT slightly detuned from resonance. Detuning was used in order to prevent exceeding the mechanical stress limits of the device.

The circuit was also used to determine loss factors associated with the PT for finite element simulations. The correct loss factors are necessary to accurately determine the theoretical gain of the PT.

The generally accepted equivalent circuit for a vibrating piezoelectric circuit is called a Butterworth–van-Dyke (BVD) equivalent circuit. An example BVD equivalent circuit is shown in Figure 53. This circuit consists of C_0 and R_0 representing the PT input electrode capacitance and dielectric loss respectively. The mechanical vibration is represented by the components C_m , L_m , and R_m . The value of C_0 was measured directly from the PT. Once the resonant and anti-resonant frequencies were known, C_m was determined from C_0 by Equation 22. L_m was then determined with Equation 23.

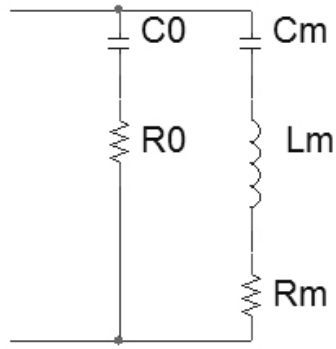


Figure 53: The BVD equivalent circuit for a piezoelectric transducer. The left side represents the capacitance formed from the input, and the right side accounts for the mechanical vibration [35].

$$C_m = \left(\frac{\omega_{AN}^2}{\omega_{RN}^2} - 1 \right) C_0$$

Equation 22

$$L_m C_m = \frac{1}{(\omega_{RN})^2}$$

Equation 23

Once those values were known, R_m and R_0 were determined by measuring the input impedance of the piezoelectric device and using an iterative curve fitting technique. The equivalent circuit impedance was compared to the impedance of the real device. By calculating the square of

the residual difference, R^2 , between the measured and calculated impedance the equivalent circuit was matched to the measured device.

The terms of the equivalent circuit were found by curve fitting. The automatic script used for curve fitting was implemented with Matlab code [36] and the script can be found in the appendix. Figure 54 shows a comparison between the measured input impedance and the input impedance from an equivalent circuit. A list of the best equivalent circuit values for one particular PT is shown in Table 6.

Table 3: Values for equivalent circuit determined by curve fitting to match input impedance.

C_0 (pF)	R_0 (Ω)	L_m (H)	C_m (pF)	R_m (Ω)
102.8	.01	3.81	3.35	2009.3

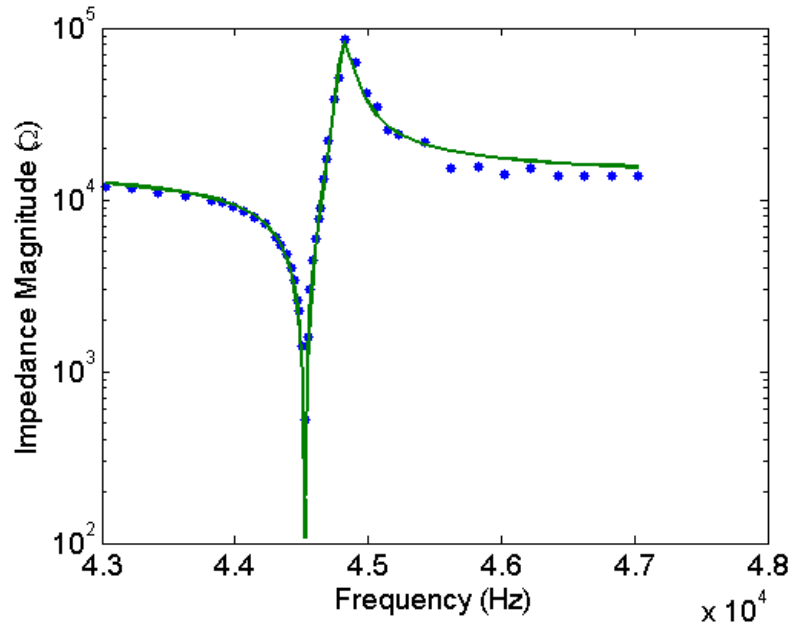


Figure 54: Measured input impedance (blue) and input impedance of an equivalent circuit (green) determined by curve fitting.

Mechanical Loss

The mechanical loss factor describes how much energy is lost per cycle as a proportion of stored energy in the PT. A high mechanical damping coefficient results in a high mechanical loss factor. Once R_m is known, the quality factor and thus the mechanical loss factor can be determined with Equation 24 and Equation 25. These values are used to introduce loss into finite element simulations to determine the real performance of a PT. For a typical PT, the mechanical loss factor was found to be 0.0018.

$$Q_m = \sqrt{\frac{L_m}{C_m}} \frac{1}{R_m}$$

Equation 24

$$\text{Mechanical Loss Factor} = [Q_m]^{-1}$$

Equation 25

As methods to reduce mechanical loss and increase the quality factor were implemented, the peak output voltage of the PT was increased. This result was in agreement with Equation 17. One early improvement was to improve how electrodes were applied to the PT surface. During initial experimentation, the electrodes were applied to the PT by applying a thin coat of silver paint directly to the PT surface. In order to create a thinner, and more even electrode surface, higher quality electrodes were applied with an aluminum sputtering system.

The quality factor of the PT with silver paint was compared to the PT with aluminum electrodes. With silver paint the equivalent circuit had a minimum mechanical resistance of 3.52 k Ω and a quality factor of 303. Once the aluminum electrodes were applied with a sputtering system, the quality factor of the PT rose to 531.

Flashover Prevention

During experimentation, the peak output voltage measured in the laboratory was increased to several kV. When the output voltage measured in atmosphere approached 2 kV and beyond, a pinging noise was frequently observed to correspond with the high voltage. Eventually the pinging noise was attributed to flashover occurring on the PT surface. Discharges were observed as flashes of light near the input electrode with branches extending along the length of the device toward the output electrode. Because the brightest point appeared near the input electrode of the PT, this area was considered to be the point at which the discharges originated. A list of these events is recorded in Table 4. Once flashover occurred, the output voltage generally did not greatly increase as the driving frequency approached resonance.

When a high voltage pulse is being produced, the voltage profile along the length of the PT can result in a large electric field on the PT surface. The high electric field can then lead to unwanted discharges forming [29, 20]. For the tested PT, flashover was observed on the surface of the PT when high voltage experiments are being conducted. The conditions leading to flashover were examined and several methods for eliminating flashover were tested.

Table 4: Summary of flashover events during high voltage tests

Date	Input Electrode Length (mm)	Output Electrode Length (mm)	Voltage (V)
2008/04/27	23	5	1890
2008/07/04	32	10	1993
2008/07/07	32	17.5	2071
2008/12/18	32.5	9	1850
2008/12/19	35	9	2900
2009/01/22	29.5	5	3137

A method for eliminating flashover was sought and two methods were investigated. The first involved carefully designing the input electrode so that the edge of the electrode corresponded to the region with the smallest electric field. This method was tested and found to be partially successful. As shown in Table 4, the peak output voltages were achieved with the PTs that had electrodes applied according to the lowest electric field profile shown in Figure 19.

The second method to improve the flashover voltage was to deposit a thin dielectric film over the entire device, or at least the region of the device at which the discharge occurs. Previous experimentation has shown that encapsulation can be used to prevent flashover in pulsed high voltage environments [37]. Encapsulation works by suppressing pre-breakdown field emission currents from a material [38]. For this reason, application of thin dielectric films at high voltage triple points can inhibit the growth of flashover.

This method was initially tested by depositing a thin layer of parylene on top of both LiNbO₃ and electrode encapsulating both. The same test setup was used as before with a 4 mm gap and 8 kV pulser. When subject to pulses the gap did not break down for approximately 60 pulses over 3 seconds. Eventually bulk breakdown occurred through the parylene and flashover occurred across the gap on every succeeding pulse.

Because thin film encapsulation with parylene was successful in preventing flashover during this experiment, the idea was expanded for flashover prevention on the high voltage PT. Parylene was chosen as the encapsulating material for several reasons. Parylene has a high pulsed bulk breakdown strength of 2.6 MV/cm [39]. It is inexpensive and readily available. Parylene is also easy to deposit as a thin film using vacuum evaporation with no substrate heating required. As a thin film it is transparent, so any discharges can be observed. After deposition it has low stress at room temperature. The thickness and range of parylene deposition is easily controlled and is highly uniform.

An experiment was performed to determine if thin film deposition can be used to inhibit flashover on a high voltage PT. A thin film of parylene was deposited with varying thickness and length on several high voltage PTs. Careful consideration was made to determine the best location for the deposited film to minimize its effect on the operation of the PT. The thin film was found to inhibit flashover.

One drawback to adding a dielectric layer was that it could introduce additional mechanical loss. However, with proper electrode design, it was possible to deposit parylene to a small region of the PT as shown by the dashed region in Figure 55. In that case the location of the encapsulating parylene would correspond to the region of least mechanical vibration. Depositing a thin dielectric film only in that region may both prevent flashes from occurring and contribute little additional mechanical loss.

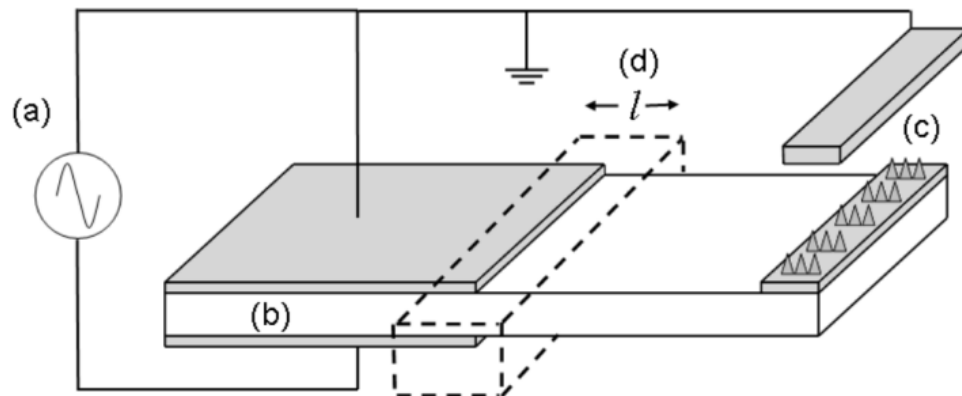


Figure 55: Parylene could be added to only a small region as demonstrated by the dashed box in order to minimize mechanical loss. The experiment diagram is shown; (a) RF source, (b) rotated Y-cut LiNbO₃, (c) field emission structures and target, (d) parylene deposition of length, L .

Five high voltage PTs were prepared for experimentation. Four of the samples received a thin film of Parylene type C which encapsulated the triple point region. The thin film extended 1 mm to the input side of the triple

point and extended a length L toward the output end of the PT. A control PT with no added parylene was also fabricated.

In order to determine the effect of encapsulation on the PT, two parylene lengths were chosen, 5 and 9 mm, at two different deposition thicknesses, 4.8 and 9.2 μm . The dashed region shown in Figure 55 shows the location of the parylene on the PT. This location corresponded to the region of least mechanical vibration of the PT.

Each PT was driven with a RF signal near the half wavelength resonant frequency, f_0 . For each PT the resonant frequency was near 44.5 kHz. The frequency was swept from below to above resonance. For each test, the input and output voltage was measured and the PT surface was monitored for evidence of flashover. For each PT, the output voltage increased as resonance was approached and then decreased away from resonance. The measured input and output voltage were used to calculate voltage gain. The gain under low voltage operation for each PT is displayed in Figure 56.

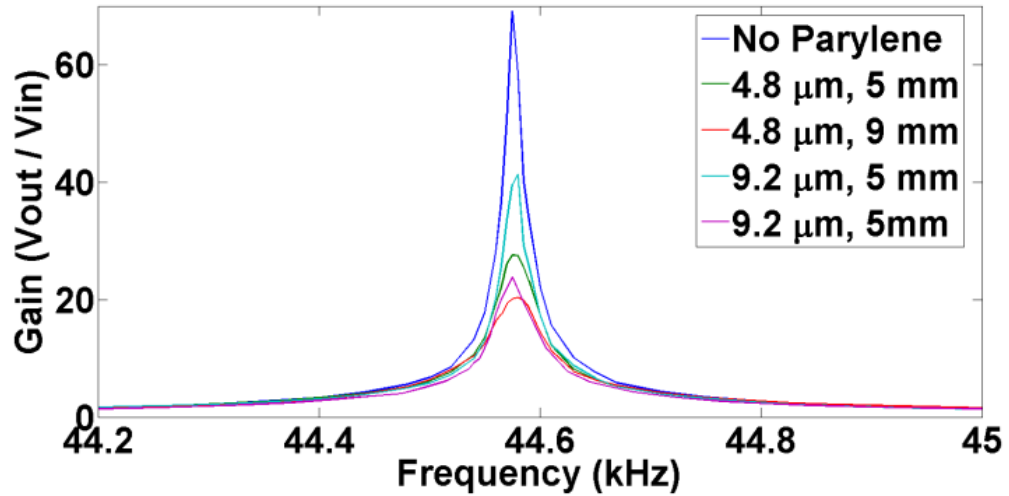


Figure 56: Gain at low voltage operation for all configurations centered on the average resonant frequency.

Under high voltage operation, the PT with no parylene began to exhibit flashover when the output voltage was increased to beyond 1470 V. None of the parylene coated PTs exhibited flashover throughout the entire frequency range. The peak voltage for each PT is recorded in Table 5. As shown, the peak voltage for a PT with a parylene encapsulated triple point exceeds that for the PT without parylene encapsulation. For high voltage tests, once flashover occurred the output voltage was not increased.

Table 5: High voltage PT summary

PT type	Peak voltage before flashover (V)	Mechanical Loss Factor
No Parylene	1470*	0.00188
4.8 μm , 5 mm	2400	0.003384
4.8 μm , 9 mm	2259	0.007144
9.2 μm , 5 mm	2675	0.002632
9.2 μm , 9 mm	2298	0.00564

**flashover occurred at this voltage with no parylene*

A way to evaluate the parylene's contribution to mechanical loss was developed. For this, the mechanical loss factor for each PT was calculated and compared. The input impedance of each PT was measured to determine its equivalent circuit. The equivalent circuit is shown in Figure 53 where C_0 and R_0 represent the capacitance formed on the input side of the PT and C_m , L_m , and R_m , represent the mechanical vibration of the PT under a specific wavelength mode. At the resonant frequency determined by C_m and L_m , the impedance of the PT is dominated by R_m .

The mechanical loss factor of the vibrating system, $[Q_m]^{-1}$, is found from the equivalent circuit by Equation 24 and scales with R_m . The mechanical loss factor, which represents mechanical damping of the vibrating crystal, is shown in Table 5. The mechanical loss for the high voltage PT was found to increase when parylene was added to prevent flashover.

As shown by the experimental gain curves in Figure 56, the gain produced by the PT was reduced by the parylene coating. It was discovered that by increasing the length of the parylene deposition, the PT gain was further reduced at a set frequency. This was also demonstrated by the loss factor that was determined for each parylene coating. Figure 57 shows the effect of the parylene length on the damping of the PT. As the length of the parylene coating was increased, the loss factor was increased. This led to the conclusion that the parylene contributed to the mechanical loss by restricting the motion of the LiNbO_3 .

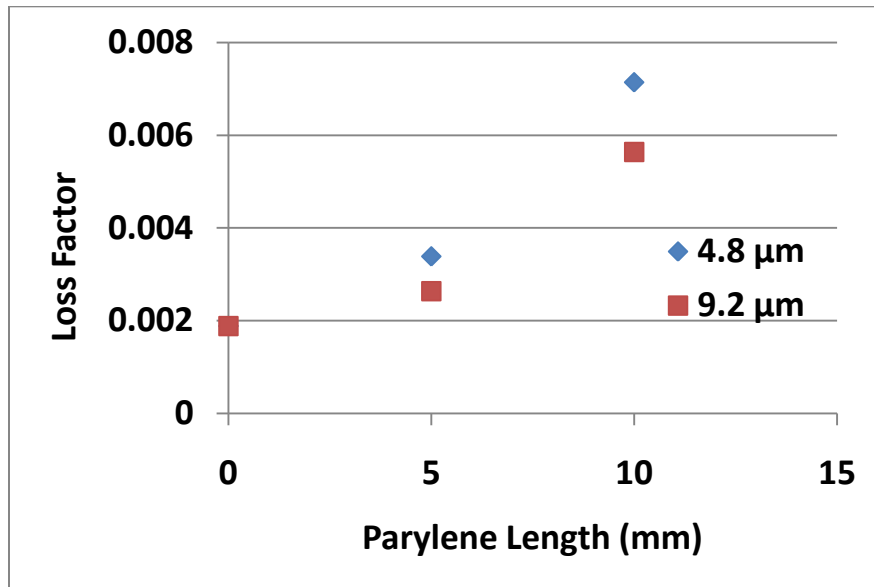


Figure 57: Loss factor vs. parylene length.

From Figure 57, it was also demonstrated that a thicker encapsulation did not lead to increased loss. In fact, for this experiment the mechanical

loss factor was greater for the 4.8 μm thick parylene than for the 9.2 μm thick parylene. One possible explanation for the difference stems from the use of two different parylene application cycles necessary for differing parylene thicknesses. It is possible that an inconsistency between the parylene deposition cycles caused the parylene to adhere slightly differently. Another possible explanation for the difference is that the thicker parylene contributed to a small amount of additional stability at the low vibration null point.

High Voltage Measurements

With the driving portion of the circuit in place the performance of the PT was tested. Initially the measured output voltage and gain was lower than expected. The input and output voltage of the transformer was measured over a range of 40 to 46 kHz. The transformer ratio was then calculated over that region. Using an input voltage of 35 V_{pp} , voltages slightly greater than 800 V_{pp} were measured demonstrating a voltage gain ≥ 20 . Figure 58 displays the output voltage of the transformer and Figure 59 displays the transformer voltage ratio near the first resonant frequency.

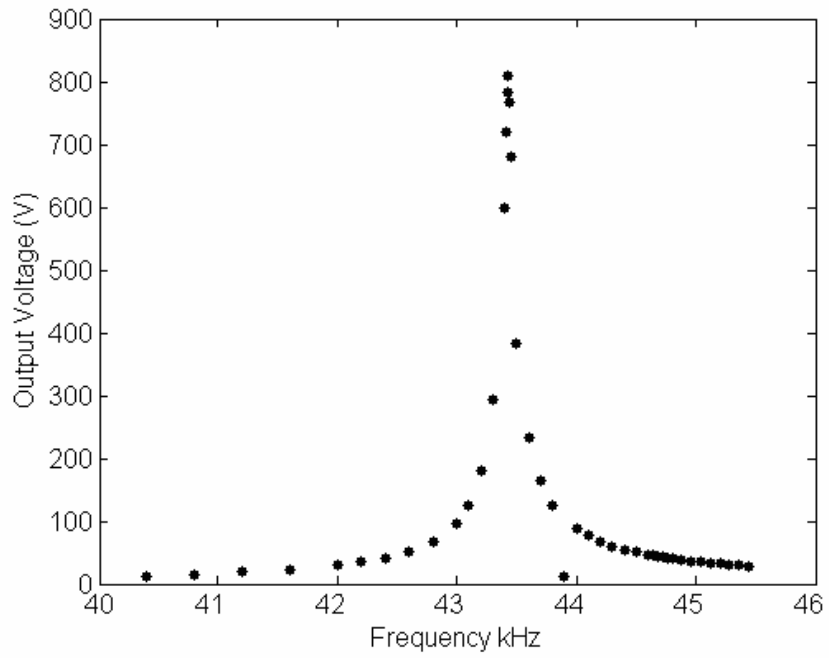


Figure 58: Initial Output Voltage

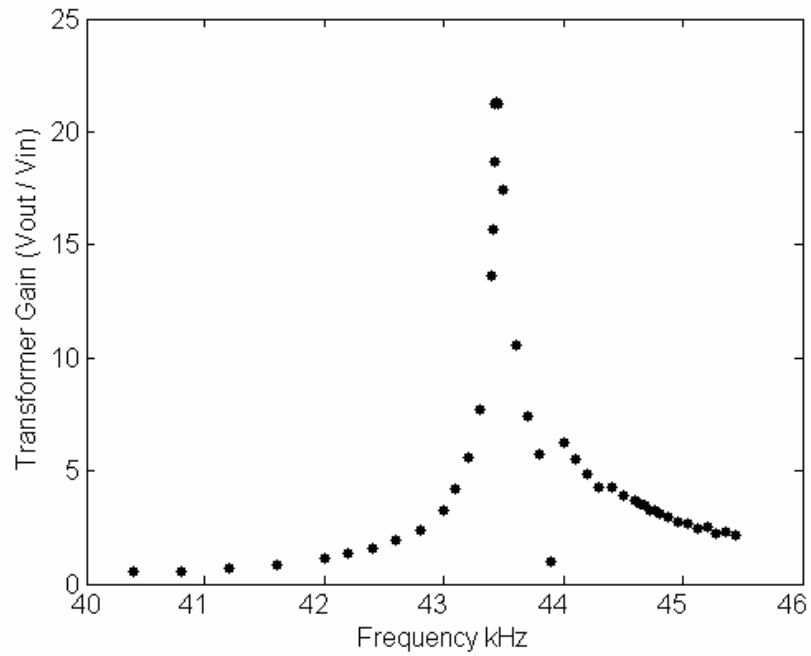


Figure 59: Initial Voltage Gain

Variable Capacitance Diagnostic

The output voltage was lower than expected so an explanation was sought. Previous work has shown that the load impedance of a PT circuit can have a large effect on the PT's gain [29]. Because the output impedance of PTs are very high, load impedances of less than 100 M Ω can begin to decrease the voltage for high voltage PT circuits. This is demonstrated in Figure 60 for a high voltage PT developed by Nakamura.

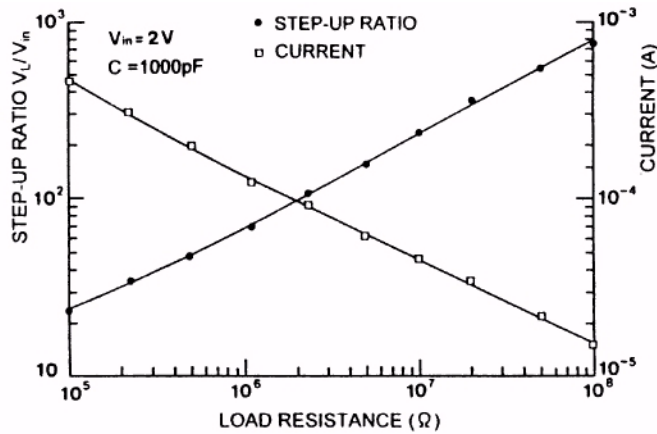


Figure 60: PT gain will be reduced by relatively low load impedance [29]

To more accurately measure the output voltage, the variable capacitance output voltage diagnostic that was described beginning on page 54 was used. The HV connection shown in Figure 42(a) was connected directly to the output end of the PT with a small section of transformer wire. The output voltage of the PT using the new diagnostic was increased from near 800 to above 2 kV as shown in Figure 61. The voltage gain was increased near 20 to above 70 as shown in Figure 62. While the output

voltage of the PT was increased, it was still lower than expected. Therefore the x-ray diagnostic was used to further avoid loading down the PT voltage.

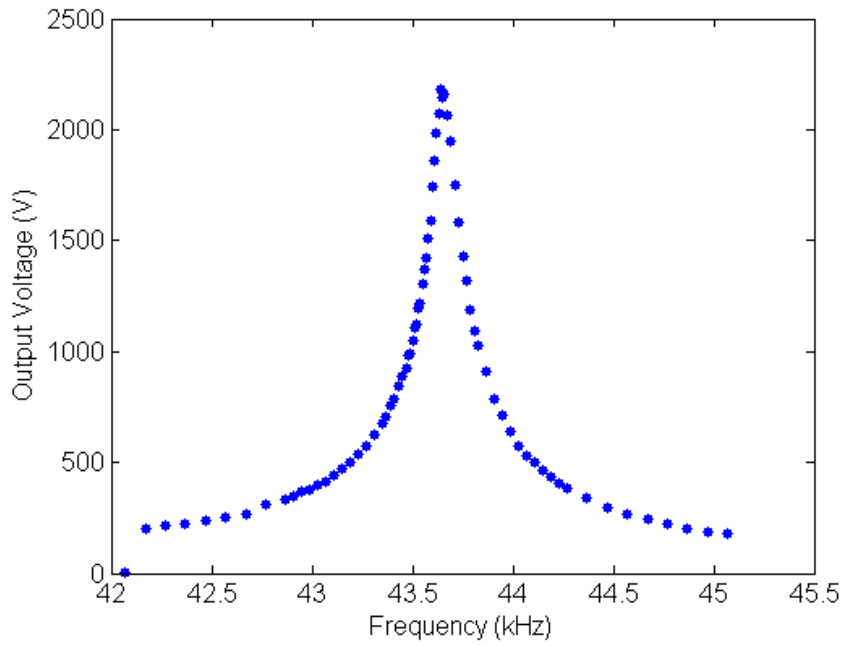


Figure 61: Increased Output Voltage

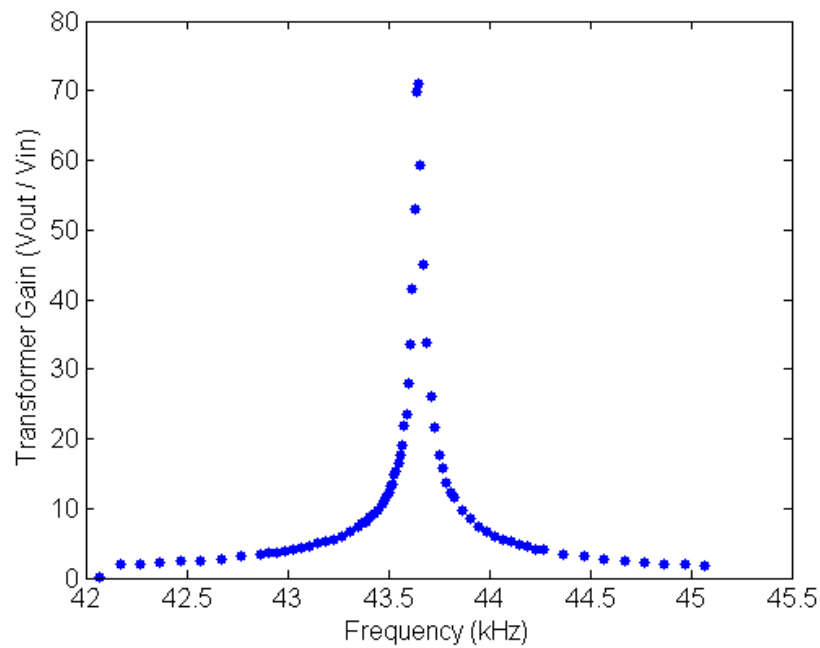


Figure 62: Increased Voltage Gain

X-ray High Voltage Measurements

The method of using x-ray energy to determine the accelerating potential of the piezoelectric transformer was utilized. The method was described in Chapter 3. Because x-ray measurements were being made above the factory calibration for the Si-PIN x-ray detector, special attention was paid to ensure that the measured spectra contained easily identifiable fluorescing lines from known materials [40]. Several targets were used during these tests including titanium, tungsten, and molybdenum and several fluorescent lines were identified.

During testing it became apparent that the x-rays were being measured after the electron emission was “turned off.” This was due to surface charging of the PT output electrode. As electrons were emitted, the output electrode became positively charged. When the PT was turned off and was no longer creating high voltage, electrons were accelerated back toward the output electrode. The blowback of electrons created additionally measured x-rays as they impacted the PT. The x-ray energy decayed in energy as the PT output electrode gradually neutralized.

Further scrutiny lead to the conclusion that under normal operation the PT will charge to a certain positive value due to electron emission. However, the surface charge will not hinder, but could actually aid in the production of energetic ions by providing an additional DC bias to the output electrode. Nevertheless, to reduce the amount of surface charging for electron emission

tests, the surface was allowed to self neutralize for 90 seconds after every 90 seconds of electron beam current.

For the first experiment, the driving frequency was held constant at 10 Hz from resonance. The input voltage was incrementally increased to the PT. As described on page 63, the PT was driven to high voltage 2 times every second for a period of 90 seconds out of every 180 seconds. The emitted x-rays were sampled over a period of 30 minutes for each input voltage.

Figure 63 shows the resulting spectrum from electron emission with a tungsten target. The spectrum contains both Bremsstrahlung and fluorescence lines. Two specific peaks were observed. The higher energy peak was from the $K(\alpha_1, \beta_1)$ shells of the titanium target which are at approximately 4.5 keV. The lower energy peak was from the $L(\alpha_1, \beta_1)$ shells of the niobium in the PT which have energies near 2.2 keV.

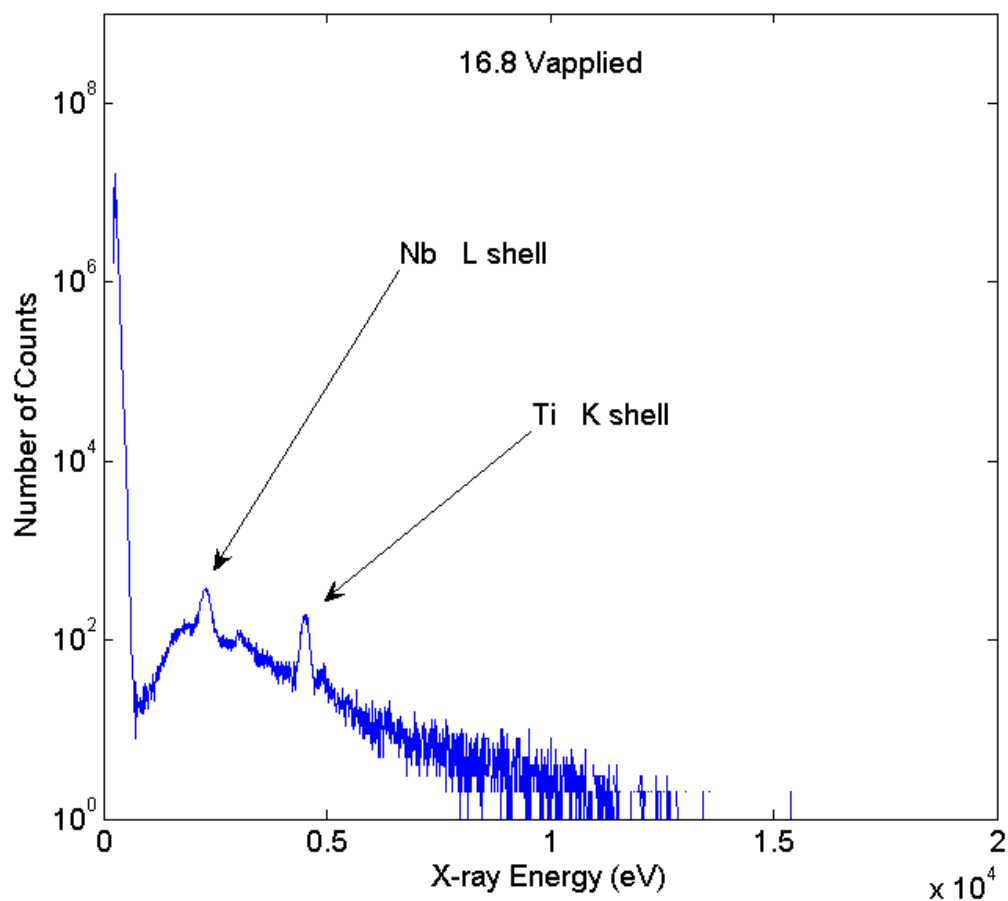


Figure 63: Bremsstrahlung and Fluorescence at highest energy for titanium

To directly view the effect of output voltage on electron energy, the PT input voltage was slowly increased as x-rays were measured. Figure 64 shows the x-ray energy in number of counts as the PT voltage was increased to several specific values. The electron emission structures were Pt-Ir wires attached to the PT output electrode. The electrons were accelerated into a titanium target. Below a certain threshold no electron current was observed and only background x-ray emission was measured.

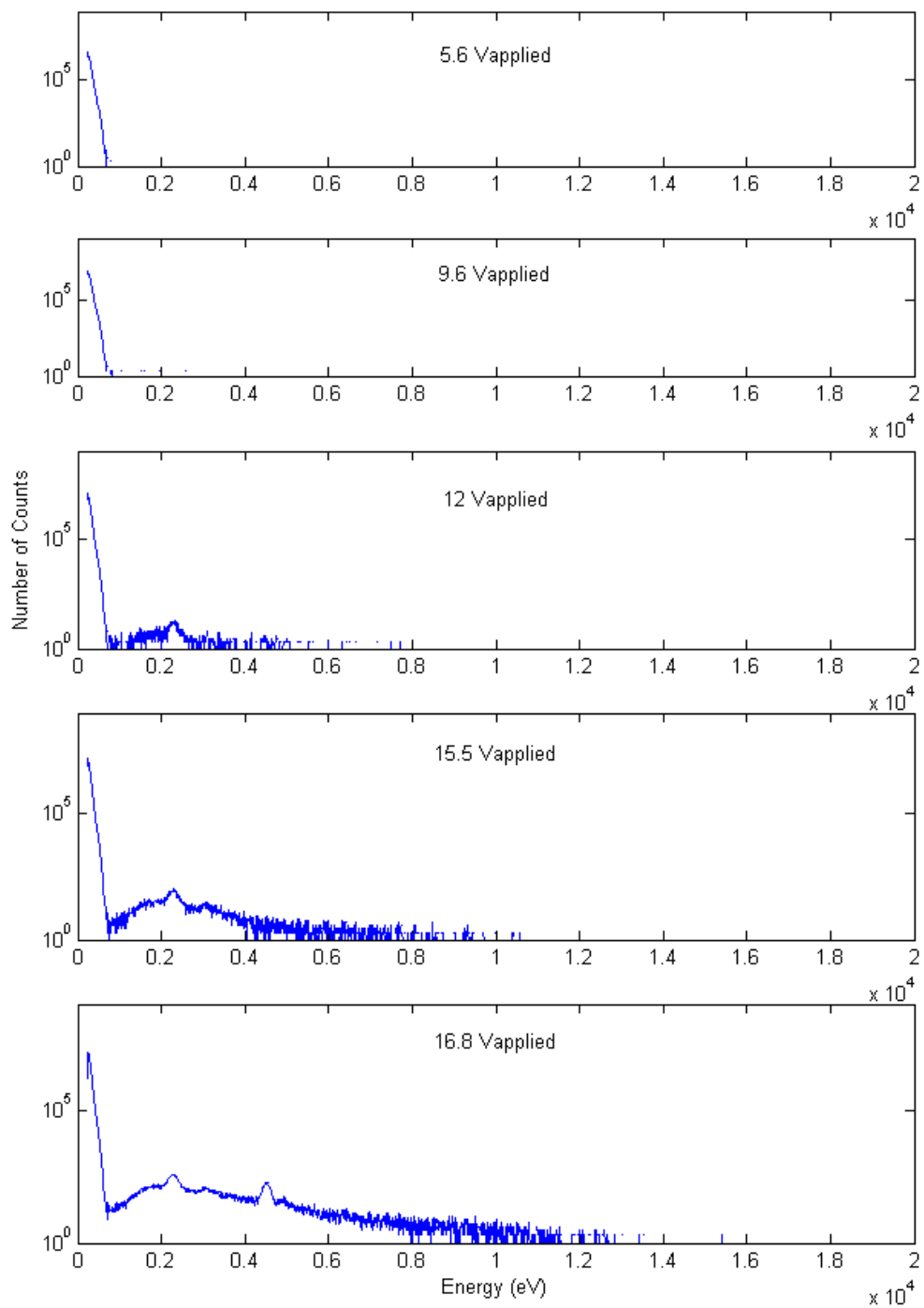


Figure 64: Bremsstrahlung and Fluorescence under increased input voltages

A summary of the input voltage compared to peak measured energy is provided in Table 6. As the applied PT voltage was increased, the output voltage was increased and electrons were accelerated to higher energies. The voltage gain of the PT is also shown. For this particular experiment, the PT was driven very close to resonance (10 Hz) to achieve very high voltage gain. Eventually the input voltage was increased to the point that the applied stress exceeded the yield stress of the transformer and the PT broke in half. This was the first PT to break after slowly exceeding the yield stress. For this PT, the highest measured x-ray energy after the detector had been calibrated for a higher energy range was 13.5 keV.

Table 6: Peak measured x-ray energy at several applied input voltages

Saturated Applied Voltage (V)	Peak Measured Xray Energy (keV)	Voltage Gain
5.6	.694	NA
9.6	.694	NA
12	5	416.7
15.5	9.31	600.7
16.8	12.6	750
19.6	Broken Crystal	NA

The PT was further examined in a similar fashion. During the test, the driving frequency was slowly increased so that it approached resonance. The supply voltage setting was maintained. However because the input impedance of the PT decreased as the frequency moves toward resonance, the actual input voltage dropped. While this input voltage drop was not accounted for in the output voltage measurement comparison, it was

accounted for in the gain comparison. The resulting x-ray spectrum at 44.52 kHz is shown in Figure 65. The peak electron energy and thus PT output voltage was 14.6 kV. Figure 66 and Figure 67 show the output voltage and gain resulting from the change in frequency for this test.

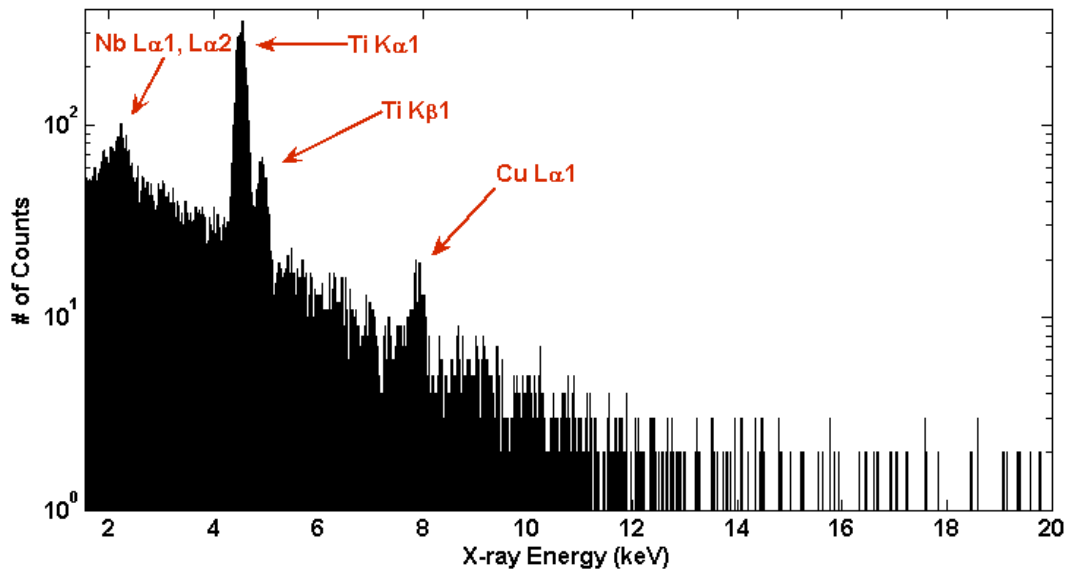


Figure 65: Measured x-ray spectrum from highest frequency of experiment.

Because there is little information on the point at which the PT will break due to exceeding its peak stress threshold, it is hard to predict what conditions lead to PT fracture. During this experiment the PT broke at 44.52 kHz frequency which was 10 Hz from true resonance. The applied voltage was 50 V_{pp} .

Finite element simulations were performed to compare the newly acquired experimental information with theoretical values. The simulated output voltage with a 25 $V_{applied}$ (50 V_{pp}) signal was compared to the

experimental output voltage provided by x-ray detection. The frequency was swept over a range that included the resonant and experimental frequencies. This comparison is shown in Figure 66. Because the experimental input voltage changed due to the change of the input impedance, a comparison was also made of the gain of the PT. This comparison is shown in Figure 67.

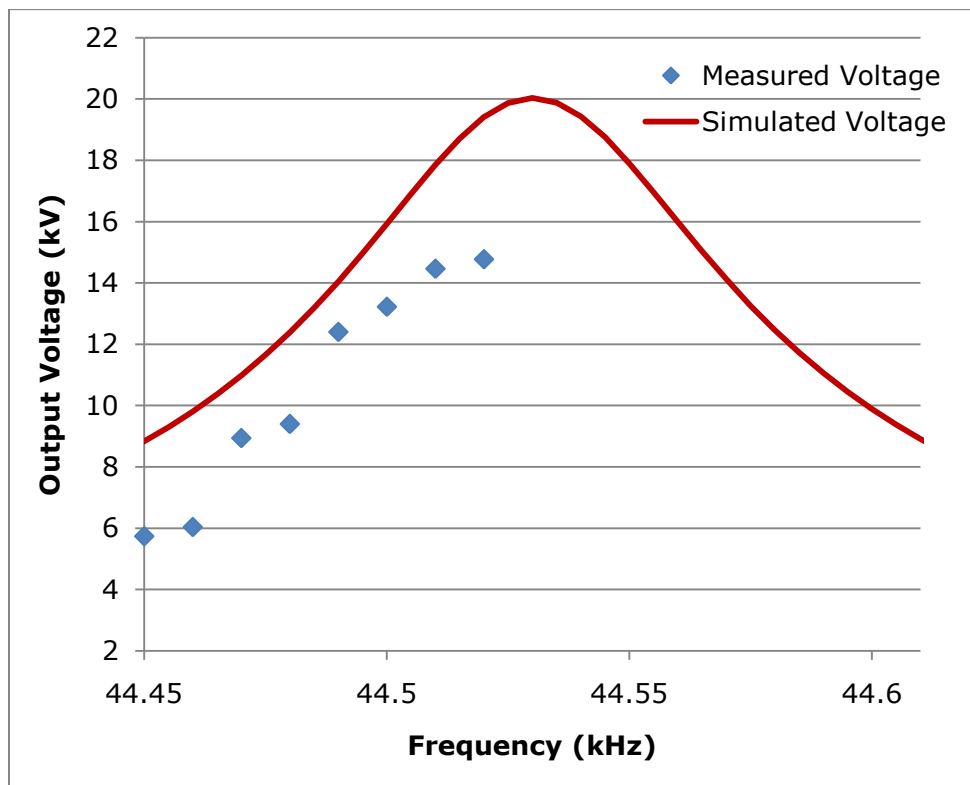


Figure 66: Measured output voltage with x-ray diagnostic compared to Simulated PT with 25 V_{applied} (50 V_{pp}). The PT providing the measured output voltage had a thin film of parylene which can contribute to loss.

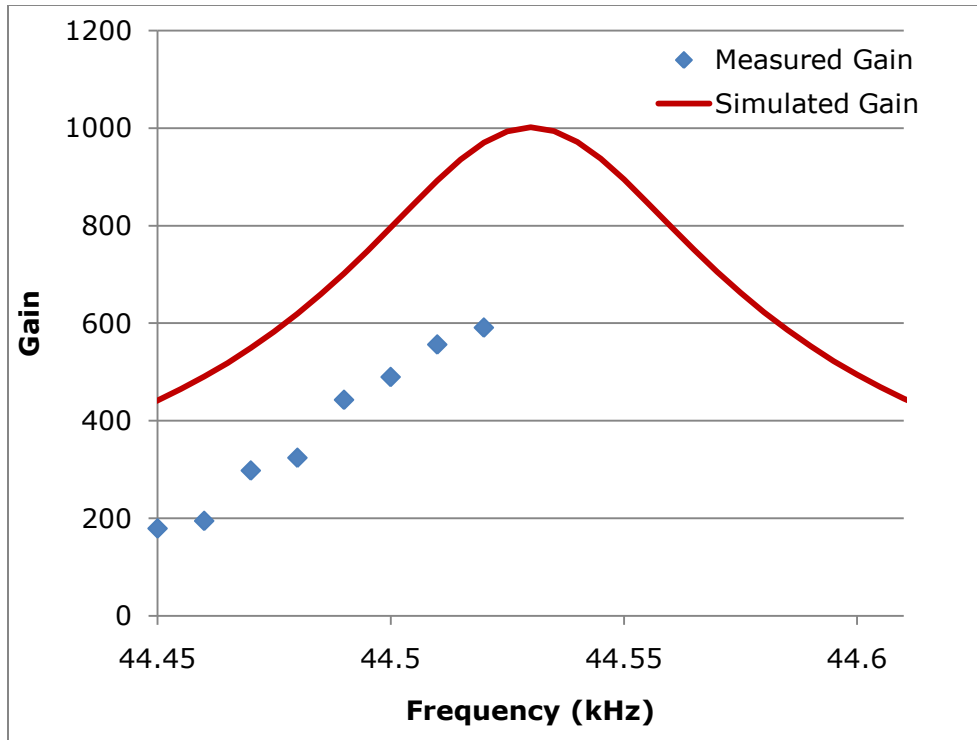


Figure 67: Measured Gain from x-ray diagnostic compared to simulated gain with experimentally determined loss. The measured PT had a thin film of parylene which can contribute to loss.

The voltage and gain measured from the PT were close to the predicted value from the simulations. Despite the fairly close fit, there is a difference between experimental and simulated data. This difference can be explained by the fact that the measured data presented were made with a PT with a thin film of parylene. The high resolution input impedance measurement was made with a PT without parylene, so the loss from the parylene was not present in the simulation.

During a separate experiment, the ability of parylene to prevent flashover was tested. The parylene was found to completely eliminate the

flashover by preventing the large electric field present on the PT surface from forming small discharges. Because the parylene was predicted to add loss to the vibration of the PT, its affect on gain was measured. The addition of parylene is described in detail later in this paper. The parylene was found to reduce gain by 20 to 50 percent depending on the length of the parylene deposition. The reduction of gain is consistent with the data in Figure 67.

Accuracy of the Bremsstrahlung measurement is another explanation for the discrepancy in measured voltage. The measurement accuracy is affected by integration time and the detector gain. Due to the nature of Bremsstrahlung emission, the fewest counts occur at the peak x-ray energy. Since x-ray generation is stochastic in nature, the accuracy of the measurement is proportional to the square root of the number of counts.

Overstressed Piezoelectric Transformers

During experimentation, a very high voltage gain was demonstrated by the PT. The PT also had the ability to accelerate particles into targets producing measureable x-rays. However, 100 kV was not produced in the laboratory. Logically, by increasing the input voltage, 100 kV would be attainable according to the gain curve. However, by increasing the applied voltage, a maximum stress limit was reached for LiNbO_3 . This threshold was reached several times resulting in broken PTs.

The threshold at which the PT will fracture due to an applied stress was examined in detail in Chapter 2. Several PTs were broken during experimentation and the conditions under which the stress led to fracture

were recorded. In one case, an applied voltage of 25 V (50 V_{pp}) at a frequency of 10 Hz from resonance resulted in a slow PT fracture. In another experiment the driving frequency was 5 Hz from true resonance and the applied voltage was 20 V and the PT broke immediately.

Simulations confirmed that the conditions under which the PT broke corresponded to conditions that led to exceeding the von Mises stress criterion for LiNbO₃. Figure 20 demonstrates the stress that occurs in the PT when it is driven at 10 Hz from resonance with 25 V applied. The peak stress was 34 MPa. 34 MPa is toward the low end of the expected yield stress for LiNbO₃, which is 30 – 120 MPa. The PT may be fracturing at this level because little effort had been made to reduce rough edges which could lead to fracture initiation point.

In order to increase the measured output voltage provided by the PT at a given stress, the bipolar output method introduced on page 44 was implemented. The input voltage was applied to the center region of the PT, and the output voltage was measured from end to end. Experiments were performed to confirm that this method could increase the output voltage of the PT.

Bipolar Output Verification

A low voltage experiment was performed in order to verify the bipolar output voltage scheme. For the setup which is shown in Figure 68, two driving electrodes were deposited in the center of the PT, and a RF signal was applied at the resonant frequency. The length extension vibration resonant

frequency still depended on the length of the PT, so the frequency remained near 45 kHz. Output voltage signals were taken with respect to ground from each end of the PT. The output signals were found to be similar in magnitude and 180° out of phase as shown in Figure 69.

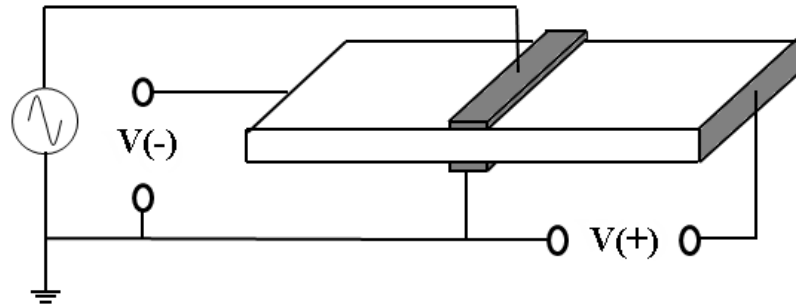


Figure 68: Experimental setup to verify a bipolar output signal. The output signals were observed to be 180° out of phase.

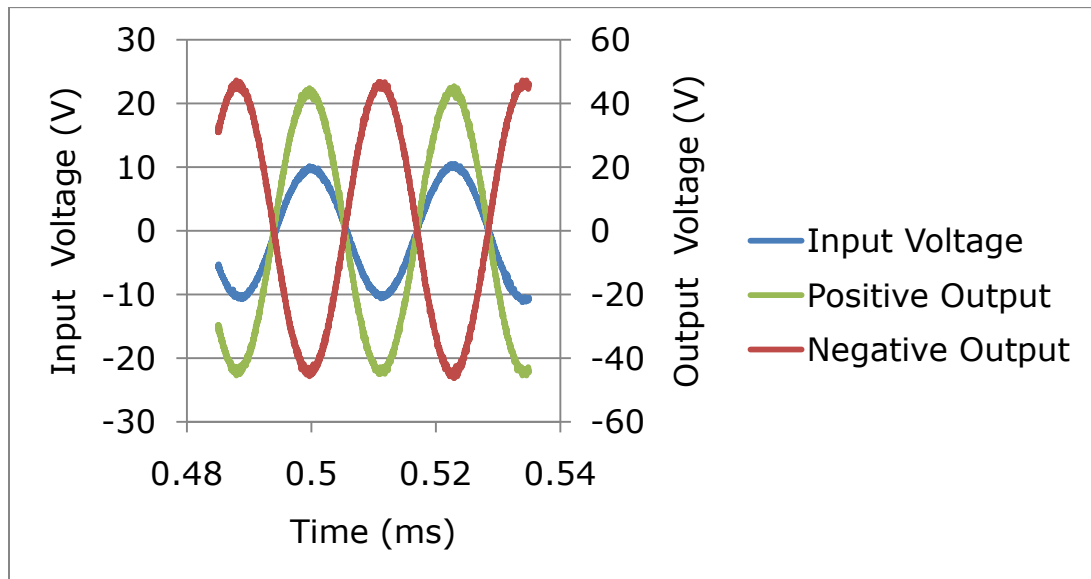


Figure 69: The output voltage from the bipolar configured PT.

A high voltage test was performed to confirm that the bipolar driven PT would produce higher voltages which could be harvested from both the plus and minus end of the PT. The PT was placed in a vacuum and one end of was attached to a titanium target with a wire as shown in Figure 70. Field emitting structures were attached to the other end. The electrons were again accelerated into the titanium target. The resulting spectrum is shown in Figure 71. The peak x-ray energy was 25 keV, which was an improvement over the non-bipolar configuration.

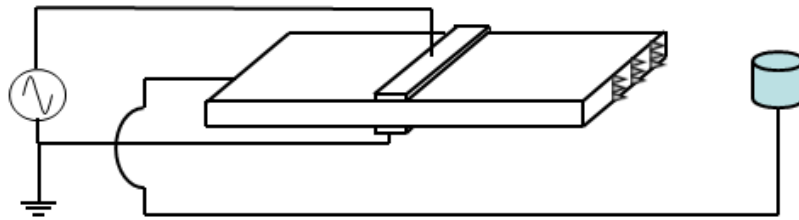


Figure 70: Bipolar high voltage test circuit

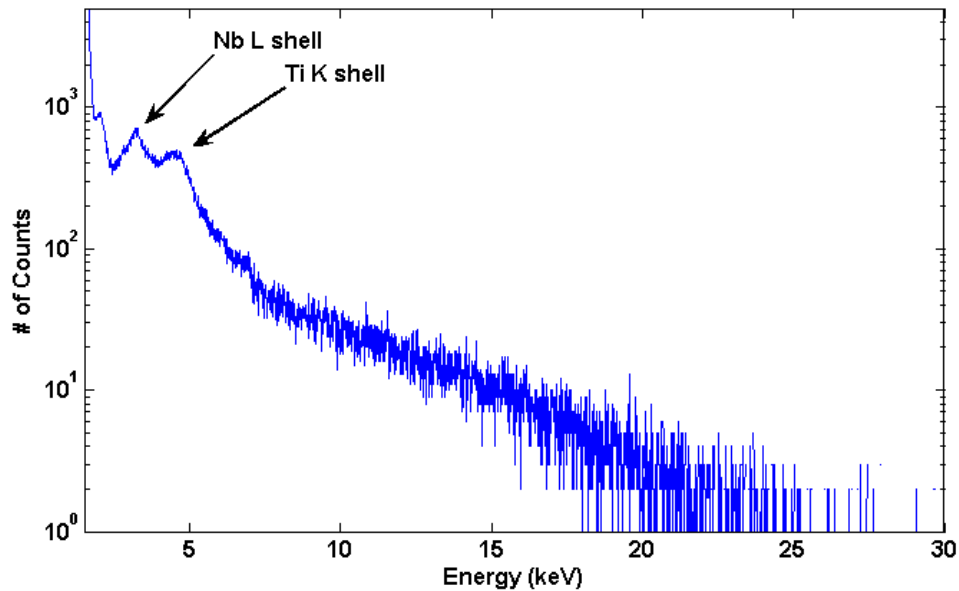


Figure 71: Spectrum from the bipolar arranged PT

5. Conclusions

Summary

This project has successfully demonstrated the use of a piezoelectric transformer to generate and accelerate particles. Many interesting topics were encountered and explored while striving toward high voltage. This document has explained many of the solutions that were developed to increase the output voltage of the PT. Beginning from its initial design, many improvements were made in response to problems that occurred and discoveries that were made.

An understanding of the operation of the transformer was developed through simulation and experimentation. This understanding that was developed was critical in the development of solutions to specific problems

that were encountered. Important models were also developed from this understanding and were used to more accurately predict the performance of the PT.

In order to optimize the PT's performance, the mechanisms which led to high voltage were investigated in detail. An iterative process of improvement by direct observation and simulation was used. As an understanding of the measured data became clearer through experimentation, the measured voltage and peak available voltage was increased. Other issues such as flashover, mechanical loss, and stress were also addressed. A summary of the important discoveries and results is presented below.

- High voltage gain was confirmed.

When the fully developed PT model was simulated, gain on the order of 800 was predicted. Once the high impedance diagnostic was developed, high voltage gain was observed from the PT. The peak measured gain was around 750 as shown in Table 6.

- Flashover was prevented by thin film encapsulation.

During this experiment, flashover was successfully prevented by thin film encapsulation. An added mechanical loss from the parylene was confirmed and is shown in Figure 57. This loss is minimized by placing the

parylene at the mechanical displacement null point and by minimizing its length. To reduce the loss, it would be best to minimize the amount of parylene needed to prevent flashover. This would allow the gain to approach its highest value.

- The peak output voltage for a given geometry was found.

By accelerating electrons into a target with the PT, a very high impedance diagnostic was developed. This allowed for a measurement of the peak voltage able to be produced by the PT. While 100 kV was not fully achieved, an explanation for the difficulties in attaining 100 kV was been developed.

Because the peak von Mises stress that the LiNbO_3 can withstand was exceeded with the initial design as shown in Figure 20, a redesign was made to more evenly distribute the peak stress. The evenly distributed stress is shown in Figure 35.

While the peak voltage was initially predicted to be 20 kV and measured at 14.6 kV, the first PT redesign experiment demonstrated 25 kV in the laboratory. Several proposed solutions will help in the future attainment of that 100 kV.

Future Work

The first of a group of redesigns, specifically the bipolar output PT, was found to successfully increase the available voltage from the PT. While its success was encouraging, many experiments remain to fully develop the details of the design. For example, the input impedance of the PT was not measured in detail, but there was indication that it had increased over the non-bipolar design. This was because the surface area over which the driving electric field was applied was reduced.

In addition, several of the other redesigns that were presented in order to more evenly spread the PT stress have not been confirmed by experimentation.

Finally, several interesting circuit designs to increase the output voltage were considered throughout this project. It may be possible to use elements such as small capacitance and diodes to create a voltage doubling circuit very similar to a Cockroft-Walton generator. It may also be possible to arrange several PTs in a fashion so that the output voltage could be added similar to a Marx bank architecture. These ideas could be expanded and tested.

APPENDIX

Comsol Simulation Guideline

The module that was used was the MEMS -> Structural Mechanics -> Piezo Solid module. Two useful simulation types were performed: Eigenfrequency analysis and frequency response analysis. The Eigenfrequency was used to determine resonant frequency modes quickly and the frequency response was used to determine actual responses such as electric potential and material displacement.

For all simulations, a three dimensional object was inserted into the work space. This object was composed of three connected regions: input, output development, and output voltage. These three regions composed the vibrating LiNbO₃ material and are demonstrated in Figure 10.

The drawn material was oriented according to the un-rotated piezoelectric standard described in [24]. Once the PT geometry was entered into the work space, a new coordinate system was created according to the desired polarization rotation angle. For most of this project, that angle was -135°. The sub-domain settings were then entered for the PT geometry. LiNbO₃ was applied at the new coordinate system with the appropriate dielectric and mechanical loss factors.

In some simulations additional solids were entered into the simulation that represented electrodes. The material properties of aluminum were applied to the electrodes in the global (un-rotated) coordinate system.

Boundary conditions were then applied to the LiNbO₃ material. All surfaces were allowed to freely vibrate unless a particular restrictive boundary condition was desired. The driving signal was applied to the top of the input side of the PT. The bottom of the input side was set as ground. The top output surface of the of output voltage section was set to floating potential. On all other surfaces, a zero charge boundary condition was set.

The Eigenfrequency simulation was then performed to determine the length extensional frequency, and the appropriate frequency was noted. Then the simulation type was changed to frequency response over a range of frequencies that included the length extensional frequency. Often an array was entered as: $(f_0-250):10:(f_0+250)$. This would simulate the response over 500 Hz at a 10 Hz interval.

Matlab Data Calculations

```
clear;
computer_name='andy';
probe_multiplier=369.7 %from calibration curves
%taken from experiment
frequencies=[43.025 43.225 43.425 43.625 43.825 43.905 43.985 44.065 44.145
44.225 44.305 44.345 44.385 44.425 44.445 44.465 44.485 44.505 44.525 44.545
44.565 44.585 44.605 44.625 44.645 44.665 44.685 44.705 44.745 44.785 44.825
44.905 44.985 45.065 45.145 45.225 45.425 45.625 45.825 46.025 46.225 46.425
46.625 46.825 47.025];
frequencies=frequencies*1000;
w=2.*pi.*frequencies;

test='2009-01-23 test 1';
parameter='29.5:5 mm';
startshotnumber=0;
index=1;
for I=1:45
    shotnumber=startshotnumber+index-1;
    clear time_period input_voltage_filtered_offset_period
output_voltage_filtered_offset_period
    clear input_current_filtered_offset_period output_current_filtered_offset_period
    clear power integral
    %shotnumber=69
    %I=70

    if shotnumber<1000;
    pre_shotnumber='0';
    end
    if shotnumber<100;
    pre_shotnumber='00';
    end
    if shotnumber<10;
    pre_shotnumber='000';
    end

    sn=num2str(shotnumber);
    shot=strcat(pre_shotnumber,sn);
    directory_to_change_to=strcat('C:\Documents and
Settings\',computer_name,'\Desktop\benwell\data\',test,'\');
    current_dir=cd(directory_to_change_to); %set the current directory to the media
directory
    addpath(genpath(strcat(current_dir,'\ALL',shot,'\'))); %the the directory with the
shot of interest as the first directory searched for the path
    %load channel 1
%    data1=tekload(strcat('F',shot,'CH1','.CSV'),'CSV');
%    time_data1=data1.Time; %separate the structure into two different arrays
%    channel1=data1.Waveform;
    %load channel 2
```

```

data2=tekload(strcat('F',shot,'CH2','.CSV'),'CSV');
time_data2=data2.Time; %separate the structure into two different arrays
channel2=data2.Waveform;
%load channel 3
data3=tekload(strcat('F',shot,'CH3','.CSV'),'CSV');
time_data3=data3.Time; %separate the structure into two different arrays
channel3=data3.Waveform;
%load channel 4
data4=tekload(strcat('F',shot,'CH4','.CSV'),'CSV');
time_data4=data4.Time; %separate the structure into two different arrays
channel4=data4.Waveform;

%change data structure names if necessary
time=time_data2;
% signal_generator=channel1;
%get rid of dc offset
input_voltage=channel2;

[input_voltage_filtered,dt]=butterfilterupdated2(time,input_voltage,200E3,20,800,7
99);

input_voltage_offset=((max(input_voltage_filtered)+min(input_voltage_filtered))/2)
;
input_voltage_filtered_offset=input_voltage_filtered-input_voltage_offset;
%get rid of dc offset
output_voltage=channel3*probe_multiplier;

[output_voltage_filtered,dt]=butterfilterupdated2(time,output_voltage,200E3,20,800
,799);

output_voltage_offset=((max(output_voltage_filtered)+min(output_voltage_filtered)
)/2);
output_voltage_filtered_offset=output_voltage_filtered-output_voltage_offset;
%get rid of dc offset
input_current=channel4;

[input_current_filtered,dt]=butterfilterupdated2(time,input_current,200E3,20,800,79
9);

input_current_offset=((max(input_current_filtered)+min(input_current_filtered))/2);
input_current_filtered_offset=input_current_filtered-input_current_offset;

%calculate transformer ratio
input_voltage_filtered_offset_pk_pk(index)=max(input_voltage_filtered_offset)-
min(input_voltage_filtered_offset);

output_voltage_filtered_offset_pk_pk(index)=max(output_voltage_filtered_offset)-
min(output_voltage_filtered_offset);

%transformer_ratio(index)=output_voltage_filtered_offset_pk_pk(index)./input_volt
age_filtered_offset_pk_pk(index);

```

```

transformer_ratio(index)=output_voltage_filtered_offset_pk_pk(index)/input_voltag
e_filtered_offset_pk_pk(index);
%Calculate Power
% time=time*1e9;      %convert time to nanoseconds
time_step=time(2)-time(1);  %time_step in nanoseconds

%find index of first negative going input_voltage zero crossing

n=1;
if input_voltage_filtered_offset(n)<0
    while input_voltage_filtered_offset(n)<0
        n=n+1;
    end
    n=n+10;
end

while input_voltage_filtered_offset(n)>0
    n=n+1;
end
start_index=n;

n=n+15;
while input_voltage_filtered_offset(n)<0
    n=n+1;
end
n=n+15;
while input_voltage_filtered_offset(n)>0
    n=n+1;
end
end_index=n;

% frequency=1/((end_index-start_index)*time_step);
% measured_frequency(index)=frequency;

%find theta by first finding current zero crossings

n=end_index;
if input_current_filtered_offset(n)<0 %current leads, theta is positive
    while input_current_filtered_offset(n)<0
        n=n-1;
    end
    current_lead_index=n;
    time_difference=(end_index-current_lead_index)*time_step;
    theta(index)=2*pi*time_difference*frequencies(index);
end

n=end_index;
if input_current_filtered_offset(n)>0 %current lags, theta is negative
    while input_current_filtered_offset(n)>0
        n=n-1;
    end
    current_lag_index=n;

```

```

        time_difference=(end_index-current_lag_index)*time_step;
        theta(index)=2*pi*time_difference*frequencies(index);
    end

    %redefine voltages and current to only include one period
    for P=1:(end_index-start_index)
        time_period(P)=time(start_index+P-1);

input_voltage_filtered_offset_period(P)=input_voltage_filtered_offset(start_index+P-1);

output_voltage_filtered_offset_period(P)=output_voltage_filtered_offset(start_index+P-1);

input_current_filtered_offset_period(P)=input_current_filtered_offset(start_index+P-1);

        %output current I=c(dv/dt)
        %for derivative=1:length(output_voltage_filtered_offset_period)-1
        if P>1
            output_current_filtered_offset_period(P)=93E-
12*(output_voltage_filtered_offset_period(P)/probe_multiplier-
output_voltage_filtered_offset_period(P-1)/probe_multiplier)/(time_step);
        end
    end

output_current_filtered_offset_period(1)=output_current_filtered_offset_period(2);

    %calculate average input power
    n=start_index;
    m=1;
    power(end_index-start_index+2)=0;
    while m<(length(time_period)-1)
        % while n<end_index/2+1
        %integrate instant power
        % power(m)=power(m-1)+time_step/3*1e-9*(input_voltage(2*n-
2)*input_current_filtered(2*n-2)+4*input_voltage(2*n-
1)*input_current_filtered(2*n-
1)+input_voltage(2*n)*input_current_filtered_offset(2*n));

power(m)=time_step/3*(input_voltage_filtered_offset_period(m)*input_current_filtered_offset_period(m)+4*input_voltage_filtered_offset_period(m+1)*input_current_filtered_offset_period(m+1)+input_voltage_filtered_offset_period(m+2)*input_current_filtered_offset_period(m+2));
        m=m+1;
        n=n+1;
    end
    integral=sum(power);
    %divide by one period
    simpson_input_power(index)=abs(integral*frequencies(index));

    %calculate average output power
    n=start_index;

```

```

m=1;
power(end_index-start_index+2)=0;
while m<length(time_period)-1

power(m)=time_step/3*(output_voltage_filtered_offset_period(m)*output_current_f
iltered_offset_period(m)+4*output_voltage_filtered_offset_period(m+1)*output_cur
rent_filtered_offset_period(m+1)+output_voltage_filtered_offset_period(m+2)*outp
ut_current_filtered_offset_period(m+2));
    m=m+1;
    n=n+1;
end
integral=sum(power);
%divide by one period
simpson_output_power(index)=abs(integral*frequencies(index));

%put time back into regular seconds
% time=time./1e9;

input_current_filtered_offset_pk_pk(index)=max(input_current_filtered_offset_perio
d)-min(input_current_filtered_offset_period);

output_current_filtered_offset_pk_pk(index)=max(output_current_filtered_offset_pe
riod)-min(output_current_filtered_offset_period);
    input_vrms=sqrt(mean(input_voltage_filtered_offset_period.^2));
    irms=sqrt(mean(input_current_filtered_offset_period.^2));
    output_vrms=sqrt(mean(output_voltage_filtered_offset_period.^2));
    average_input_power(index)=cos(theta(index)).*input_vrms.*irms;
    Real(index)=input_vrms.*cos(theta(index))./irms;
    Imaginary(index)=input_vrms.*sin(theta(index))./irms;
    Zmag(index)=input_vrms/irms;
    absorbed_power(index)=simpson_input_power(index)-
simpson_output_power(index);
    efficiency(index)=simpson_output_power(index)./simpson_input_power(index);
    index=index+1
end
fclose('all')
%END OF ACQUISITION

%answers= [frequencies; transformer_ratio; output_voltage_filtered_offset_pk_pk;
Zmag; simpson_input_power; input_voltage_filtered_offset_pk_pk;
input_current_filtered_offset_pk_pk; output_current_filtered_offset_pk_pk]

%plots
plot(frequencies./1000,transformer_ratio,'.')
xlabel('Frequency (kHz)')
ylabel('Transformer Gain (Vout / Vin)')
title(parameter)
plot(frequencies./1000,output_voltage_filtered_offset_pk_pk,'.')
xlabel('Frequency (kHz)')
ylabel('Output Voltage (V)')
title(parameter)
semilogy(frequencies./1000,Zmag/1000,'.')
xlabel('Frequency (kHz)')

```

```

ylabel('Input Impedance (k \Omega)')
title(parameter)
plot(frequencies./1000,theta,'.')
xlabel('Frequency (kHz)')
ylabel('Current - Voltage Phase Difference (Rad.)')
title(parameter)
plot(frequencies./1000,(Real),'.')
xlabel('Frequency (kHz)')
ylabel('Input Resistance (\Omega)')
title(parameter)
plot(frequencies./1000,Imaginary,'.')
xlabel('Frequency (kHz)')
ylabel('Input Reactance ')
title(parameter)
plot(frequencies./1000,simpson_input_power)
xlabel('Frequency (kHz)')
ylabel('Average Input Power (W)')
title(parameter)
% plot(frequencies(index)./1000,(average_input_power))
% xlabel('Frequency (kHz)')
% ylabel('Average Input Power (W)')
%title(parameter)
plot(frequencies./1000,(simpson_output_power))
xlabel('Frequency (kHz)')
ylabel('Average Output Power (W)')
title(parameter)
plot(frequencies./1000,(efficiency))
xlabel('Frequency (kHz)')
ylabel('Efficiency')
title(parameter)

%Combined Plots
plot(frequencies(index)./1000,Zmag,.',frequencies(index)./1000,(Real),'o')
plotyy(frequencies(index)./1000,(simpson_input_power),frequencies(index)./1000,(a
verage_output_power))
plot(frequencies(index)./1000,simpson_input_power,frequencies(index)./1000,(aver
age_input_power))

plot(time, output_voltage)

```

Impedance Calculating Script

```
subplot(4,1,1), plot(time_period,input_voltage_filtered_offset_period)
subplot(4,1,2), plot(time_period,output_voltage_filtered_offset_period)
subplot(4,1,3), plot(time_period,input_current_filtered_offset_period)
subplot(4,1,4), plot(time_period,output_current_filtered_offset_period)

[Zmin,min_location]=min(Zmag);
[Zmax,max_location]=max(Zmag);
fR1=frequencies(min_location);
fA1=frequencies(max_location);
wR1=2*pi*fR1;
wA1=2*pi*fA1;

%Circuit Parameters
C0=102.8E-12
R0=.1
C1=((wA1^2)/(wR1^2)-1)*C0
L1=1/((wR1^2)*C1)
R1=Zmin
Cc=95E-12

ZR0=R0;
ZC0=1./(i.*w*C0);
ZC1=1./(i.*w*C1);
ZL1=i.*w*L1;
ZR1=R1;
ZCc=1./(i.*w*Cc);

Zcrystal=abs(((1./(ZC0+ZR0)+1./(ZC1+ZL1+ZR1))).^-1);
%Zcrystal=abs(((1./ZC1+1./(ZC0+ZR0)+1./(ZC1+ZL1+ZR1))+1./ZCc).^-1);
Zexperimental=Zmag;
rsquared=(Zcrystal-Zexperimental).^2;
rsquared_sum=sum(rsquared)

semilogy(frequencies, Zexperimental, '.', frequencies, Zcrystal);

R0=LOGSPACE(-3, 5, 100);
R1=LOGSPACE(-2, 5, 100);
C0=LOGSPACE(-11, -9, 100);
C1=((wA1^2)/(wR1^2)-1).*C0;
L1=1/((wR1^2).*C1);
Cc=95E-12;
rsquared_sum_best=1E20

for K=1:100
    ZC0=1./(i.*w*C0(K));
    ZC1=1./(i.*w*C1(K));
    ZL1=i.*w*L1(K);
    %    ZCc=1./(i.*w*Cc);

for I=1:100
```

```

ZR0=R0(I);
for J=1:100
    ZR1=R1(J);

%    Zcrystal=abs(((1./ZC1+1./(ZC0+ZR0)+1./(ZC1+ZL1+ZR1))+1./ZCc).^-1);
%Zcrystal=abs((1./ZC1+1./(ZC0+ZR0)+1./(ZC1+ZL1+ZR1)).^-1);
Zcrystal=abs((1./(ZC0+ZR0)+1./(ZC1+ZL1+ZR1)).^-1);
Zexperimental=Zmag;

rsquared=(Zcrystal-Zexperimental).^2;
rsquared_sum=sum(rsquared);

if rsquared_sum < rsquared_sum_best
    R0_best=ZR0;
    R1_best=ZR1;
    C0_best=C0(K);
    C1_best=C1(K);
    L1_best=L1(K);
    rsquared_sum_best=rsquared_sum;
end %end if rsquared

end %end for R1

end %end for R0
end %end for C0
ZR0=R0_best
ZR1=R1_best
C0_best
C1_best
L1_best
rsquared_sum_best
ZC0=1./(i.*w*C0_best);
ZC1=1./(i.*w*C1_best);
ZL1=i.*w*L1_best;

%Zcrystal_best=abs((1./ZC1+1./(ZC0+ZR0)+1./(ZC1+ZL1+ZR1)).^-1);
Zcrystal_best=abs((1./(ZC0+ZR0)+1./(ZC1+ZL1+ZR1)).^-1);
% Zcrystal_best=abs(((1./ZC1+1./(ZC0+ZR0)+1./(ZC1+ZL1+ZR1))+1./ZCc).^-1);

semilogy(frequencies, Zexperimental, '.', frequencies, Zcrystal_best);

```

Impedance Matching Network Design Matlab Script

```
clear;
f=42E3:1:46E3;
w=2.*pi.*f;
%crystal impedances
ZR0=.1;
C0=400E-12;
ZC0=1./(i.*w*C0);

%LL matching network impedances

C1=6.36E-12;
ZC1=1./(i.*w*C1);
L1=2.04;
ZL1=i.*w*L1;
ZR1=100;

range=LOGSPACE(-9,-8,10);
%Cs=21.3E-9;
Cs=range.*21.3;
Ls=165E-6;
Ll=397E-6;
Cl=112.2E-9;

for n=1:10

    ZCs(n,:)=1./(i.*w.*Cs(n));
    ZLs=i.*w*Ls;
    ZLl=i.*w*Ll;
    ZCl=1./(i.*w*Cl);

    Zcrystal=(1./ZC1+1./(ZC0+ZR0)+1./(ZC1+ZL1+ZR1)).^-1;
    ZLL(n,:)=ZCs(n,)+(1./ZLs+1./((1./ZCl+1./Zcrystal).^(-1)+ZLl)).^-1;

    Zload=Zcrystal;
    Zload(n,:)=ZLL(n,:);
    Zmag(n,:)=sqrt((real(Zload(n,:))).^2+(imag(Zload(n,:))).^2);

end

plot(f./1000,Zmag)
xlabel('frequency (Rad)')
ylabel('Zmag (\Omega)')
semilogy(f./1000,Zmag)

[minimum, min_index] = min(Zmag)

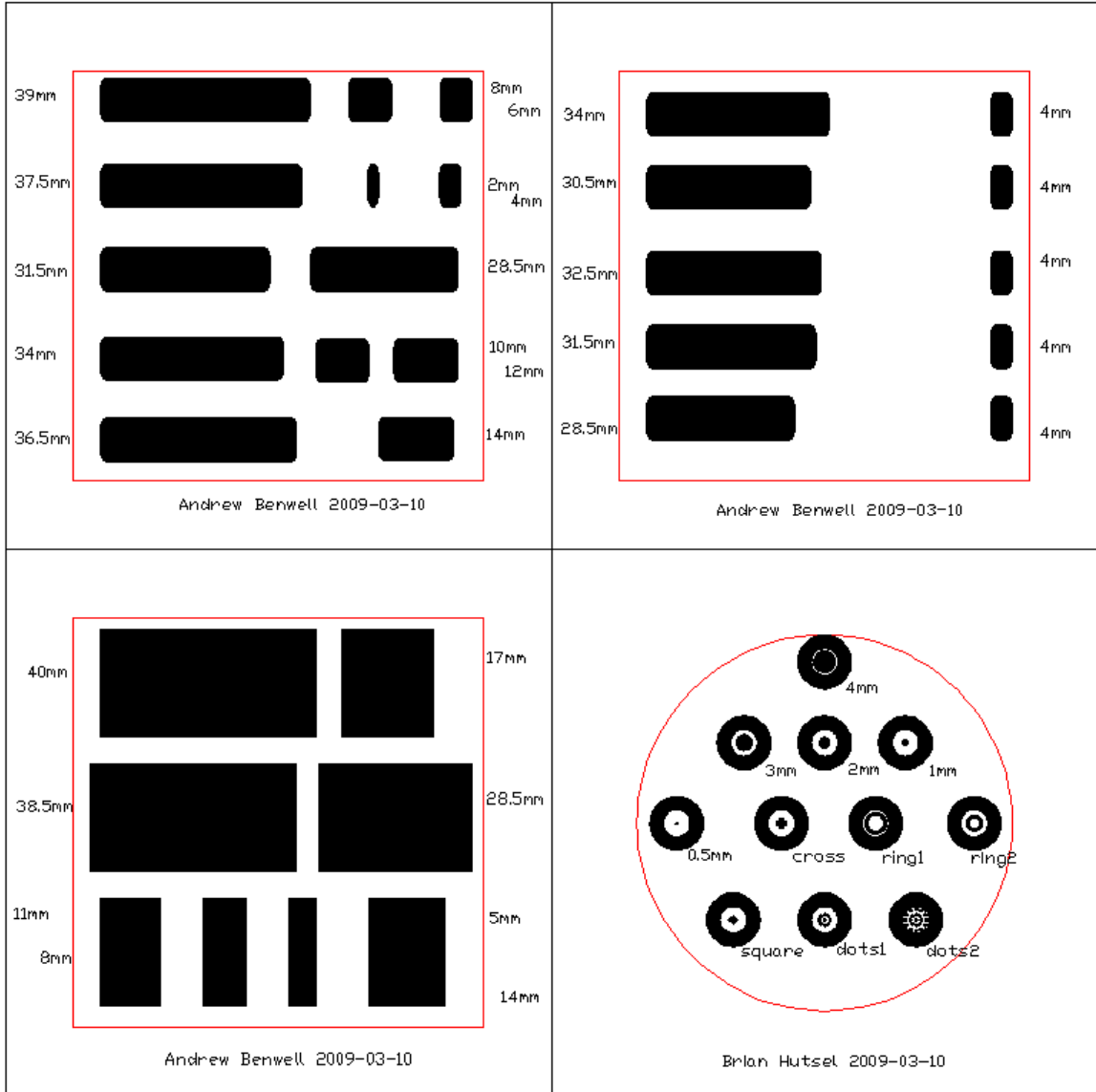
Zload(min_index)

plot(f./1000,Cs)
```

Photo Resist Patterns

These images were drawn in a cad program and sent to Finline Imaging in Denver, CO.

www.finline-imaging.net



Bibliography

- [1] C. Grassley, M. Baucus, B. Thomas, and C. Rangel, "Container security: Expansion of key customs programs will require greater attention to critical success factors," United States General Accounting Office, Tech. Rep., Jul. 2003.
- [2] D. Slaughter, M. Accatino, A. Bernstein, A. Dougan, J. Hall, A. Loshak, D. Manatt, B. Pohl, R. Walling, D. Weirup, and S. Prussin, "The "nuclear car wash": a scanner to detect illicit special nuclear material in cargo containers," *Sensors Journal, IEEE*, vol. 5, no. 4, pp. 560–564, 2005.
- [3] C. Moss, M. Brener, C. Hollas, and W. Myers, "Portable active interrogation system," *Nuclear Instruments and Methods in Physics Research Section B: Beam Interactions with Materials and Atoms*, vol. 241, no. 1-4, pp. 793–797, Dec. 2005. [Online]. Available: <http://www.sciencedirect.com/science/article/B6TJN-4GY88RY-F/1/fe2c053608c24f04d806be32fe95ed00>
- [4] C. Moss, C. Hollas, G. Mckinney, and W. Myers, "Comparison of active interrogation techniques," *Nuclear Science, IEEE Transactions on*, vol. 53, no. 4, pp. 2242–2246, 2006.
- [5] C. Moss, C. Goulding, C. Hollas, and W. Myers, "Neutron detectors for active interrogation of highly enriched uranium," *Nuclear Science, IEEE Transactions on*, vol. 51, no. 4, pp. 1677–1681, 2004.
- [6] M. Gmar, E. Berthoumieux, S. Boyer, F. Carrel, D. Dore, M. Giacri, F. Laine, B. Poumarede, D. Ridikas, and A. Lauwe, "Detection of nuclear material by photon activation inside cargo containers," in *SPIE Defense and Security Symposium*, Apr. 2006.
- [7] J. Mihalczko, "Radiation detection for active interrogation of heu," Oak Ridge National Laboratory, Tech. Rep., Dec. 2004.
- [8] T. Gozani, "The role of neutron based inspection techniques in the post 9/11/01 era," *Nuclear Instruments and Methods in Physics Research Section B: Beam Interactions with Materials and Atoms*, vol. 213, pp. 460–463, Jan. 2004. [Online]. Available: <http://www.sciencedirect.com/science/article/B6TJN-48WHJ2G-S/1/2ed747a41a8c14d425d68413e3d1e88c>
- [9] V. Tang, G. Meyer, J. Morse, G. Schmid, C. Spadaccini, P. Kerr, B. Rusnak, S. Sampayan, B. Naranjo, and S. Putterman, "Neutron production from feedback controlled thermal cycling of a pyroelectric crystal," *Review of*

Scientific Instruments, vol. 78, no. 12, pp. 123504–123504, Dec. 2007.
[Online]. Available: <http://link.aip.org/link/?RSI/78/123504/1>

[10] B. Rosenblum, P. Braunlich, and J. Carrico, "Thermally stimulated field emission from pyroelectric linbo₃," *Applied Physics Letters*, vol. 25, no. 1, pp. 17–19, Jul. 1974. [Online]. Available: <http://link.aip.org/link/?APL/25/17/1>

[11] C. Rosen, "Ceramic transformer and wave filters," in *Proc. Electron. Compon. Symp.*, 1957, pp. 205–.

[12] R. Byrd, J. Moss, W. Priedhorsky, C. Pura, G. Richter, K. Saeger, W. Scarlett, S. Scott, and J. Wagner, R.L., "Nuclear detection to prevent or defeat clandestine nuclear attack," *Sensors Journal, IEEE*, vol. 5, no. 4, pp. 593–609, 2005.

[13] J. A. Geuther and Y. Danon, "Electron and positive ion acceleration with pyroelectric crystals," *Journal of Applied Physics*, vol. 97, no. 7, pp. 074109–5, Apr. 2005. [Online]. Available: <http://link.aip.org/link/?JAP/97/074109/1>

[14] J. Geuther, Y. Danon, and F. Saglime, "Nuclear reactions induced by a pyroelectric accelerator," *Physical Review Letters*, vol. 96, no. 5, p. 054803, 2006. [Online]. Available: <http://link.aps.org/abstract/PRL/v96/e054803>

[15] J. A. Geuther and Y. Danon, "Enhanced neutron production from pyroelectric fusion," *Applied Physics Letters*, vol. 90, no. 17, p. 174103, 2007. [Online]. Available: <http://link.aip.org/link/?APL/90/174103/1>

[16] J. Yang, "Piezoelectric transformer structural modeling - a review," *Ultrasonics, Ferroelectrics and Frequency Control, IEEE Transactions on*, vol. 54, no. 6, pp. 1154–1170, 2007.

[17] K.-T. Chang, "Effects of load resistances on step-up voltage gains of rosen-type piezoelectric transformer," *Industrial Technology, 2005. ICIT 2005. IEEE International Conference on*, pp. 1080–1085, Dec. 2005.

[18] Y.-H. Hsu, C.-K. Lee, and W.-H. Hsiao, "Electrical and mechanical fully coupled theory and experimental verification of rosen-type piezoelectric transformers," *Ultrasonics, Ferroelectrics and Frequency Control, IEEE Transactions on*, vol. 52, no. 10, pp. 1829–1839, Oct. 2005.

[19] T. Tsuchiya, Y. Kagawa, N. Wakatsuki, and H. Okamura, "Finite element simulation of piezoelectric transformers," *Ultrasonics, Ferroelectrics*

- and Frequency Control, IEEE Transactions on*, vol. 48, no. 4, pp. 872–878, 2001.
- [20] H. Itoh, K. Teranishi, and S. Suzuki, "Discharge plasmas generated by piezoelectric transformers and their applications," *Plasma Sources Science and Technology*, vol. 15, no. 2, pp. S51–S61, 2006.
- [21] M. Kemp and S. Kovaleski, "Piezoelectric-resonance effect in a radio-frequency-driven ferroelectric plasma source," *Plasma Science, IEEE Transactions on*, vol. 35, no. 3, pp. 578–581, 2007.
- [22] J. Hyun-Woo, L. Chang-Hwan, R. Jong-Seok, and J. Hyun-Kyo, "Identification of material constants for piezoelectric transformers by three-dimensional, finite-element method and a design-sensitivity method," *Ultrasonics, Ferroelectrics and Frequency Control, IEEE Transactions on*, vol. 50, no. 8, pp. 965–971, 2003.
- [23] E. Syed, F. Dawson, and S. Rogers, E.S., "Analysis and modeling of a rosen type piezoelectric transformer," in *Power Electronics Specialists Conference, 2001. PESC. 2001 IEEE 32nd Annual*, F. Dawson, Ed., vol. 4, 2001, pp. 1761–1766.
- [24] F. Standards Committee of the IEEE Ultrasonics and F. C. Society, "Ieee standard on piezoelectricity," IEEE, Tech. Rep., Sep. 1987.
- [25] "Comsol multiphysics," pp. –, 2008.
- [26] V. da Silva, *Mechanics and Strength of Materials*. Springer, 2006.
- [27] K. Wong, *Properties of Lithium Niobate*. INSPEC, 2002.
- [28] R. Holland, *Design of Resonant Piezoelectric Devices*. Masseurchuset Institute of Technology, 1969.
- [29] K. Nakamura and Y. Adachi, "Piezoelectric transformers using linbo3 single crystals," *Electronics and Communications in Japan*, vol. 81, no. 7, pp. 1–6, 1998.
- [30] M. Kemp, "The ferroelectric plasma thruster," Ph.D. dissertation, University of Missouri, 2008.
- [31] Y. Ohmachi, K. Sawamoto, and H. Toyoda, "Dielectric properties of linbo3 single crystal up to 9 gc," *Japanese Journal of Applied Physics*, vol. 6, no. 12, pp. 1467–1468, 1967. [Online]. Available: <http://jjap.ipap.jp/-link?JJAP/6/1467/>

- [32] B. Gall, "The automated etching of atomically sharp tungsten structures for field emission," University of Missouri Department of Electrical and Computer Engineering, Tech. Rep., 2009.
- [33] R. Cline, "Scanning tunneling electron microscope," <http://webphysics.davidson.edu/Alumni/DoNeumann/lab.htm/STM/contents.htm>.
- [34] K. Wolff, "10 kv pulser calibration instrument," University of Missouri, Tech. Rep., 2008.
- [35] G. Ivensky, I. Zafrany, and S. Ben-Yaakov, "Generic operational characteristics of piezoelectric transformers," *Power Electronics, IEEE Transactions on*, vol. 17, no. 6, pp. 1049–1057, Nov 2002.
- [36] "Matlab student version," pp. –, 2008.
- [37] G. Tripoli, D. Conte, S. Seiler, P. Turchi, and C. Boyer, "Flashover inhibition by encapsulation," in *7th IEEE Int'l Pulsed Power Conference*, 1989.
- [38] L. Jedynak, "Vacuum insulation of high voltages utilizing dielectric coated electrodes," *Journal of Applied Physics*, vol. 35, no. 6, pp. 1727–1733, 1964. [Online]. Available: <http://link.aip.org/link/?JAP/35/1727/1>
- [39] P. C. Services, "Parylene c datasheet."
- [40] *Operating Manual XR-100CR X-ray Detector, Revision 15, January, 2007.*

VITA

Andrew Benwell was born on July 5th, 1980 in Wentzville, Missouri. He earned his B.S., M.S., and Ph.D. in Electrical Engineering in 2003, 2007, and 2009 respectively. In July of 2006, Andrew married Risa Kitawaki of Kyoto, Japan. Andrew now works for SLAC National Accelerator Laboratory in Menlo Park, California.